Self-focusing of a Pulsed Electron Beam in Gases and Their Ionization

—A novel approach to discharge chemistry—

June 1982

日 本 原 子 力 研 究 所

Japan Atomic Energy Research Institute

Self-focusing of a Pulsed Electron Beam in Gases and Their Ionization

—A novel approach to discharge chemistry —

Hiroshi Hotta*, Hidehiko Arai, Ryuichi Tanaka+ and Hiromi Sunaga+

Division of Research
Takasaki Radiation Chemistry Research Establishment
Japan Atomic Energy Research Institute
Watanuki-cho, Takasaki-shi, Gunma-ken

Abstract

A relativistic high-intensity pulsed electron beam generated from a Febetron 706 was strongly self-focused in two pressure regions, i.e., below and above 5 Torr. The dependence of the electron energy spectrum on pressure and path length in He was at first studied by measuring depth-dose distributions in an aluminum-blue cellophane stack. Then, maximum doses of the depth-dose curves in the dosimeter placed on the beam axis at 10.4 cm from the cell window were measured as functions of pressure in He, Ne, Ar, Kr, Xe, H_2, D_2, N_2, O_2, N_2O, CO_2, SF_6, CH_4, C_2H_2, C_2H_4, C_2H_6, C_3H_8, CH_3F, $CHClF_2$, CCl_2F_2, He+X, Ar+X, and O_2+X (X: additive gas). The strong self-focusing at pressure lower than 5 Torr is attributed to space-charge neutralization by positive ions due to escaping of secondary electrons, produced by direct ionization of the primary beam. Therefore, relative total ionization cross sections for beam electrons could be obtained from the data in this region. When the space-charge neutralization time becomes shorter than a rise time of the pulsed beam, secondary electrons are accelerated by a backward electric field E_z induced by the pulsed beam so that the self-focusing declines abruptly due to electron avalanching by accelerated secondary electrons. The beam is self-focused again gradually with further increasing pressure because of suppression of this avalanching. The avalanching was analyzed self-consistently for He, Ar, H_2, N_2, and CH_4 by a computer simulation in the pressure region between 5 and 300 Torr. The dose estimated from the calculated net current for these gases gives the good correspondence to the observed dose. The present computational results indicate that the larger dose is given by the longer mean ionization time t_i which depends on E_z/p. The value of t_i increases with increasing pressure in the pressure region of gradually-increasing self-focusing because E_z/p decreases with increasing pressure. Since the value of t_i is related theoretically to data on swarm parameters and other molecular data, the information obtained from the simulation gives some approach to estimate ionization or electron avalanching induced by the pulsed beam, from molecular data for gases. At higher pressure (usually above 100 Torr), the self-focusing declines again as a result of a competition between the self-focusing force and the diffusion force of multiple scattering of the primary beam by a background gas.

Keywords: Pulsed Electron Beam, Self-focusing, Gas Ionization, Electrical Breakdown, Ionization Time, Discharge Chemistry, Electron Avalanching

+ Division of Development, Takasaki Radiation Chemistry Research Establishment
* Fukui Institute of Technology, Fukui 910

各種気体中でのパルス電子線の自己集束性と
気体イオン化過程の研究

——放電化学への新しいアプローチ——

日本原子力研究所高崎研究所研究部

堀田　寛* ・ 新井英彦
田中隆一＋ ・ 須永博美＋

要　旨

Febetron 706 の相対論的大強度のパルス電子線は，5 Torr 以下と以上の2つの圧力域で強い集束性を示した．He 中でのこの電子線のエネルギースペクトルの，圧力および通過距離依存性を，アルミニウム・ブルーセロハン積層線量計の深部線量分布から検討した．セルの照射窓より 10.4 cm のビーム軸上に置いた線量計で求めた深部線量曲線の極大線量値を，気体圧の関数として，He, Ne, Ar, Kr, Xe, H_2, D_2, N_2, O_2, N_2O, CO_2, SF_6, CH_4, C_2H_2, C_2H_4, C_2H_6, C_3H_8, CH_3F, $CHClF_2$, CCl_2F_2, He+X, Ar+X および O_2+X （X は添加気体）について測定した．5 Torr 以下での強い集束性は，入射ビームの直接イオン化で生じた二次電子の逸散により，正イオンが空間電荷を中和するためである．この関係より 5 Torr 以下のデータからビーム電子に対する相対的全イオン化断面積を求めることができた．空間電荷の中和時間がパルスの立ち上り時間より短くなると，二次電子はパルスビームの逆電場 E_z により加速され，電子なだれが起きる．この結果，自己集束性は急速に崩壊する．さらに圧力を増すと，電子なだれが抑えられるため，ビームは再び徐々に自己集束性を増す．この電子なだれ機構を，5～300 Torr の He, Ar, H_2, N_2 および CH_4 について電子計算機によるシュミレーションから解析した．これらの気体について正味電流の計算値から求めた線量は，観測値とよく対応した．これらの計算結果から，E_z/P 依存性をもつ平均イオン化時間 t_i が長いほど大きな線量が与えられることがわかった．E_z/P は圧力の増加と共に減少するので，自己集束性が次第に増加する圧力域では，t_i 値は圧力の増加と共に増加する．t_i 値は理論的にスウォームパラメーター値および他の分子論的データと関係しているので，シミュレーションから得られた知見は，気体の分子論的データから，パルスビームによって起きるイオン化あるいは電子なだれを推定する手がかりを与える．さらに高い圧力（通常 100 Torr 以上）では，自己集束力と気体による一次ビームの多重散乱による発散力との競合の結果，自己集束性が減少する．

＋ 高崎研究所開発部
* 〒910　福井市 福井工業大学

Contents

<div align="center">

目　　　次

</div>

1. Preface

A Febetron 706 of Field Emission Corporation was placed in our laboratory in 1971 as a generator of a pulsed electron beam. We have been interested in the self-focusing of the beam as a result of the preliminary experiment[1] in the hope that some physico-chemical information must be obtained from the study of the self-focusing in various gases. At first, the experimental results concerning the self-focusing phenomena[2-6] were analyzed on the basis of the simple model[7]. Afterwards, we interpreted the data in the intermediate pressure region (10 – 100 Torr) in terms of gas breakdown time owing to electron avalanching[8,9]. Recently, we interpreted successfully the data on the basis of the revised model by a computer simulation[10-12]. Then, we have been driven by necessity of the preparation of this report to re-examine the whole previous data in view of the new model.

The self-focusing of a relativistic high-intensity pulsed electron beam has been investigated as a field of beam dynamics with the development of large pulsers for various purposes, for example, nuclear fusion, laser, and pulse radiolysis. Recently, Yonas and Toepfer[13] have reviewed the present status of relativistic-electron-beam produced plasmas. In Chap. 2, the theory of the self-focusing is outlined rather historically in order to elucidate the physical meaning of our study. The model accepted finally by us or the fundamental conception of our analysis is explained in **2.2.3**. Next, the experimental procedures and results are described in Chap. 3. In the present study, the degree of the self-focusing is represented by D_{obs} which is the maximum dose of the depth-dose curve in a stack of aluminum and blue cellophane on the beam axis. The value of D_{obs} is approximately related to the net current which is proportional to the self-focusing force. At first, the self-focusing was studied as a function of pressure of He by using the aluminum-blue cellophane stack at various positions as described in Chap. 4. After that, the stack was always placed at 10.4 cm on the beam axis from the window of the irradiation cell filled with various gases because the end-plate effect and the background dose could be neglected practically at this position in He. Then, the data of D_{obs} in Chap. 3, used for the present discussion, were obtained from the experiments using the stack at 10.4 cm like this.

As described in Chap. 5, the beam is affected only by ionization caused by the primary beam in the pressure region below 5 Torr. We found that, for such a case, the relative total ionization cross section for the primary beam can be obtained through the measurement of D_{obs}. With increasing pressure, secondary electrons are much produced by an induced electric field E_z of a pulsed beam. Then, the beam is strongly affected by this secondary ionization or E_z. The scheme for the estimation of such electron production and its effect is explained in Chap. 6.

The numerical analysis according to this scheme was carried out by the use of an electronic computer for He, Ar, H_2, N_2, and CH_4 for which the related swarm parameters were known completely. Although processes in a gas are not always in equilibrium for an extremely abrupt change of E_z, data on swarm parameters given as functions of E/p were used without any correction even for such a case. Nevertheless, the data on D_{obs} could be interpreted fairly well by the computational results as shown in Chaps. 7, 8, and 9. This means that the computational model in Chap. 6 is adequate so that data on various parameters obtained by the computation, for example, the value of E/p, the density of secondary electrons and so on, which are not easy to be measured directly, represent semi-quantitatively ionization caused

by the pulsed beam. Furthermore, data on D_{obs} for various gases other than five ones could be interpreted on the basis of the conclusion from the above computation. In Chap. 10, the conclusion could be applicable to the binary mixtures with He, Ar, and O_2 for which the related data are sparse. Consequently, we can say that the value of D_{obs} obtained from the simpler method can give information on ionization during the pulse or at E/p induced by the pulsed beam. Especially, this method is very valuable for mixtures because the related data are usually imperfectly known.

The beam is multiply scattered at higher pressure as shown in Chap. 11. The results obtained in the present study are summarized in Chap. 12. Symbols used in this report are listed at the end of volume.

The beam-plasma interaction has been analyzed physically for some lower-pressure gases such as He, Ar, N_2, and air. For example, the net current of a pulsed beam has been analyzed numerically, at highest, up to 20 Torr by a computer simulation[14-16]. Miller, Gerardo, and Poukey[17,18] have observed the current-wave form of pulsed electron beam with a Faraday cup placed at about 1 m from a chamber window in some gases of 0.001 to 300 Torr to obtain the relationship between the observed current and gas properties. However, they have hardly discussed the detailed molecular processes in the plasma. Recently, the molecular processes induced by a pulsed beam in higher-pressure gases have been much studied in the field of discharge and laser chemistries[13,19-22]. As pointed out already, the early processes during the pulse are affected by the induced electric field E_z, the effect of which is reflected in the value of D_{obs} obtained in the present study. Therefore, our results can give useful information for these fields and also on the mechanisms of ionization chamber, gas breakdown, and its inhibition.

We found from the present study that the state of a pulsed beam, namely, the beam density and the value of E/p, is quite different among the pressure ranges of a background gas. Therefore, the chemical effect of a pulsed beam on gaseous media is not simply proportional to gas pressure. The pressure dependence of radiation-chemical yields in some gases irradiated by a Febetron 706 has been reported by Willis, Boyd, and Miller[23] who have unnoticed this effect.

2. Theory of Self-focusing

2.1 General Formulation of Beam Behavior

2.1.1 Steady electron beam

Suppose that a cylindrical steady electron beam of radius r_0 propagates with velocity $v_b = \beta c$ (c: light velocity) along z-axis in vacuum. The steady beam means that the electron density is uniform for r- and z-directions at any time and that all the electrons move parallel to z-axis and have no velocity component to r-direction. Since the radially outward electric and magnetic forces (F_e and F_m) on an electron at r from the beam axis are given by

$$F_e = \frac{2N_e c^2 r}{r_0^2} \tag{2.1}$$

and

$$F_m = \frac{2N_e e^2 r}{r_0^2}\beta^2 \tag{2.2}$$

in the Gaussian unit system, the total force F_r is given by

$$F_r = F_e + F_m$$
$$= \frac{2N_e e^2 r}{r_0^2}(1 - \beta^2), \tag{2.3}$$

where N_e is the number of beam electrons per cm. The beam always diverges because of $1 > \beta^2$.

When an irradiation cell is filled with a low-pressure gas, the gas is ionized to give positive ions and secondary electrons. Secondary electrons with light mass are accelerated by F_r and escape from the beam channel. Consequently, the remaining positive ions tend to neutralize the space charge of the primary beam When the electric or space-charge neutralization factor f_e is defined as a ratio of ion density n_i to beam electron density n_b

$$f_e = n_i/n_b, \tag{2.4}$$

F_r becomes as

$$F_r = \frac{2N_e e^2 r}{r_0^2}(1 - f_e - \beta^2) \ (1 \geq f_e \geq 0). \tag{2.5}$$

The concept of the space-charge neutralization factor has been introduced first by Bennett[24] and established by Lawson[25]. According to Lawson, the radial equation of motion for an electron at r in the paraxial beam is given by

$$\frac{d^2r}{dz^2} = \frac{2\nu r}{\gamma\beta^2 r_0^2} \ (1 - f_e - \beta^2) \tag{2.6}$$

and for an electron at the beam surface ($r = r_0$)

$$\left(\frac{d^2r}{dz^2}\right)_{r=r_0} = \frac{2\nu}{\gamma\beta^2 r_0} \ (1 - f_e - \beta^2) \tag{2.7}$$

where $\nu = N_e e^2/m_e c^2$ $\quad$ (m_e: electronic rest mass) $\tag{2.8}$

$$\gamma = 1/(1 - \beta^2)^{1/2}. \tag{2.9}$$

When $f_e > 1 - \beta^2$, the beam is self-focused. When $f_e = 1$, Eq. (2.6) becomes like

$$\frac{d^2r}{dz^2} + 2\left(\frac{\nu r}{\gamma r_0^2}\right) = 0 \tag{2.10}$$

with a sinusoidal solution of wave length λ[25]

$$\lambda = 2\pi r_0 / (2\nu/\gamma)^{\frac{1}{2}}.$$ (2.11)

The space-charge neutralization time t_N is defined as the time at which $f_e \cdot 1$ or $n_i \cdot n_b$, as will be discussed in **5.2**.

2.1.2 Pulsed electron beam

When a pulsed electron beam passes into a cylindrical cell with radius R and length l ($R < l$) filled with gas, the rapid rise of the beam current I_b induces an electric field E_z. A backward plasma current I_{back} of secondary electrons induced by E_z reduces the magnetic force F_m. This E_z on the beam axis is given by

$$E_z \cdot -\frac{1}{c} \int_0^R \frac{dB_\theta}{dt}\, dr$$

$$= \frac{2}{c^2}\frac{dI_b}{dt}\left(\int_0^{r_0}\frac{r}{r_0^2}\, dr + \int_{r_0}^R \frac{1}{r}\, dr\right)$$

$$\frac{2}{c^2}\frac{dI_b}{dt}\left(\frac{1}{2} + \ln\frac{R}{r_0}\right)$$ (2.12)

when end-plate effects become negligibly small; according to Putnam[26], this condition is realized at z like

$$z > R/2.4 \qquad \text{(cm)}$$ (2.13)

where z is scaled from the cell window. In Eq. (2.12), the magnetic flux B_θ is given as the magnetic field H_θ in the Gaussian unit system like

$$B_\theta - H_\theta - \frac{2N_e e v_b\, r}{c\, r_0^2}\; (0 < r < r_0)$$ (2.14a)

and

$$= \frac{2N_e v_b}{cr}\quad (r_0 \leq r).$$ (2.14b)

When the magnetic or current neutralization factor f_m is defined as

$$f_m = I_{back}/I_b,$$ (2.15)

Eqs. (2.5) and (2.6) become like[7,27]

$$F_r = \frac{2N_e e^2 r}{r_0^2}[1 - f_e - \beta^2(1 - f_m)]$$ (2.16)

and

$$\frac{d^2 r}{dz^2} = \frac{2\nu r}{\gamma\beta^2 r_0^2}[1 - f_e - \beta^2(1 - f_m)].$$ (2.17)

The ratio of ν/γ, called the Budker parameter, serves as a convenient measure for classifying the properties of intense beams;

$$\nu/\gamma = I_b/(17000\beta\gamma).$$ (2.18)

When the current of a relativistic high-intensity beam exceeds the Alfvén current limit $(17000\ \beta\gamma)$[28], some electrons of the beam cannot propagate forward due to the Lamor motion induced by the self-magnetic field at the beam surface. According to Yonas and Spence[29], the beam with $\nu/\gamma > 1$ can propagate when the above magnetic neutralization occurs.

2.2 Net Current of Pulsed Beam

2.2.1 The t_B model of net current

Although the assumption of uniformity and paraxiallism is not always realized for a practical beam, the dependence of the self-focusing on gas pressure can be interpreted quali-

tatively in terms of f_e and f_m in Eq. (2.16)[7]. The beam is self-focused the most strongly for $f_e = 1$ and $f_m = 0$. However, values of f_e and f_m vary with the lapse of time[9]. Therefore, the finer model is necessary to analyze the self-focusing quantitatively.

Putnam[26] proposed first that electron avalanching occurs after perfect space-charge neutralization. Secondary electrons are accelerated up to near light velocity to radial direction when $f_e \ll 1$ or $t \ll t_N$. Such fast electrons have few chances of electron avalanching because of small ionization cross section for high-energy electrons and a very low pressure. Once f_e becomes unity, the axial backward field E_z becomes predominant and the radial field becomes negligibly small so that electron avalanching induced by E_z becomes appreciable.

According to Yonas et al.[27], a time delay is required for build-up of a secondary electron density high enough to produce substantial current neutralization. This time delay is called the breakdown time t_B of a background gas under E_z. When the schematic beam profile is shown in **Fig. 2.1**, as a first approximation, and increase in I_b is cancelled by $I_{back}(<0)$ after t_B; the net current I_{net} defined by

$$I_{net} = I_b + I_{back} \qquad\qquad (2.19)$$

remains equal to the value of $I_b(t_B)$ as seen in **Fig. 2.1**. This model will be called the t_B model of I_{net}. The value of I_{back} is negative for $dI_b/dt > 0$. The decline of the self-focusing in the intermediate pressure region is attributed to this gas breakdown. At first, we analyzed our data on D_{obs} on the basis of this model[8]. Although the experimental results could be analyzed by the t_B model without using an electronic computer, the whole data could not be interpreted perfectly in terms of such a t_B.
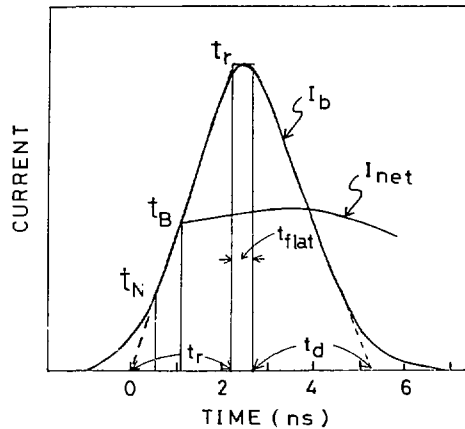
Fig. 2.1   The schematic pulsed-beam current profile used for
the present study.

2.2.2 Computation of net current

Swain[14] calculated self-consistently the plasma conductivity and the electric field induced by 2-MeV 4-kA beam of 100 ns duration on the basis of a model which includes (a) direct ionization of gas by the high-energy beam electrons and (b) secondary ionization of gas caused by acceleration of secondary electrons by E_z induced by the pulsed beam. For the beam injected into He at 0.2−2.0 Torr, his computational results agree with experimental results at lower pressures but tend to deviate from the experimental at higher pressures.

McArthur and Poukey[15,16] calculated I_{net} resulting from 45-kA beam of 3 MeV and

also from a 2-20 kA beam of 0.25-3 MeV, injected into at 1-20 Torr, on the model including detailed atomic processes. Their results agree within ±15% with experimental values.

Since the beam characteristics of our machine are different from their beams, the similar computation is necessary on assumptions conformed to our experiment. Such a computation was carried out to analyze our data on D_{obs} on the basis of the following equation derived by us (Eq. (2.24)).

2.2.3 Basic equations for the present study

A self-consistent equation for a beam envelope has been given by Kapchinskij and Vladimirskij[30] as

$$\left(\frac{d^2 r}{dz^2}\right)_{r=r_0} = -\frac{A}{r_0} + \frac{\varepsilon_b}{r_0^3}$$ (2.20)

where

$$A = \frac{2 I_{net} e}{m_e r c^3 \beta^3} (1 - f_e - \beta^2)$$ (2.21)

$\pi \varepsilon_b$ beam emittance;

the first term represents the self-focusing and the second term the dispersion or defocusing. This equation for a uniform and paraxial beam has been solved numerically in a dimensionless form for a general form[31]. For the steady-state uniform beam $(d^2r_0/dz^2 = 0)$, the envelope radius is given by

$$r_0 = \varepsilon_b/\sqrt{|A|} \quad (A < 0).$$ (2.22)

Therefore, we can obtain the relationship from Eqs. (2.21) and (2.22) as

$$r_0 \propto \varepsilon_b/\sqrt{|I_{net}(1 - f_e - \beta^2)|}.$$ (2.23)

In the present study, the degree of the self-focusing is measured as the maximum dose of the depth-dose curve D_{obs} in the dosimeter placed on the beam axis, as will be explained in **3.3**. When this D_{obs} is assumed as

$$D_{obs} \propto \int \frac{I_b(t)}{\pi r_0^2} dt,$$ (2.24)

D_{obs} can be expressed from Eq. (2.23) by[9]

$$D_{obs} \propto \int \frac{I_b(t) I_{net}(t)(1 - f_e - \beta^2)}{\varepsilon_b^2} dt.$$ (2.25)

When $t_N \approx 0$ at higher pressure, Eq. (2.25) becomes like

$$D_{obs} \propto \int \frac{I_b(t) I_{net}(t)\beta^2}{\varepsilon_b^2} dt$$ (2.26)

because of $f_e = 1$. The value of I_{net} is proportional to the self-focusing force F_r because

$$F_r = -\frac{2 e r \beta}{c r_0^2} I_{net} = -e \beta H_\theta$$ (2.27)

from Eq. (2.16) when $I_{net} = e N_e v_b (1 - f_m)$ and $f_e = 1$.

Therefore, when the value of $I_{net}(t)$ is estimated by using data on properties of a gas, our data on $D_{obs}(p)$ can be analyzed by Eq. (2.26). Such an analysis will be given in **6. – 10**.

2.2.4 Dependence on apparatus

In Eq. (2.12), E_z depends on R/r_0 as well as dI_b/dt. Therefore, gas breakdown due to electron avalanching is suppressed by using a narrower irradiation cell and a mildly rising beam. The result of Miller et al.[17, 18] has not shown the breakdown in the intermediate pressure region in which we found it. Since they used the 1.5 MeV pulsed beam of a Febetron 705 with 3000 A peak current and 20 ns rising time, dI_b/dt must be much smaller for their beam than for our beam.

2.3 Ion Acceleration

Graybill and Uglum[32] demonstrated that a pulsed electron beam can accelerate light ions to high energies to the same direction with the beam. According to Olson[33,34], ion avalanching via ion acceleration is induced in a low-pressure gas by an intense relativistic electron beam when I_b is larger than the space-charge limitting current I_L given by

$$I_L = \beta(\gamma - 1)(m_e c^3/e)(1 + 2\ln R/r_0)^{-1}(1 - f_e)^{-1}. \qquad (2.28)$$

For the self-focusing beam, I_L increases with increasing f_e and. for the self-defocusing beam, I_L also increases with increasing r_0. Then, the value of I_L seems to be always larger than 8000 A (the maximum I_b for our machine). Therefore, ion avalanching can be neglected at least for the phenomenon discussed in this report.

3. Experimental Procedures and Results

3.1 Pulsed Electron Generator

A Febetron 706 (tube 5515) manufactured by Field Emission Corp., U.S.A. was used as a pulsed electron beam generator. The nominal characteristics of tube 5515 announced by the maker are listed in **Table 3.1**. The beam profile from an oscilloscopic tracing is shown schematically in **Fig. 2.1** as shown already in **2.2.1**. When the rise time t_r is defined as shown by dotted lines in **Fig. 2.1**, t_r = 2.2 ns. The definitions of other symbols in **Fig. 2.1** will be given in **5.2**. Ling, Weiss, and Epp[35] have reported that the mean energy of this beam is 480 keV. The electron equivalent energy was 625 keV from the extrapolated range of the depth-dose curve in **Fig. 3.4** shown later. Since the out-put energy, measured by calorimetry, was 12 J/pulse, the peak current I^p is estimated to be 8000 A on assumption of the 480 keV mean energy. Then, the maximum electron density at the peak $(I^p/(e\beta c))$ is 1.9 x 10^{12}/cm as β = 0.857. When the beam is assumed to be radially uniform and paraxial, for r_0 = 0.6 cm and R = 6.4 cm, the induced electric and magnetic fields at the beam surface are 9 x 10^5 V/cm and 2700 G for the I^p. The value of E_z from Eq. (2.12) is 2 x 10^4 V/cm for the linearly rising part of the current (I_{back}=0). The value of ν/γ given by Eq. (2.18) is 0.28 for $I_b = I^p$.

Table 3.1 Characteristics of tube 5515

Effective pulse duration	3 nsec
Output energy	11.1 J
Maximum beam fluence	10.1 J/cm^2
Effective beam width	1.2 cm
Maximum peak current density	9000 A/cm^2
Approximate charge density	30 μC/cm^2
Surface dose in aluminum	5.3 Mrad/pulse
Linear range in aluminum	212 mg/cm^2
Electron equivalent energy	625 keV

3.2 Irradiation Cell and Filling of Gases[3]

A stainless-steel cylindrical irradiation cell (SUS 27) which was placed coaxially at the front of the tube face, was 12.8 cm in inner diameter and 25 cm in length and has a stainless-steel window (0.001 cm in thickness and 3.5 cm in diameter) as shown in **Fig. 3.1**. The air space between the cell window and the tube face was 0.8 cm long. Energy loss in this air space is negligibly small (less than 15 keV), while the scattering of the beam in the window may be appreciable. These effects, however, are irrelevant to discussion on the relative change of depth-dose curves at the fixed position which is the main subject in the present study.

After evacuated at least up to 2 x 10^{-4} Torr, the cell was filled with a gas. Gases used were mostly obtained of the purest grade from Takachiho-shoji, Tokyo and used without purification. The pressure was measured with a mercury manometer for above 20 Torr, with a silicone-oil manometer (density = 1.06 g/cm^3) between 1 and 20 Torr, and with a McLeod gauge for below 1 Torr.
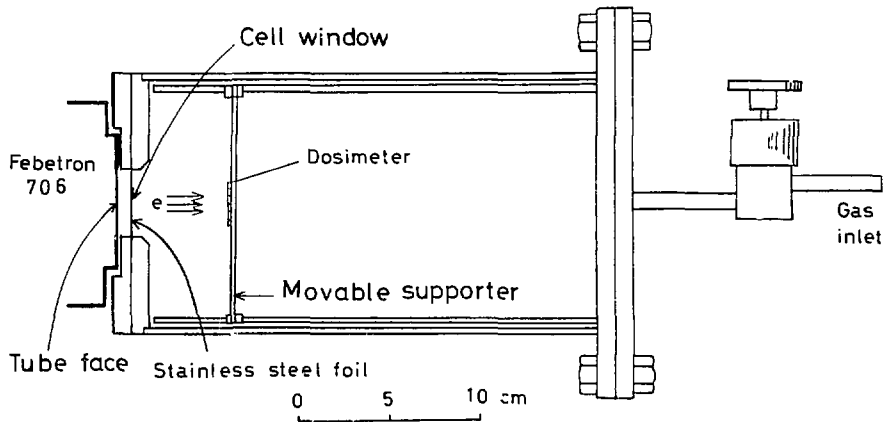
Fig. 3.1   The irradiation cell.

3.3   Aluminum-Blue-Cellophane Dosimeter

A dosimeter was set perpendicularly at 10.4 cm from the cell window on the cell axis
as shown in **Fig. 3.1**. The dosimeter was a 1.2 cm square stack within which aluminum ab-
sorber (15.7 mg/cm²) and Avisco Light Blue Cellophane ribbon (3.8 mg/cm²) were piled
alternately in 13 layers as shown in **Fig. 3.2**. The cellophane ribbon is not so thin as to be
ignored in comparison with aluminum. However, since the difference in stopping power or
mean atomic number between aluminum and cellophane is relatively small, the depth-dose
curve by means of the following method approximately shows the curve in aluminum.

Before and after irradiation, a cellophane ribbon folded in the stack was extended, and
its optical density at 655 nm was read by scanning of the ribbon with a NARUMI micro-
spectrophotometer as shown in **Fig. 3.3**, in which typical results for the focused (A) and
defocused (B) beams are shown. The maximum change (C) of the optical density after irradia-
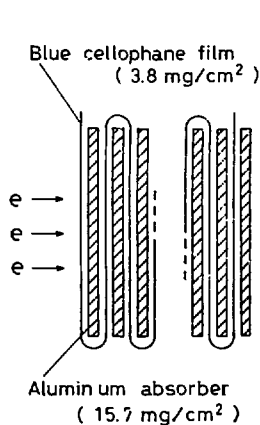
Fig. 3.2   The aluminum-blue
cellophane piled dosi-
meter.
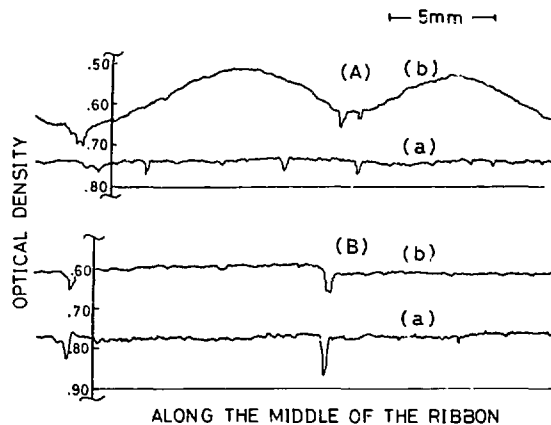
Fig. 3.3   Scanning of the optical density of the blue
cellophane ribbon at 655 nm before (a) and
after (b) irradiation. The self-focused (A) and
defocused beam (B).

tion (b) from before irradiation (a) in the scanning curve corresponds to the dose on the beam axis. The absorbed dose (D(Mrad)) is obtained from C by equation

$$D = 331\,C^4 - 197\,C^3 + 65.9\,C^2 + 9.12\,C \qquad (3.1)$$

which was obtained experimentally[1]. The scanning cannot always run on the same position correctly before and after irradiation. Therefore, the uncertainty of C may be 0.01 at largest as an optical density, which is equivalent to about 0.01 Mrad, including instrumental errors. Then, for the strongly defocused beam, several pulses were shooted to a single dosimeter to reduce the uncertainty of the background dose.

A depth-dose curve is obtained when such a dose on the beam axis at each depth is plotted against depth. The curve in **Fig. 3.4** was obtained for the dosimeter placed in air at 1 cm from the tube face. As seen in **Fig. 3.4**, the curve becomes the maximum usually at the third layer. The maximum value of the depth-dose curve D_{obs} is used as a measure of the self-focusing for the present study.

3.4 Results for Various Gases

When values of D_{obs} are plotted against gas pressure, a curve is obtained for a certain gas. Such curves for various gases observed at 10.4 cm on the beam axis from the cell window are shown in **Figs. 3.5 3.13**[3,4,5]. As seen in these figures, the beam is hardly self-focused in the intermediate pressure region (usually around 5 10 Torr), in which D_{obs} decreases down to 0.2 Mrad. Therefore, the position at 10.4 cm is very suitable for the study of the self-focusing because of such a low background dose and also of disappearance of the end-plate effect from Eq. (2.13). Data for n-C_4H_{10}, cis-2-C_4H_8, n-C_5H_{12}, and neo-C_5H_{12} have been published else-where[5].
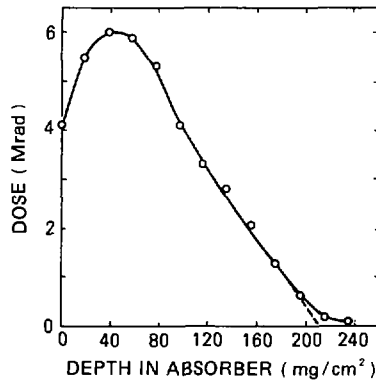
Fig. 3.4   The depth-dose curve in the dosimeter placed at
1 cm from the tube window in atmospheric air.
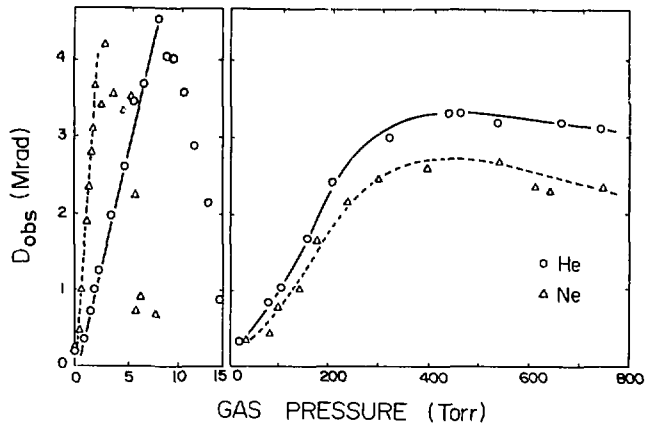
Fig. 3.5   Values of D_{obs} at 10.4 cm on the beam axis from the cell window in He
(○) and Ne (△).
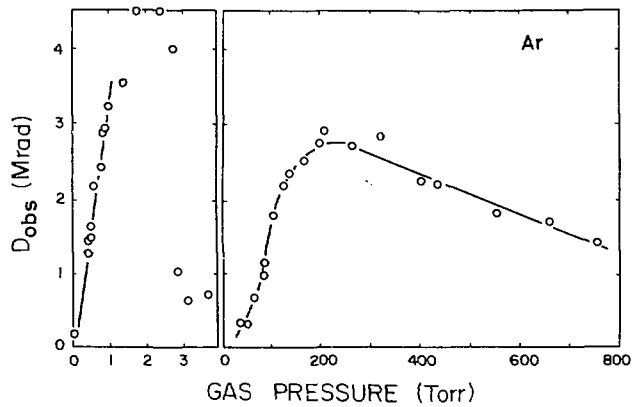
Fig. 3.6   Values of D_{obs} at 10.4 cm on the beam axis from the cell window in Ar.
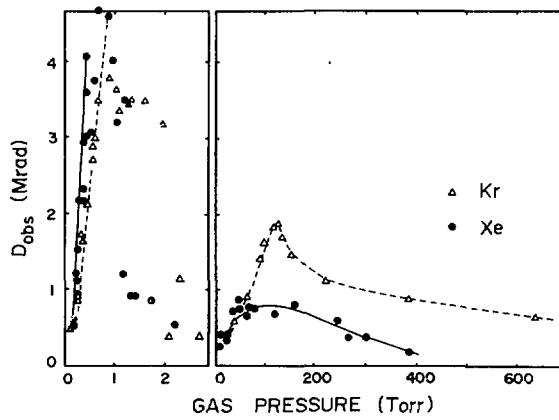
Fig. 3.7   Values of D_{obs} at 10.4 cm on the beam axis from the cell window in Kr ($\triangle$) and Xe ($\bullet$).
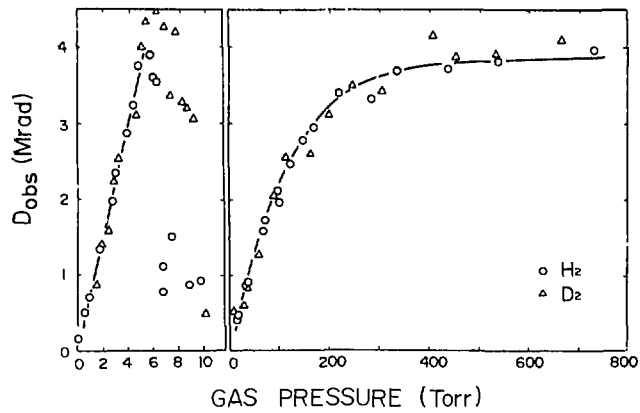
Fig. 3.8   Values of D_{obs} at 10.4 cm on the beam axis from the cell window in H_2 ($\circ$) and D_2 ($\triangle$).
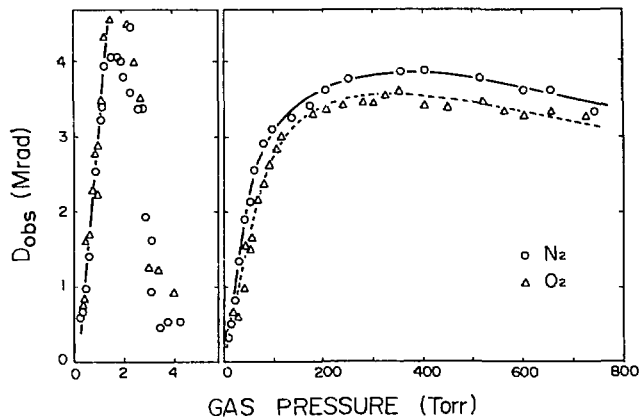
Fig. 3.9   Values of D_{obs} at 10.4 cm on the beam axis from the cell window in N_2 ($\circ$) and O_2 ($\triangle$).
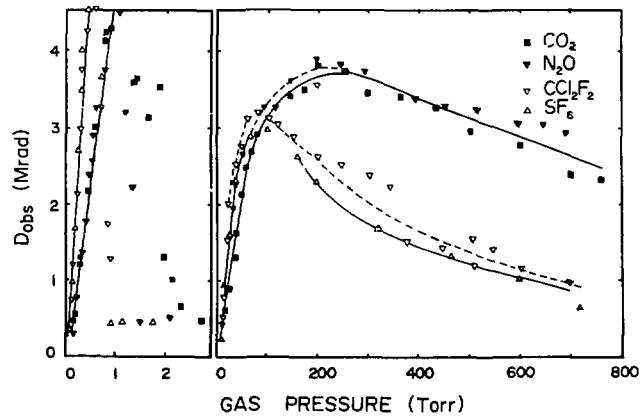
Fig. 3.10   Values of D_{obs} at 10.4 cm on the beam axis from the cell window in CO_2 (■), N_2O (▲), SF_6 (△), and CCl_2F_2 (▽).
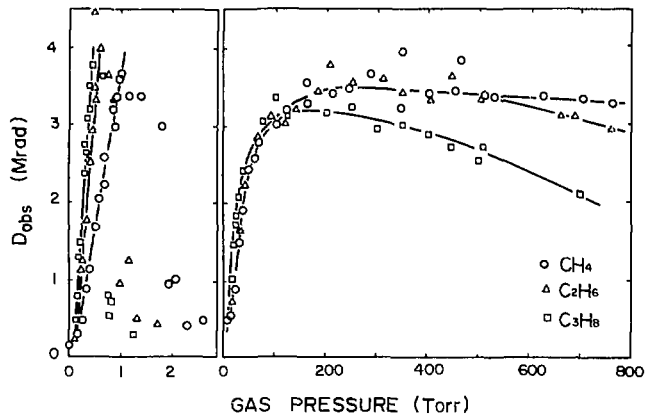
Fig. 3.11   Values of D_{obs} at 10.4 cm on the beam axis from the cell window in CH_4 (○), C_2H_6 (△), and C_3H_8 (□).
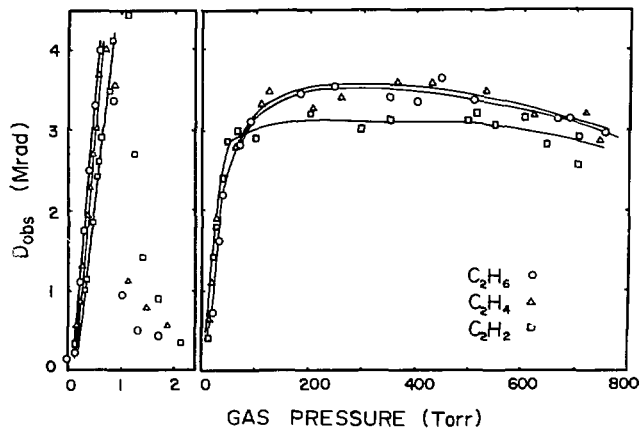
Fig. 3.12   Values of D_{obs} at 10.4 cm on the beam axis from the cell window in C_2H_2 (□), C_2H_4 (△), and C_2H_6 (○).
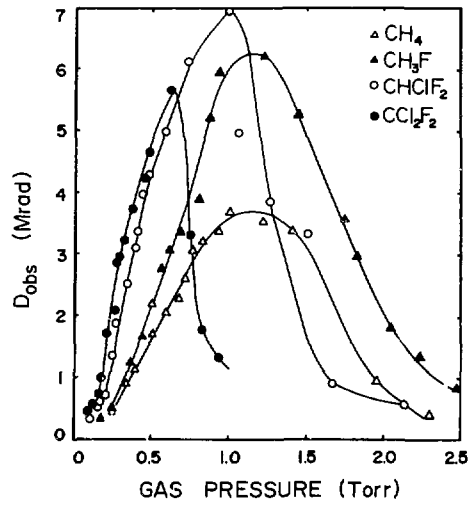
(a)
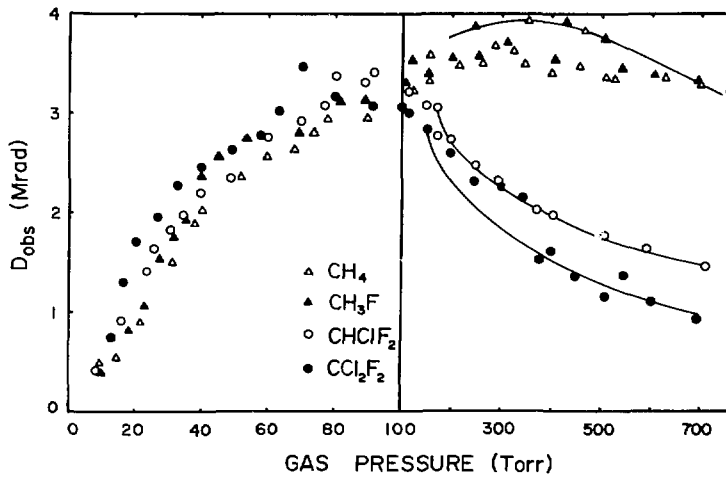
(b)

Fig. 3.13 (a) and (b) Values of D_{obs} at 10.4 cm on the beam axis from the cell window in CH_4 ($\triangle$), CH_3F ($\blacktriangle$), $CHClF_2$ ($\bigcirc$), and CCl_2F_2 ($\bullet$).

4. Self-focusing in Helium

4.1 Introduction

Before the self focusing was studied in various gases at the same position as described in **3.2**, the depth-dose distribution in the dosimeter had been studied in detail in helium with a glass cylindrical irradiation cell (30 cm in diameter and 40 cm in depth[2]) larger than the cell used for various gases. Such a large glass cell was used with the intention of observing the beam profile and avoiding the wall effect. After this experimentation, the smaller cell as shown in **Fig. 3.1** was used to save evacuation time and the cost of a sample gas.

A depth-dose curve was determined by the energy spectrum of electrons and/or by the distribution of their incident angle to the surface of the dosimeter (aluminum). It is difficult to distinguish the contribution of each effect from the shape of the curve. The increase of the incident angle gives the curve as if the composition of lower-energy electrons increases. Yonas et al.[27] attempted to analyze the effect of the incident angle on depth-dose distributions by a Monte-Carlo method. Despite of great interest in the dependence of the beam behavior on gas pressure, the depth-dose distribution in an irradiated solid sample has never been studied experimentally as a function of pressure of gaseous atmosphere. Since helium has the smallest cross sections of elastic scattering and collisional energy loss, this gas is the most suitable for study on the electromagnetic properties of a high-intensity relativistic electron beam. The collisional energy loss during traverse of 30 cm is at most 10 keV even at one atmospheric pressure.

The maximum and extrapolated ranges, which are usually defined for a number-transmission curve of electrons, may be defined similarly for the present depth-dose curve. For monoenergetic beam, the extrapolated range is nearly equal to the maximum range. When the extrapolated range is extremely short in comparison with the maximum range, the fraction of lower-energy components should be relatively large in the beam. The extrapolated range for a normally incident beam can be used as a relative measure for the kinetic energy of the predominant part of electrons in the beam.

Results observed as functions of helium pressure and distance from the cell window had been discussed previously mainly in terms of f_e, f_m, and E_z (Eqs. (2.12) and (2.16))[2]. Since the model has been revised afterwards as described in **2.2.3**[10,11], the dependence of the dose on pressure must be interpreted as referring to the discussion which will be described in the following chapters. On the other hand, it is concluded in this chapter that the variation of the energy spectrum with distance is attributed mainly to degradation by E_z induced by the end plate effect near the inlet of the cell, given by the following equation[26].

$$E_z(0,z,t) = -\overbrace{2\frac{\partial N_e}{\partial z}\left(\frac{1}{2}+\ln\left(\frac{R}{r_0}\right)\right)\frac{4z(l-z)}{l^2}}^{(1)} + \overbrace{\frac{2N_e}{r_0}\frac{\partial r_0}{\partial z}\left(\frac{4z(l-z)}{l^2}\right)}^{(2)}$$

$$-\overbrace{2N_e\left(\frac{1}{2}+\ln\left(\frac{R}{r_0}\right)\right)\frac{4(l-2z)}{l^2}}^{(3)} - \overbrace{\frac{2}{c^2}\frac{\partial I_b}{\partial t}\left(\frac{1}{2}+\ln\left(\frac{R}{r_0}\right)\right)}^{(4)}$$

$$+\overbrace{\frac{2}{c^2}\cdot\frac{I_b}{r_0}\frac{\partial r_0}{\partial t}}^{(5)} \qquad\qquad\qquad (4.1)$$

where l is the length of the chamber. The first three terms are due to the end plate effect as described below; the terms of the above equation are identified as follows:

(1) Electrostatic due to a variation in the beam charge/length modulated by end plate surface charges,

(2) Electrostatic due to a variation of the beam radius with z modulated by end plate surface charges,

(3) Electrostatic due to induced (positive) surface charges at the end plates which terminate the field lines of adjacent (negative) charges,

(4) Changing magnetic flux due to current variation,

(5) Changing magnetic flux due to containment of current within a time varying radius.

4.2 Results and Discussion[2]

4.2.1 Dosimeter

Doses at 10, 20, and 30 cm from the cell window at 0.01 and 50 Torr were too small to be determined precisely by the blue-cellophane dosimeter. For these cases in **Figs. 4.4** and **4.5**, small thermoluminescence dosimeters, ultra-thin LiF-Teflon disks (Teledyne Isotopes UT-LIF-7) (4.7 mg/cm^2) were used instead. Differences of stopping power and mean atomic number are smaller between aluminum and this disk than between aluminum and blue cellophane. For **Figs. 4.7** and **4.8**, disks of Teledyne Isotopes LIF-7 (27 mg/cm^2, 5 mm in diameter) were piled alone without aluminum absorbers.

Since the doses between 2 and 30 cm at 0.01 and 50 Torr respectively changed so much as seen **Fig. 4.2**, the curves at these pressures were normalized at the maximum point of the curve. Therefore, the data are shown by relative values for 0.01 and 50 Torr and by direct values for 10 and 655 Torr.

4.2.2 Dependence on pressure and distance

The maximum value of the depth-dose curves at 10 cm from the cell window, obtained by the procedure as described in **3.3**, is plotted against helium pressure in **Fig. 4.1**. The similar quantities at 0.01, 10, 50, and 655 Torr are shown as functions of distance from the cell
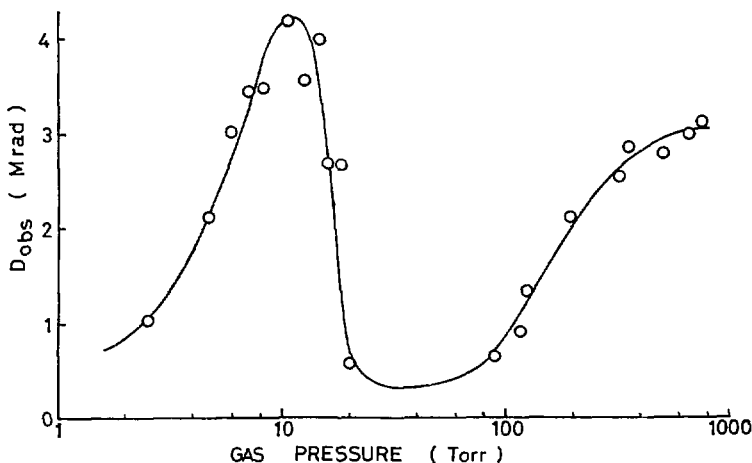
Fig. 4.1   Maximum doses of the depth-dose curve at 10 cm as a function of helium pressure.
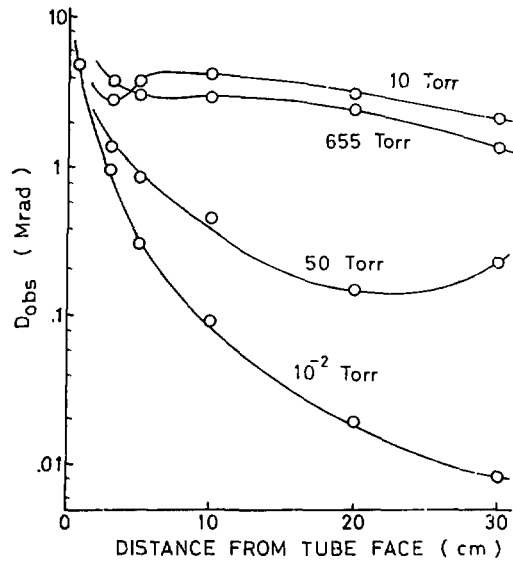
Fig. 4.2   Maximum doses of the depth-dose curve as functions of distance from the cell window at 0.01, 10, 50, and 655 Torr.
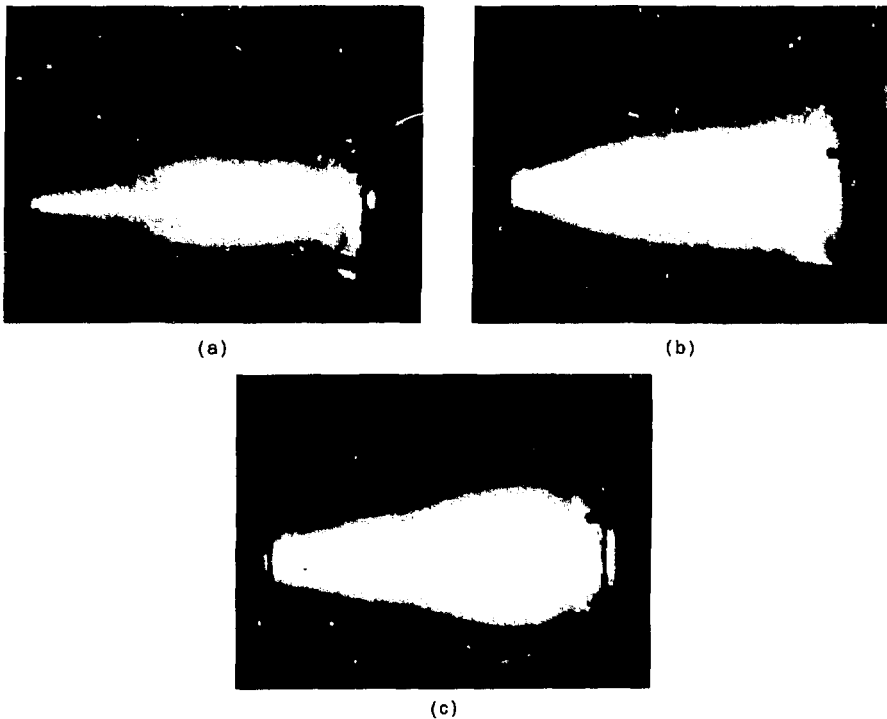
Fig. 4.3   Photographs of the beam profile in helium at (a) 10 Torr (f = 22), (b) 60 Torr (f = 22), and (c) 600 Torr (f = 32).

window in **Fig. 4.2**. These four pressures represent the peaks and the bottoms in **Fig. 4.1**. Photographs of the beam trajectory profile at these pressures were taken by polaroid film (ASA 10000) as shown in **Fig. 4.3** by using emission from helium. That at 0.01 Torr could not be taken because of weak emission. Since the emission strength increases with pressure, the electron density cannot be compared directly between photographs. It is remarkable that we can see a core in the photographs at 10 and 600 Torr and not for that at 60 Torr; there is a nodal structure for the self-focused beam. It is concluded from these facts that the beam is strongly self-focused at two peaks and defocused at the bottoms of the curve in **Fig. 4.1**. The minimums of the curve at 10 and 50 Torr in **Fig. 4.2** are attributed to the nodal structure predicted by the Lawson's theory[25] (Eq. (2.11)).

4.2.3 Defocusing below 1 Torr

The depth-dose curves at 0.01 Torr at various distances from the cell window are plotted as relative dose in **Fig. 4.4**. The maximum range does not decrease appreciably with distance, but the extrapolated range shown by dotted lines decreases abruptly as far as 10 cm and becomes almost constant at larger distances. The space charge is hardly neutralized during the pulse ($t_N{}^{*a)} \gg t_r$ and $f_e \approx 0$) because $\sigma_{ion}(480 \text{ keV})$ for He $= 1.98 \times 10^{-19} \text{ cm}^2$ [36]. Therefore, the beam diverges with distance as seen in **Fig. 4.2**, so that E_z in Eq. (4.1) is reduced. Furthermore, the charge on the end plate affects strongly to E_z near the cell window and the effect decreases rapidly with z[26]; this end-plate effect becomes negligibly small at 7 cm from Eq. (2.13) ($R = 15$ cm). Consequently, the beam energy is degraded strongly by E_z only near the cell window. The degradation is integrated with distance as far as 7 cm and becomes constant far from 7 cm as shown as the extrapolated range in **Fig. 4.4**. These effects are represented by the depression of the curve from A to B, C, and D.

A	▵	0.8 cm
B	▲	3.2 cm
C	○	5.0 cm
D	●	10 cm
D	○	20 cm
D	●	30 cm
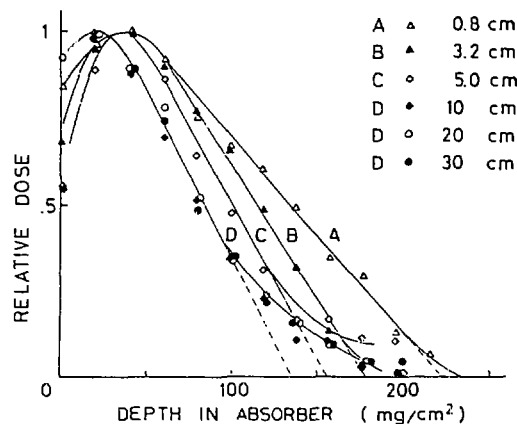
Fig. 4.4   Depth-dose curves, normalized at the maximum point, in He of 0.01 Torr on the beam axis at various positions.

4.2.4 Self-focusing near 10 Torr

The depth-dose curves at 10 Torr are shown in **Fig. 4.5**. As seen in **Fig. 4.2**, the dose does not so decrease with distance as at 0.01 Torr, because the defocusing force is weak. At 10 Torr, $t_N = 1.2 \text{ ns}^{*a)}$ and the end-plate effect disappears after t_N. Consequently, the beam

---

*a) The function for t_N will be given as Eq. (5.10) in **5.2**.
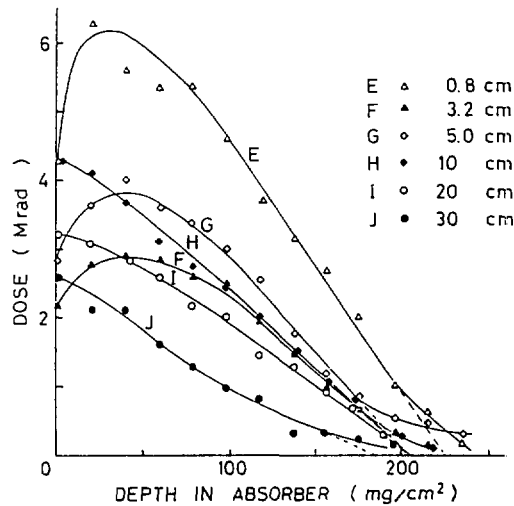
Fig. 4.5   Depth-dose curve in He of 10 Torr on the beam axis
            at various positions.

energy is not so degraded at 10 Torr as at 0.01 Torr as shown by the extrapolated range in **Fig. 4.5**.

The surface dose is the highest of the depth-dose curve at 10 cm and beyond. This is attributed to the increasing fraction of lower-energy components on the beam axis at larger distances. On the other hand, according to Lawson[25], the wavelength of the sinusoidal motion of electrons is given by Eq. (2.11) on assumption of no collisional energy loss. In Lawson's model, electrons with lower energy must come back to the beam axis at a certain distance. The highest surface dose at and beyond 10 cm in **Fig. 4.5** and the maximum of the curve at 10 Torr near 10 cm in **Fig. 4.2** may suggest that, in this region, lower-energy electrons come back to the beam axis more easily than higher-energy ones although the total electron density is reduced with distance. Since the diverging force is strong at 0.01 Torr, such relative enrichment of lower-energy electrons does not occur as seen in **Fig. 4.4**.

4.2.5 Defocusing near 50 Torr

The depth-dose curves, normalized at the maximum point of the curve, at 50 Torr are shown in **Fig. 4.6**. The extrapolated range decreases gradually with distance and the maximum point of the curve approaches the surface with distance. These tendencies are quite different from those at 0.01 Torr, despite of the similar defocusing. The defocusing at 50 Torr is due to electron avalanching as discussed in **7.** not due to the strong interaction among beam electrons as at 0.01 Torr. At 50 Torr, $t_N = 0.2$ ns[*a)]. Consequently, the greater part of the beam traverses under very weak E_z and F_r so as to be defocused without degradation of the beam energy.

We measured the depth-dose curves at 2, 4, and 6 cm off the axis at 10, 20, and 30 cm respectively from the cell window at the same time at those on the axis. The results on the axis are shown in **Fig. 4.7.** The depth-dose curves, normalized at the maximum point of the curve, at 20 cm on and off the axis are shown in **Fig. 4.8**. The similar result was obtained at 30 cm, while there was no appreciable difference between on and off the axis at 10 cm. In Eq. (2.11), lower-energy electrons must come back to the beam axis at shorter distance. However, they come back at larger distance near 50 Torr because of the weak self-focusing. Then, lower-energy electrons seem to be relatively much concentrated on the beam axis at larger distance.
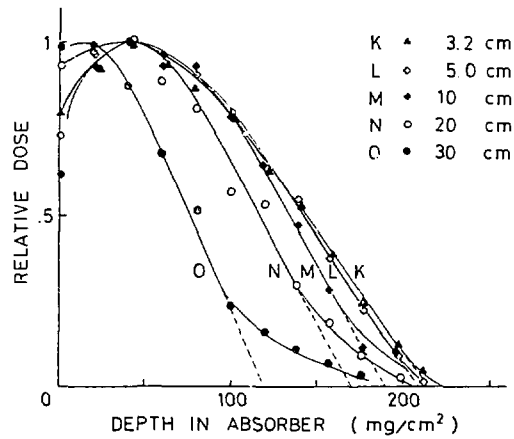
Fig. 4.6   Depth-dose curves, normalized at the maximum point, in He of 50 Torr on the beam axis at various positions.
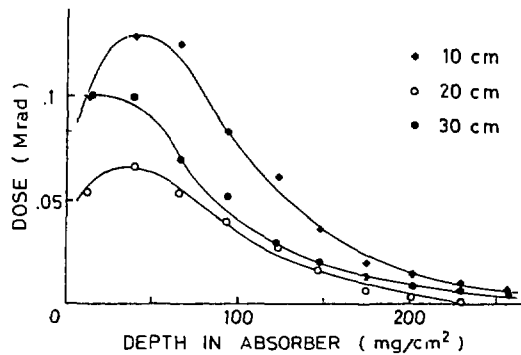
Fig. 4.7   Depth-dose curves in a thermoluminescence dosimeter in He of 50 Torr on the beam axis at 10, 20, and 30 cm.
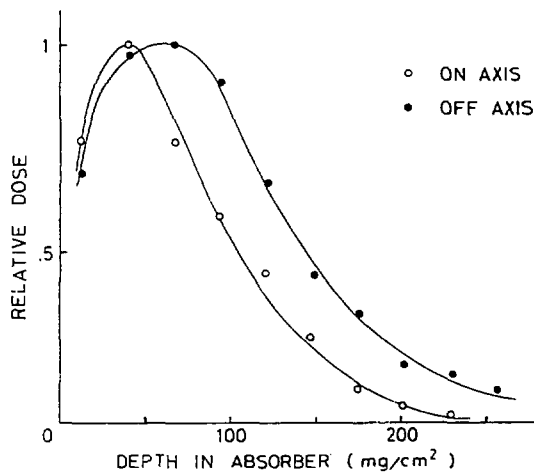
Fig. 4.8   Depth-dose curves in a thermoluminescence dosimeter, normalized at the maximum point, in He of 50 Torr on and off the beam axis at 20 cm from the cell window.

The high surface dose of the curves at larger distances in **Fig. 4.6** suggests also such enrich-ment. The minimum of the curve at 50 Torr in **Fig. 4.2** as well as the above relative enrich-ment can be explained by the sinusoidal motion described in **4.2.4**. As predicted qualitatively by Eq. (2.11), the wavelength is larger at 50 Torr than at 10 Torr because r_0 is large for the defocused beam.

4.2.6 Self-focusing at 655 Torr

The depth-dose curves at 655 Torr are shown in **Fig. 4.9**. The extrapolated range de-creases monotonically with distance in contrast with the result of the similar self-focused beam at 10 Torr. The self-focusing at 655 Torr will be discussed in detail in Chap. 7.

Another difference between 10 and 655 Torr is the surface dose at 10 cm and beyond which is not the highest at 655 as at 10 Torr. When the depth-dose curves at 1 cm on and off the axis were normalized at their maximum points, they were almost the same between the both positions at 10, 20 and 30 cm from the tube face. These facts show that the relative enrichment of lower-energy electrons does not occur at 655 Torr.

In a higher pressure gas, the sinusoidal motion of beam electrons as seen at 10 Torr is impossible owing to collisional scattering by the background gas, and higher-energy electrons are degraded with distance. Therefore, the enrichment does not occur and the extrapolated range decreases with distance. Although the collisional scattering with He competes with the self-focusing force, the former effect is not so appreciable in He as in heavier gases (Chap. 11).
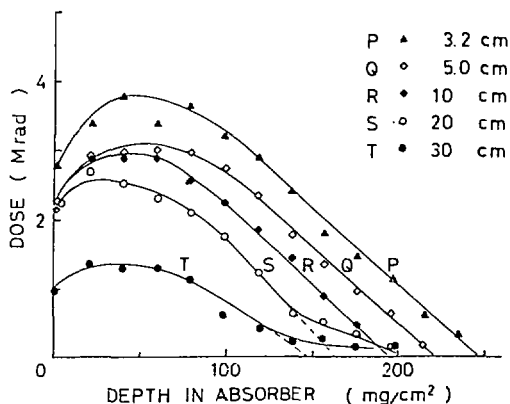
Fig. 4.9   Depth-dose curves in He of 655 Torr on the beam axis
at various positions.

4.3 Surface Dose at Low Pressure of Some Gases

The depth-dose curve in a low-pressure gas, measured in the irradiation cell as described in **3.2**, had sometimes two peaks at the surface and near the third layer of the piled dosimeter. Some results are shown in **Fig. 4.10**. Even if the surface maximum does not appear, the surface dose is high in the pressure region in which the dose increases linearly with increasing pressure as described in **5.2**. This is shown in **Figs. 4.11 – 4.14** as the ratio of the surface dose to the maximum dose near the third layer. The arrow in these figures represents the value of p_{4Mrad} , defined in **5.3**, at which the maximum dose is 4Mrad. The data are rather scattered because the same tube with the same aging was not always used.

Energy spectrum of electrons from a Febetron 706 seems to have the low-energy part

besides the main high-energy part at 480 keV maximum[35]. The high surface dose may be attributed to the former part. The lower-energy electrons run away from the beam channel owing to the defocusing force at lower pressure and the multiple scattering with the medium at higher pressure.
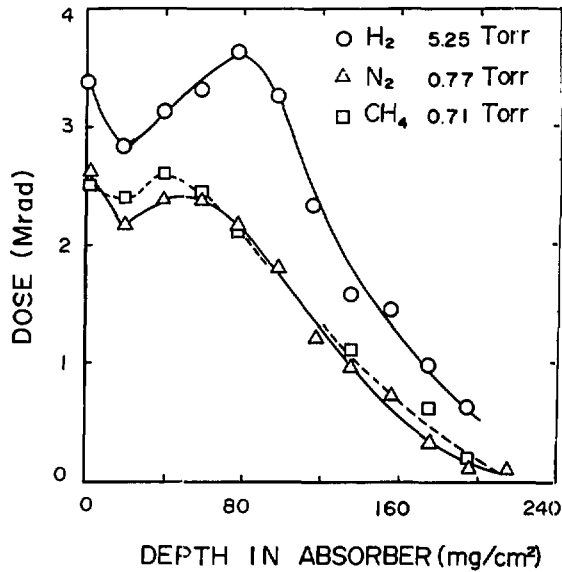
Fig. 4.10   Depth-dose curves in H_2 of 5.25 Torr, N_2 of 0.77 Torr, and CH_4 of 0.71 Torr.
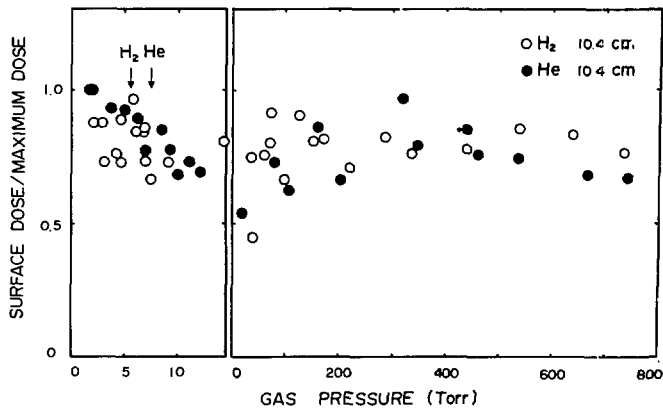
Fig. 4.11   Ratios of the surface dose to the maximum dose in depth-dose curves at 10.4 cm on the beam axis from the cell window as functions of pressure of H_2 (○) and He (●). Arrows indicate $p_{\omega \, r \, od}$
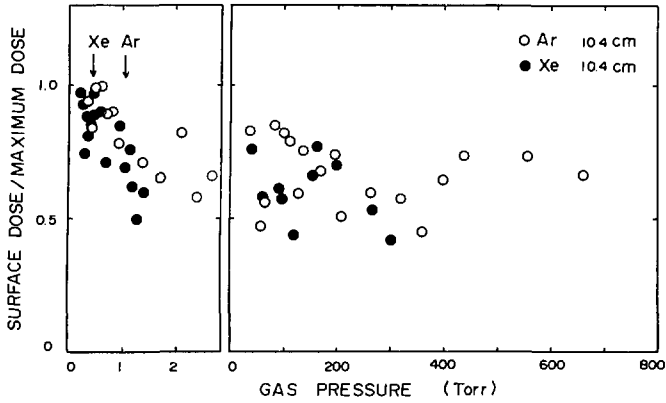
Fig. 4.12   Ratios of the surface dose to the maximum dose in depth-dose curves at 10.4 cm on the beam axis from the cell window as functions of pressure of Ar (○) and Xe (●). Arrows indicate p_{4Mrad}
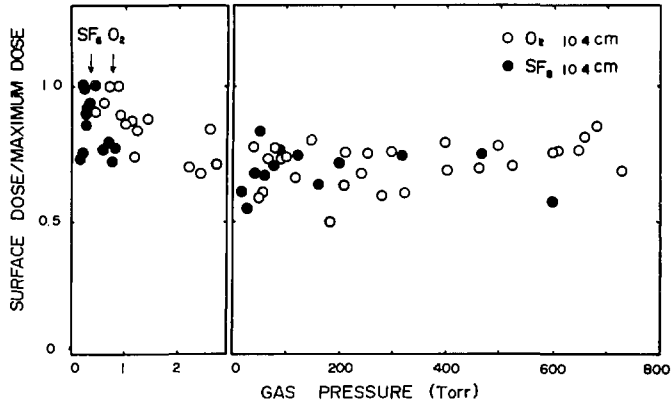
Fig. 4.13   Ratios of the surface dose to the maximum dose in depth-dose curve at 10.4 cm on the beam axis from the cell window as functions of pressure of O_2 (○) and SF_6 (●). Arrows indicate p_{4Mrad}
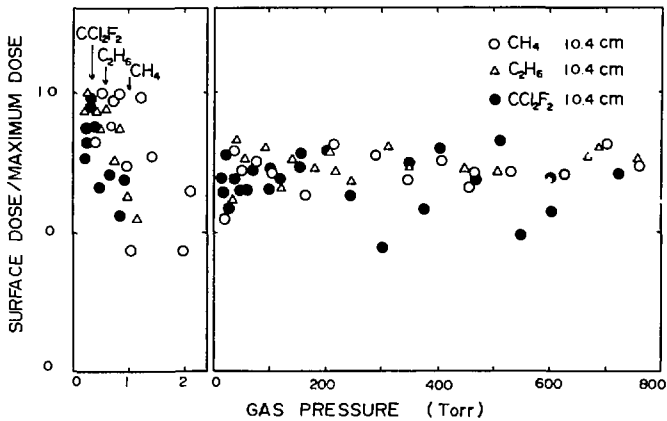
Fig. 4.14   Ratios of the surface dose to the maximum dose in depth-dose curve at 10.4 cm on the beam axis from the cell window as functions of pressure of CH_4 (○), C_2H_6 (△), and CCl_2F_2 (●). Arrows indicate p_{4Mrad}

5. Self-focusing in Various Gases below 5 Torr

5.1 Introduction

A high-intensity relativistic pulsed electron beam is strongly self-focused in a gas generally below 5 Torr but near 10 Torr for He. As seen in **Figs. 3.5 − 3.13**, for all the gases, D_{obs} increases almost linearly with increasing pressure from a certain pressure (0.2 Torr for Ar) due to the self-focusing of the beam. In vacuum, the beam is defocused as shown by Eq. (2.3). At extremely low pressure, the beam is still defocused because of $f_e < 1 - \beta^2$ in Eq. (2.5). Amounts of ions and secondary electrons produced increase linearly with increasing pressure. Secondary electrons run away from the beam channel by F_r of Eq. (2.5) because $\beta^2 \ll 1$ for these electrons as verified by Olson[37]. Therefore, the space charge in the beam channel is neutralized by this escape of secondary electrons to increase f_e with increasing pressure. When f_e becomes larger than $1 - \beta^2$, the beam begins to be self-focused as shown by Eq. (2.6). The self-focusing becomes the maximum for $f_e = 1$ and $f_m = 0$. The value of f_e, however, is not constant over the whole pulse duration. In this chapter, we attempt to simulate the above pressure dependence of D_{obs} as considering the time dependence of f_e. As a result of this analysis, relative total ionization cross sections of gases could be obtained from data on D_{obs} increasing linearly with pressure in the low pressure region.

Miller, Gerardo, and Poukey[17,18] have studied the propagation of pulsed electron beams generated from a Febetron 705 and a Nereus accelerator in some gases. They observed the beam current profile with a Faraday cup equiped at the end of the beam drift tube and then analyzed it by a numerical simulation. The model in this chapter is much simpler than for their analysis because of the present simulation without electronic computer.

5.2 Space-charge Neutralization[9]

The value of f_e is not constant over the whole pulse duration and the whole beam. The beam front is always under a defocusing force because of $f_e = 0$. Consider a fixed position in a beam-drift channel on the beam axis, for example, the position placing a dosimeter. The succeeding part of the beam passing the fixed position is influenced by space-charge neutralization due to accumulation of ions produced by the foregoing part of the beam when secondary electrons escape out completely till t_N; that is, $f_e(t)$ at this position is proportional to $\int_0^t I_b(t)/r_0^2(t)\,dt$, where t is scaled from the time when the beam front passes the fixed position. Then, $r_0(t)$ represents the value of r_0 for the part of the beam delayed by t from the beam front.

When n_0, $n_b(t)$, and $n_i(t)$ represent the number densities of neutral molecules, beam electrons, and positive ions accumulate till t, $n_i(t)$ in the beam channel is given by

$$n_i(t) = \frac{n_0 \sigma_{ion}(E_b)}{\pi e} \int_0^t I_b(t)/r_0^2(t)\,dt \qquad (5.1)$$

where $\sigma_{ion}(E_b)$ is the total ionization cross section for beam electrons with energy E_b. This is obtained by integration of the equation

$$dn_i/dt = n_0 \sigma_{ion}(E_b) n_b(t) v_b \qquad (5.2)$$

because

$$n_b(t) = \frac{I_b(t)}{\pi r_0^2(t) v_b e} \tag{5.3}$$

Terefore, $f_e(t)$ is given as $n_i(t)/n_b(t)$ like

$$f_e(t) = n_0 \sigma_{ion}(E_b) v_b r_0^2(t) / I_b(t) \cdot \int_0^t I_b(t) / r_0^2(t) dt. \tag{5.4}$$

The contribution of secondary ionization to f_e can be neglected at low pressure as explained in **2.2.1**. Consequently, Eq. (2.5) is rewritten as

$$F_r(t) = \frac{2eI_b(t)}{v_b r_0(t)} \left[1 - \beta^2 - \frac{n_0 \sigma_{ion}(E_b) v_b r_0^2(t)}{I_b(t)} \int_0^t \frac{I_b(t)}{r_0^2(t)} dt \right] \tag{5.5}$$

because $I_b = N_e \, e v_b$.

In order to compare the integration in Eq. (2.25) with data on D_{obs}, we must estimate the value of $f_e(t)$. For this purpose, the beam profile must be simplified as a trapezoid as shown in **Fig. 2.1**, which is defined by t_r, t_{flat}, and t_d as shown by dotted lines, for a solid line of the schematic profile; that is, $I_b(t)$ increases linearly till t_r like

$$I_b(t) = I^p \frac{t}{t_r} \tag{5.6}$$

and then $I_b(t)$ is flatted during t_{flat} and decreases linearly for t_d ($t_p = t_r + t_{flat} + t_d$). Hereafter, $r_0(t)$ is assumed to be constant though this assumption may be correct approximately only after t_N.

Generally, t_N is given by the following equations of $f_e(t)$ as $f_e(t_N) = 1$ by using Eq. (5.6).

a)   For $t < t_r$, Eq. (5.4) becomes like

$$f_e(t) = \alpha_c t \tag{5.7}$$

where

$$\alpha_c = \frac{1}{2} n_0 \sigma_{ion}(E_b) c \beta. \tag{5.8}$$

For $\bar{E}_b$ = 480 keV and 20°C,

$$\alpha_c = 4.26 \times 10^{26} p(\text{Torr}) \sigma_{ion} (480 \text{ keV}). \tag{5.9}$$

Then, the value of t_N can be obtained by

$$t_N(ns) = \frac{2.02 \times 10^{18}}{p(\text{Torr}) \sigma_{ion}(E_b) \beta} \qquad \text{at 20°C.} \tag{5.10}$$

For $t_r < t < t_r + t_{flat}$,

$$f_e(t) = \alpha_c(2t - t_r) \tag{5.11}$$

For $t_r + t_{flat} < t < t_p$,

$$f_e(t) = \alpha_c \frac{t_r t_d + 2t_{flat} t_d + 2t' t_d - t'^2}{t_d - t'} \tag{5.12}$$

where $t' = t - t_r - t_{flat}$.

When t_r = 2.2 ns, t_{flat} = 0.5 ns, t_d = 2.5 ns, and σ_{ion}^{Ar} (480 keV) = 9.99 $\times 10^{-19}$ cm^2 [36], values of $f_e(t)$ for various Ar pressures can be estimated from the above equations of $f_e(t)$ as shown in **Fig. 5.1**. After t_N, $f_e(t)$ is assumed to be unity because secondary electrons produced are pushed out or incorporated into the beam channel so as to compensate the change of $I_b(t)$.

In order to test the validity for the value of $f_e(t)$ obtained by such a method, we attempted to simulate the current I_{obs} observed by Miller et al. [17] by using the value of $f_e(t)$ calculated similarly for their beam [9]. The result indicates that I_{obs} from the accelerator with small ν/γ is in good agreement with the calculated one when the beam is not strongly defocused. Therefore, values of $f_e(t)$ in **Fig. 5.1** are applicable for the self-focused beam from a Febetron 706 with ν/γ = 0.28.

When I_{back} = 0 for $t < t_B$, Eq. (2.25) is rewritten as

$$D_{obs} \propto \int \frac{I_b^2(t)|1 - f_e(t) - \beta^2|}{\epsilon_b^2} dt \tag{5.13}$$

because $I_{net} = I_b$. The value of $I_b^2(t)|1 - f_e(t) - \beta^2|$ for $f_e(t) > 1 - \beta^2$, obtained by using $I_b(t)$ as shown by dotted lines in **Fig. 2.1** and $f_e(t)$ in **Fig. 5.1**, are plotted against t for some Ar pressures (Torr) in **Fig. 5.2**. The curve approaches the envelope with increasing pressure. When ϵ_b is assumed to be constant, D_{obs} must be proportional to the integration of the curve in **Fig. 5.2**. In **Fig. 5.3**, the result of such an integration is shown in an arbitrary units as curve A as a function of Ar pressure. This curve should approach asymptotically to the value for the envelope in **Fig. 5.2** with increasing pressure, in accordance with the result of Miller et al[17]. Since the dose at 0.1 Torr is nearly equal to the background dose in **Fig. 3.6**, curve B in **Fig. 5.3** represents the value subtracted by the value at 0.1 Torr. These curves indicate that D_{obs} increases almost linearly up to 0.7 Torr with increasing pressure. When ϵ_b in Eq. (5.13)
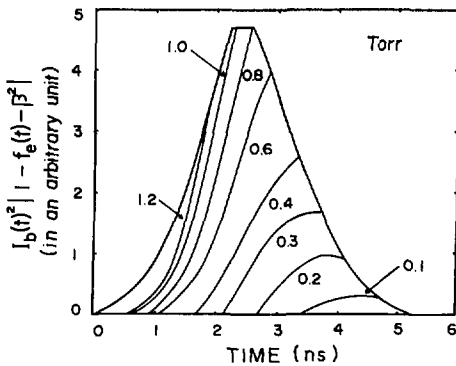
Fig. 5.1   Curves of claculated $f_e(t)$ for various
          Ar pressure (Torr).
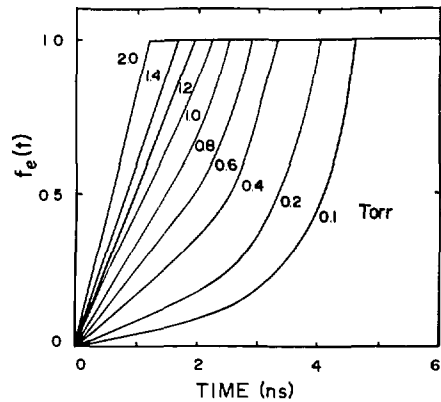
Fig. 5.2   Curves of $I_b(t)^2|1 - f_e(t) - \beta^2|$ calculated
          from $f_e(t)$ in Fig. 5.1.
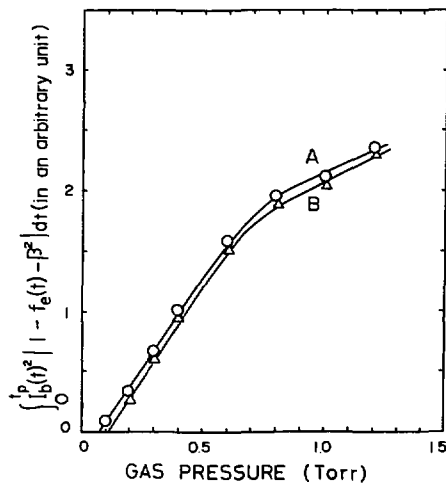
Fig. 5.3   The curve of $\int_0^{t_p} I_b(t)^2|1 - f_e(t) - \beta^2| dt$ calculated
          from data in Fig. 5.2. See text for A and B. The t_p
          is the pulse duration.

must be smaller for the self-focused beam than for the defocused one, the actual curve of D_{obs} rises more steeply than the curve in **Fig. 5.3**. In **Fig. 3.6**, the linearity of D_{obs} is seen up to near 1 Torr.

According to the computer simulation as will be shown in 7., the t_B model of I_{net} in **2.2.1** is correct to some extent up to the pressure at which D_{obs} becomes the minimum, for example, up to 5 Torr for Ar. From Eq. (5.13), D_{obs} should be the maximum for $t_B = t_r = 2.2$ ns because $I_{net}(t_B) = I^p$ for this case. In fact, the pressure for $t_B = 2.2$ ns is nearly equal to the pressure giving the maximum D_{obs} as considering the experimental accuracy as shown in Table II of ref. 8.

5.3 Total Ionization Cross Section

The value of D_{obs} increases almost linearly with increasing pressure in a low-pressure gas. In this region, from Eq. (5.13), D_{obs} is in a function of f_e given by Eq. (5.4) in which the values of v_b and $I_b(t)$ are given by the machine not by the gas. At low pressure at which the beam is not scattered by the medium, ε_b is also assumed to vary with time irrelevant of the kind of gas. Therefore, in Eq. (5.4), when these parameters are considered to be constant for the present experimentation, $f_e(t)$ is determined only by $n_0 \sigma_{ion}(E_b)$ or $p \sigma_{ion}(E_b)$. Although $r_0(t)$ and $F_r(t)$ are dependent on each other, for a fixed value of $p \sigma_{ion}(E_b)$, $r_0(t)$ should vary on the same way with the lapse of time irrelevant of the kind of gas so that D_{obs} should be the same for any gas. Consequently, we can obtain the total ionization cross section of the i' the gas for the primary beam, $\sigma_{ion}^{(i)}(E_b)$ from the equation

$$p_D^{(i)} \sigma_{ion}^{(i)}(E_b) = p_D^{(i)} \sigma_{ion}^{(i)}(E_b) \tag{5.14}$$

or

$$\sigma_{ion}^{(i)}(E_b) / \sigma_{ion}^{(s)}(E_b) = p_D^{(s)} / p_D^{(i)} \tag{5.15}$$

where p_D represents the pressure at which the value of D_{obs} is D and the index s is refered to the standard gas. Miller, Gerardo, and Poukey[17] pointed out the similar relationship between σ_{ion} and the pressure at which the current collected at about 1 m by a Faraday cup is 60% of the initial. Their latter pressure corresponds to the above p_D.

In **Figs. 3.5 — 3.13**, D_{obs} appears to increase linearly up to $3 - 4$ Mrad. Therefore, the value of $p^{(i)}$ for 4 Mrad, p_{4Mrad}, was determined by the least square method from data on D_{obs} in the linearly increasing region, because the value can be determined more precisely for the higher dose. Since the value was 5.35 Torr for H_2, the relative total ionization cross section to H_2 can be determined from $p_{4Mrad}^{(i)}$ by Eq. (5.15) as listed in **Table 5.1**. Rieke and Prepejchal[36] have determined experimentally the values of M_{ion}^2 and C_{ion} for various gases in the equation

$$\sigma_{ion} = 4\pi \left(\frac{\hbar}{m_e c} \right)^2 (M_{ion}^2 \, x_1 + C_{ion} x_2) \tag{5.16}$$

where $x_1 = \beta^2 \ln[\beta^2/(1-\beta^2)] - 1$, $x_2 = \beta^{-2}$, and $\hbar = h/2\pi$ (h :Planck's constant). The values for $E_b = 480$ keV are listed also in **Table 5.1**. The relative values to H_2 from Eq. (5.15) are generally in good agreement with those from Eq. (5.16) except for gases with larger σ_{ion}. Although the beam from a Febetron 706 has the energy spectrum, the relative value of σ_{ion} to H_2 from Eq. (5.16) is almost constant proportionally to M_{ion}^2 over the wide energy range. The disagreement for gases with larger σ_{ion} may be mainly attributed to the experimental difficulty to determine p_D precisely because p_D is less than 0.4 Torr and D_{obs} increases steeply with increasing pressure.

Table 5.1 Total ionization cross sections

Gas	Relative values of σ_{ion} from		Absolute value of σ_{ion} (480 keV) (10^{-19}cm^2) from ref. 36
	$p_{\text{эМ rad}}$	ref. 36	
H_2	1.00	1.00	2.13
D_2	1.02	−	−
He	0.72	0.93	1.98
Ne	2.00	2.26	4.81
Ar	5.00	4.69	9.99
Kr	7.17	6.43	13.8
Xe	11.2	9.06	19.3
N_2	4.16	4.30	9.15
O_2	4.28	4.79	10.2
CO_2	6.28	7.00	14.9
N_2O	6.65	−	−
SF_6	14.9	−	−
CH_4	5.30	5.16	11.0
CH_3F	7.29	−	−
$CHClF_2$	12.2	−	−
CCl_2F_2	15.8	−	−
C_2H_2	6.60	6.62	14.1
C_2H_4	8.33	8.45	18.0
C_2H_6	9.01	8.50	18.1
C_3H_8	13.1	14.0	29.9
n-C_4H_{10}	16.2	18.9	40.2
cis-2-C_4H_8	14.9	−	−
n-C_5H_{12}	18.4	22.8	48.5
neo-C_5H_{12}	19.1	22.6	48.1

6. Computation of Net Current in Gases above 5 Torr

6.1 Introduction

As seen in **Figs. 3.5 − 3.13**, after passing the maximum at low pressure. D_{obs} decreases abruptly with slightly increasing pressure and, after passing the minimum, increases again gradually with further increasing pressure. This phenomenon is attributed to gas breakdown due to electron avalanching which is suppressed with increasing pressure. Such a pressure dependence was analyzed quantitatively in terms of breakdown time t_B[8] which is defined in **2.2.1**. However, since the t_B model of $I_{net}(t)$ was simplified enough to estimate the value of t_B without an electronic computer, the whole data on D_{obs} could not be explained sufficiently by t_B of this model. Afterwards, the value of $I_{net}(t)$ is calculated self-consistently on the basis of the scheme as described in this chapter[10,11]. Since $I_{net}(t)$ is related approximately to D_{obs} by Eq. (2.26), our data on D_{obs} can be analyzed physicochemically by $I_{net}(t)$ calculated by using molecular data for gases as will be described in **7. − 10.**.

6.2 Computational Model

After space-charge neutralization (Eq. (5.10)), secondary electrons remain in the beam-drift channel to be accelerated by an induced longitudinal electric field E_z. For the uniform beam of a radius r_0 (cm), E_{z0} (V/cm) on the beam axis is given by Eq. (2.12) like

$$E_{z0}(t) = -2 \times 10^{-9} \left(\frac{1}{2} + \ln\frac{R}{r_0}\right)\frac{d I_{net}(t)}{d t}$$

$$= c_1 \frac{d I_{net}(t)}{d t} \, . \tag{6.1}$$

In the present computation, I_{net} (A) is assumed like

$$I_{net}(t) = I_b(t) + I_{back}(t)$$

$$= I_b(t) + \pi r_0^2 E_z(t)\sigma_e(t) \tag{6.2}$$

where σ_e (mho/cm) is the plasma conductivity. In Eq. (6.2), $I_{back} < 0$ for $dI_{net}(t)/dt > 0$ because $E_z < 0$ in Eq. (6.1). Generally speaking, E_z at r from the beam axis is given for $r_0 > r > 0$ by

$$E_z = -2 \times 10^{-9} \left[\frac{1}{r_0}\left(1 - \frac{r^2}{r_0^2}\right) + \ln\frac{R}{r_0}\right]\frac{d I_{net}(t)}{d t} \, . \tag{6.3}$$

Since the mean value of E_z for $r_0 > r > 0$ is given from Eq. (6.3) as

$$\bar{E}_z = 0.93 E_{z0} \tag{6.4}$$

for $r_0 = 0.6$ cm and $R/r_0 = 10$, this mean value was used for the present computation. In Eq. (6.2), I_{back} is assumed to equal $\pi r_0^2 E_z \sigma_e$*b.

---

*b) Exactly speaking, I_{back} is given by[38]

$$I_{back} \cdot \frac{E_z \sigma_e}{1 + (\omega_c/\nu_{en})^2}$$

where ω_c is the electron cyclotron frequency given by

$$\omega_c = \frac{eB_\theta}{cm_e}$$

and ν_{en} the momentum transfer collision frequency given by Eq. (6.7) Therefore, Eq. (6.2) is correct only for $\omega_c/\nu_{en} \ll 1$. The value of B_θ is zero at the center of the beam and increases linearly with r up to

The plasma conductivity σ_e of a partially ionized gas in a dc electric field is given by[38]

$$\frac{1}{\sigma_e} = \frac{1}{\sigma_{en}} + \frac{1}{\sigma_{ei}} .$$ (6.5)

The conductivity due to electron-neutral collisions σ_{en} is given by

$$\sigma_{en} = \frac{e^2 n_e}{m_e \nu_{en}}$$ (6.6)

where n_e is the number density of secondary electrons and ν_{en} is the momentum transfer collision frequency of an electron with neutral particles given by

$$\nu_{en} = n_0 \langle Q_m(\varepsilon) v \rangle$$ (6.7)

($\langle\ \rangle$ represents the mean value). In Eq. (6.7), $Q_m(\varepsilon)$ is the momentum transfer cross section from an electron to neutral particles which depends on electron energy ε and v is the random electron velocity which is related to ε like

$$v = \sqrt{2\,\varepsilon/m_e} .$$ (6.8)

Therefore, when it is assumed that

$$\langle Q_m(\varepsilon) v \rangle = \sqrt{2/m_e}\, Q_m(\bar\varepsilon)\bar\varepsilon^{0.5}$$ (6.9)

($\bar\varepsilon$: the mean energy of secondary electrons), σ_{en} is given by

$$\sigma_{en} = \frac{e^2 n_e(t)}{n_0(2m_e)^{\frac12} Q_m(\bar\varepsilon)\bar\varepsilon^{\frac12}}$$

$$\simeq 1.43 \times 10^{-28} \frac{n_e(t)}{p(\text{Torr}) Q_m(\bar\varepsilon)\bar\varepsilon^{0.5}} \qquad \text{(at 20°C)}.$$ (6.10)

On the other hand, the conductivity due to electron-ion collisions σ_{ei} is given by[39]

$$\sigma_{ei} = 97.1 \cdot \frac{(2\bar\varepsilon/3)^{1.5}}{(23.5 + 1.5\ln(2\bar\varepsilon/3) - 0.5\ln n_e)} .$$ (6.11)

When $\sigma_{ei} \gg \sigma_{en}$, it can be assumed that $\sigma_e \approx \sigma_{en}$. Since this condition was realized as the computational result in the pressure region interested for the present analysis, data on D_{obs} can be analyzed only in terms of σ_{en} given by Eq. (6.10) instead of σ_e in the following chapters.

The value of $\bar\varepsilon$ is estimated from D_L/μ (the ratio of lateral electron diffusion coefficient to electron mobility) by

$$\bar\varepsilon = \frac{3}{2}\varepsilon_k = \frac{3}{2}\frac{e\,D_L}{\mu}$$ (6.12)

on assumption of the Maxwellian, where ε_k is the characteristic energy. The energy distribution shifts to the Druyvesteynian from the Maxwellian at low E/p at which the energy is lost only by elastic collisions. At high E/p at which inelastic collisions are predominant, the distribution becomes again the Maxwellian approximately[40]. In monatomic gases with excitation levels much closer to ionization potential, the energy may be lost only by elastic collisions up to the lowest excitation level. However, according to Dote and Shimada[41], the value of α_T/p for He calculated by the Boltzmann equation analysis on the assumption of the Maxwellian is much closer to the experimental data between 100 and 1000 Vcm^{-1}Torr^{-1}, where α_T is the first Townsend ionization coefficient.

The value of $n_e(t)$ in Eq. (6.10) is obtained from the following equations. The production of secondary electrons after t_N can be expressed from the Townsend discharge theory as

---

r_0 for a radially uniform beam. For such a ideal beam, $\omega_c = 8 \times 10^{10}\, r$ radian/s at $r < r_0$ for $I_{net} = 8000$ A and $r_0 = 0.6$ cm. Therefore, for the present study, the maximum value of ω_c is 4.8×10^{10} radian/s at the surface of the self-focused beam and zero on the beam axis. For the defocused beam, ω_c is reduced extremely because of decreasing I_{net} and increasing r_0. On the other hand, ν_{en} given by Eq. (6.7) must be between 2×10^9 and $2 \times 10^{10}\, p$ (Torr)/s because $Q_m(\bar\varepsilon)\varepsilon^{0.5}$ is generally between 10^{-15} and 10^{-14} cm^2 ev$^{0.5}$. Therefore, the assumption for Eq. (6.2) ($\omega_c/\nu_{en} \lesssim 1$) may be realized except for the strongly self-focused beam at low pressure.

$$\frac{dn_e}{dt} = \frac{n_0 \, \sigma_{ion}(E_b) I_b(t)}{\pi \, r_0^2 \, e} + \frac{n_e(t)}{t_i(t)} \quad . \tag{6.13}$$

The first term represents the direct ionization of the primary beam and the second term the electron avalanching by E_z. In Eq. (6.13), the particle transport current out of the beam channel due to the electric field and diffusion is neglected because of the ns pulse duration.

The mean ionization time t_i for the second term can be estimated by[37]

$$t_i = t_f/18.4 \tag{6.14}$$

from the breakdown formative time t_f determined experimentally by Felsenthal and Proud[42], who have demonstrated that their data on t_f can be expressed by

$$pt_i = \frac{pt_f}{18.4} = \frac{1}{w(\alpha_T/p - \eta_T/p)} \tag{6.15}$$

where w is the electron drift velocity, α_T the first Townsend ionization coefficient, and η_T the electron attachment coefficient.

For the present computation, Eq. (6.13) is revised as

$$\frac{dn_e}{dt} = \frac{n_0 \, \sigma_{ion}(E_b) I_b(t)}{\pi \, r_0^2 \, e} + \frac{n_e(t)}{t_i(t)} - \alpha_r n_e n_i \quad \alpha_{rd} n_e n_d, \tag{6.16}$$
$$\text{(term 1)} \qquad\quad \text{(term 2)} \quad \text{(term 3)} \quad \text{(term 4)}$$

$$\frac{dn_i}{dt} = \frac{n_0 \, \sigma_{ion}(E_b) I_b(t)}{\pi \, r_0^2 \, e} + \frac{n_e(t)}{t_i(t)} - \alpha_r n_e n_i - k_d n_i n_0^2 \tag{6.17}$$

and

$$\frac{dn_d}{dt} = k_d n_i n_0^2 - \alpha_{rd} n_e n_d \tag{6.18}$$

in considering the following reactions

$$A^+ + e^- \xrightarrow{\alpha_r} A^* \tag{6.19}$$

$$A^+ + 2A \xrightarrow{k_d} A_2^+ + A \tag{6.20}$$

$$A_2^+ + e^- \xrightarrow{\alpha_{rd}} 2A \tag{6.21}$$

where α_r and α_{rd} are the recombination coefficients for reactions (6.19) and (6.21) respectively. The k_d is the rate constant of reaction (6.20) which is reviewed by Good[43]. The number densities of A^+ and A_2^+ are represented by n_i and n_d.

6.3 Computational Procedure

The computational program for the estimation of I_{net} according to the above scheme has been published elsewhere[44]. The beam radius r_0 was assumed to be constantly 0.6 cm over the whole pulse duration. For $r_0 = 1.2$ cm, the value of I_{net} increased by about 20% at 10 and 50 Torr of Ar.

Since $E_z(t)$ and $I_{net}(t)$ depend on each other according to Eqs. (6.1) and (6.2), the problem was solved self-consistently as referring the paper of Swain[14]. From Eqs. (6.1) and (6.2), we can obtain the equation as

$$E_z(t + \Delta t) = c_1 \frac{I_{net}(t + \Delta t) - I_{net}(t)}{\Delta t} \tag{6.22}$$

and

$$I_{net}(t + \Delta t) = I_b(t + \Delta t) + \pi r_0^2 E_z(t + \Delta t) \sigma_e(t + \Delta t) \tag{6.23}$$

where $\Delta t = 0.005$ ns for the present computation. When Eq. (6.23) is substituted to Eq. (6.22),

$$E_z(t + \Delta t) = c_1 \frac{I_b(t + \Delta t) - I_{net}(t)}{t - c_1 r_0^2 \sigma_e(t + \Delta t)} \tag{6.24}$$

According to the present scheme, it is assumed for $t < t_N$ that $n_e(t) = 0$, $\sigma_e = 0$, and $I_{back} = 0$. At t_N, we assume tentatively $\sigma_1 \doteq \sigma_e(t_N) = 0.0001$. Then, we can obtain the tentative value of $E_z(t_N + \Delta t) = E_{zi}$ from Eq. (6.24). When E_{zi} acts between t_N and $t_N + \Delta t$, values of n_e, n_i, and n_d are obtained from Eqs. (6.16), (6.17), and (6.18) by means of the Runge-Kutta method[45]. Next, we obtain $\sigma_{1c} \doteq \sigma_e(t_N + \Delta t)$ from Eqs. (6.5), (6.10), and (6.11) by using the above values of n_e, n_i, and n_d and also the values of and $Q_m(\epsilon)\epsilon^{0.5}$ for E_{zi}/p. When σ_{1c} meets the condition

$$|\sigma_1 - \sigma_{1c}| / \sigma_{1c} < 0.01, \tag{6.25}$$

the value of σ_{1c} is accepted at $\sigma_e(t_N + \Delta t)$. If not so, we assume tentatively σ_2 like

$$\sigma_2 = \sigma_1^\alpha \sigma_{1c}^{(1-\alpha)} \tag{6.26}$$

($\alpha = 0.8$ for the present computation) to obtain σ_{2c} according to the above procedure. When $|\sigma_2 - \sigma_{2c}|/\sigma_{2c}$ is not less than 0.01, we assume again tentatively $\sigma_3 \doteq \sigma_2^\alpha \sigma_{2c}^{(1-\alpha)}$ to obtain σ_{3c}. This procedure is repeated successively till $|\sigma_i - \sigma_{ic}|/\sigma_{ic}$ becomes less than 0.01. When σ_{ic} meets this condition, σ_{ic} is accepted as $\sigma_e(t_N + \Delta t)$. Then, we proceed to the next step to determine $\sigma_e(t_N + 2\Delta t)$; for this case, $\sigma_1 \doteq \sigma_e(t_N + \Delta t)$ to obtain σ_{1c}. Such a procedure is repeated successively to calculate $\sigma(t_N + n\Delta t)$ till the end of the pulse duration.

As shown in **Fig. 2.1**, I_b is assumed to be flatted at t_{flat} so that the calculated E_z varies abruptly in this region. However, the value of ϵ might not be changed according to this abrupt change of E_z/p. Data on the related parameters are cited as functions of ϵ of E_z/p. The present computation was carried out automatically without any correction of this problem. The phenomenon interested in the present study must be determined mainly by the rising part of the pulsed beam. Therefore, no correction is presumed not to affect the result seriously for our subject.

7.   Ionization of Monatomic Gases by Pulsed Beam

7.1   Computational Result of I_{net} for He and Ar[10]

7.1.1   He

The computation of $I_{net}(t)$ for He was carried out by using σ_{ion} (480 keV) = 1.98 × 10^{-19} cm² [36], t_i [42], D_L/μ [46], and Q_m [47]. The results are shown in the following figures. Curves of $I_{net}(t)$ are shown in **Fig. 7.1**. The curve indicates that, up to 30 Torr, $I_{net}(t)$ is approximately constant after a certain time so as to be able to determine the definite value of t_B as
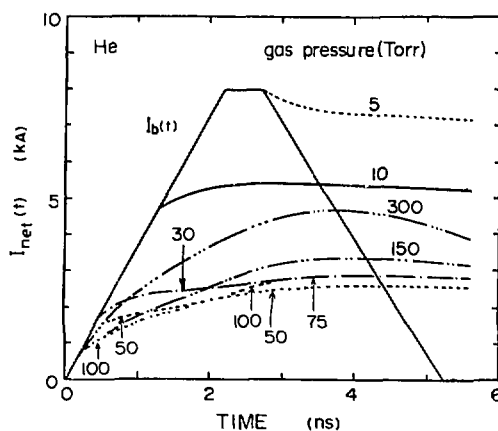
Fig. 7.1   Calculated curves of $I_{net}(t)$ for various pressure of He.
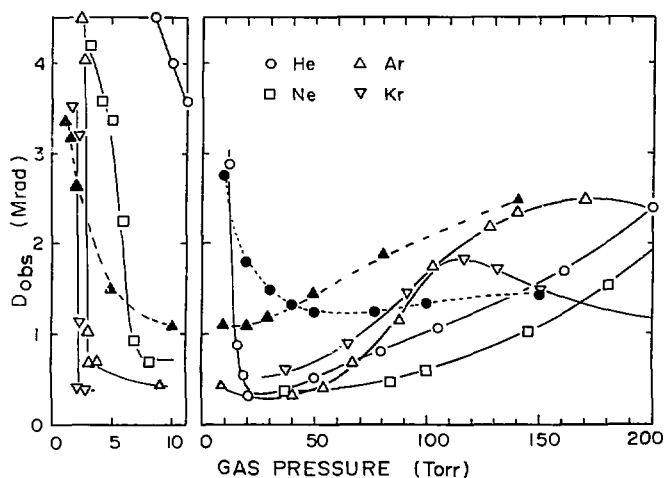
Fig. 7.2   Data on $D_{obs}(p)$ for monatomic gases shown by open marks. Values of $\int_0^{t_B} I_b(t) I_{net}(t) dt$ calculated from $I_{net}(t)$ in Fig. 7.1 are also plotted in an arbitrary unit for He (●) and Ar (▲).
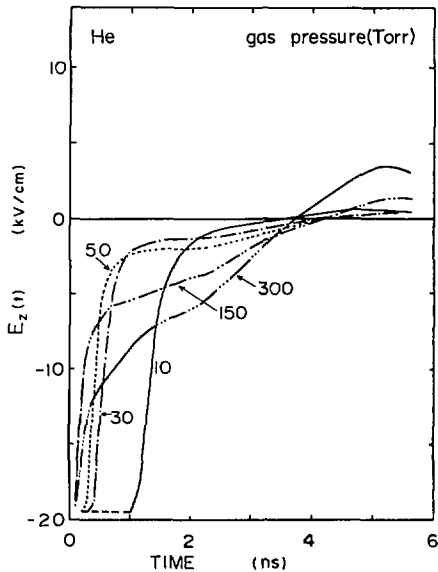
Fig. 7.3 Calculated curves of $E_z(t)$ for various pressures of He.
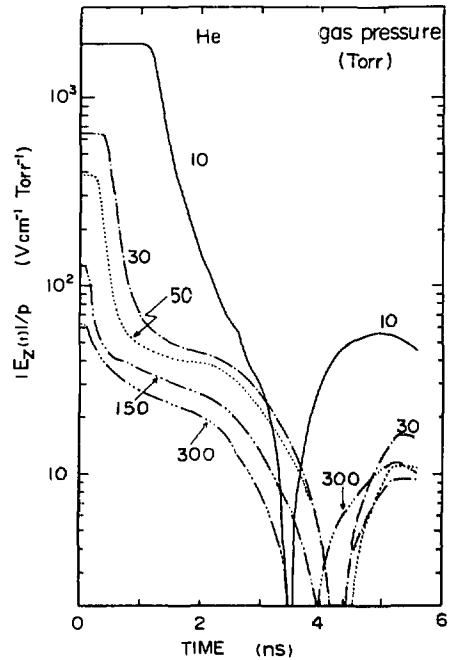
Fig. 7.4 Calculated curves of E_z/p obtained from E_z in Fig. 7.3 for various pressures of He.
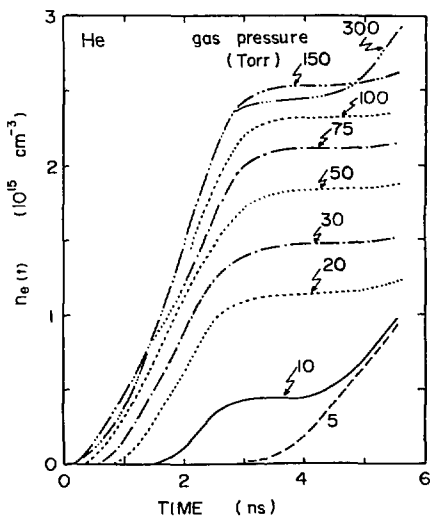
Fig. 7.5 Calculated curves of $n_e(t)$ for various pressures of He.
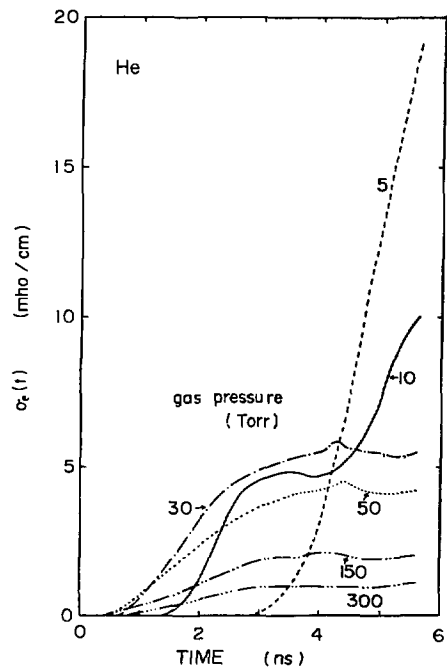
Fig. 7.6 Calculated curves of $\sigma_e(t)$ for various pressures of He.

described in **2.2.1**[8] and that, at higher pressure, $I_{net}(t)$ increases gradually with the lapse of time. The upper limit of the pressure for the t_B model of I_{net} is nearly equal to the pressure giving the minimum D_{obs} as seen in **Fig. 7.2** in which data on D_{obs} for all the monatomic gases[3] are summarized. The corresponding E_z and E_z/p curves are shown in **Figs. 7.3** and **7.4** respectively. Curves of $n_e(t)$ are shown in **Fig. 7.5**. The value of $n_e(t)$ becomes flat after 3 ns. This plateau value increases with increasing pressure up to 150 Torr, at which D_{obs} in **Fig. 7.2** equals about 1 Mrad. The corresponding curves of σ_e are shown in **Fig. 7.6**. The value becomes the maximum at near 30 Torr at which D_{obs} becomes the minimum as seen in **Fig. 7.2**. Values of $\bar{\epsilon}$ for E_z/p in **Fig. 7.4** estimated by Eq. (6.12) are higher than 12 eV till at least 2 ns, irrelevant of pressure.

7.1.2 Ar

The computation for Ar was carried out by using σ_{ion} (480 keV) = 9.99 × 10^{-19} cm² [36], t_i[42], D_L/μ[46], and Q_m[47]. The results are shown in **Fig. 7.6** for $I_{net}(t)$, in **Fig. 7.8** for $E_z(t)$ in **Fig. 7.9** for E_z/p, in **Fig. 9.10** for $n_e(t)$ and **Fig. 7.11** for $\sigma_e(t)$. The curve of $I_{net}(t)$ up to 10 Torr varies approximately according to the t_B model of I_{net}. The value of σ_e is larger than for He and becomes the maximum at 5 Torr. The plateau value of $n_e(t)$ increases up to 80 Torr, at which D_{obs} in **Fig. 7.2** equals about 1 Mrad and decreases slightly with further increasing pressure. Values of $\bar{\epsilon}$ for E_z/p in **Fig. 7.9** are between 9 and 11 eV in the whole pressure region.
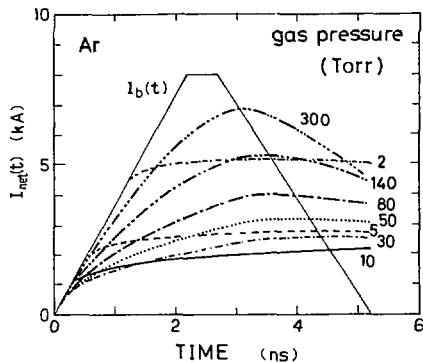
Fig. 7.7   Calculated curves of $I_{net}(t)$ for various pressures of Ar.
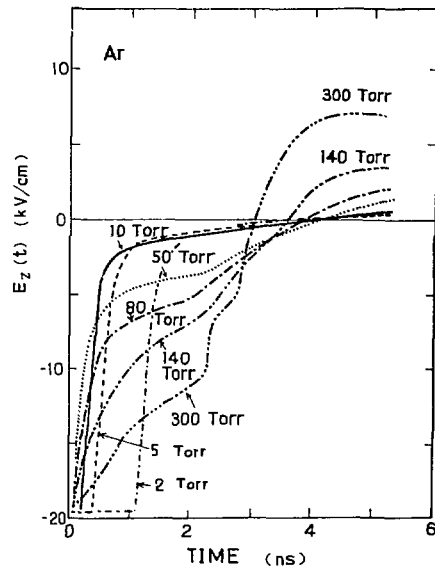
Fig. 7.8   Calculated curves of $E_z(t)$ for various pressures of Ar.
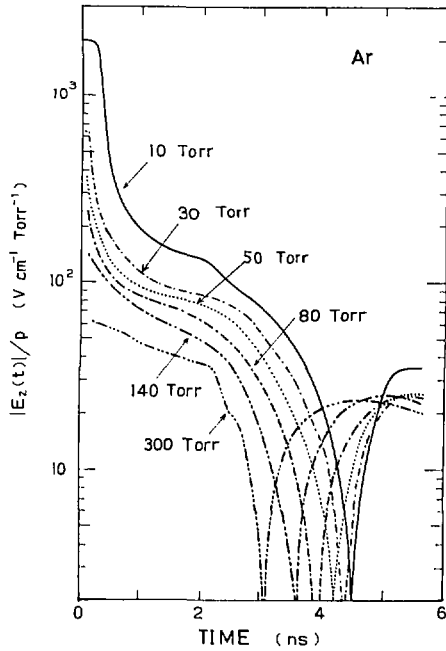
Fig. 7.9   Calculated curves of E_z/p obtained from E_z in Fig. 7.8 for various pressures of Ar.
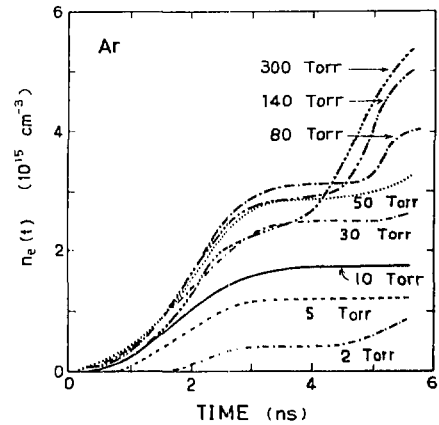
Fig. 7.10   Calculated curves of $n_e(t)$ for various pressures of Ar.
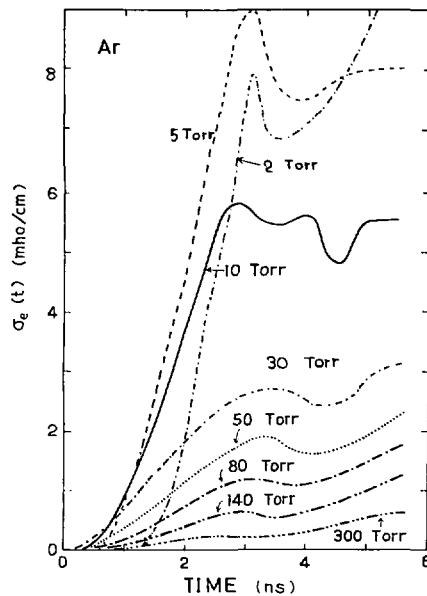
Fig. 7.11   Calculated curves of $\sigma_e(t)$ for various pressures of Ar.

7.1.3 Conclusion

The value of I_{net} varies with the lapse of time approximately according to the t_B model of I_{net} up to the pressure at which D_{obs} becomes the minimum. At higher pressure, $I_{net}(t)$ increases gradually with time even after t_B. The gradient of increasing $I_{net}(t)$ increases with increasing pressure. The value of $n_e(t)$ becomes flat at about 3 ns. This plateau value increases up to $2.5 - 3.0 \times 10^{15}$ cm^{-3} for He and Ar with increasing pressure as far as D_{obs} becomes about 1 Mrad. The curve of $n_e(t)$ does not vary appreciably with further increasing pressure. The value of E_z/p decreases with the lapse of time and also with increasing pressure. Furthermore, the value of E_z/p lies between 10 and 100 Vcm^{-1}Torr^{-1} for the major part of the pulse duration in the pressure region in which D_{obs} increases gradually with increasing pressure. The computational results indicate that the contributions of σ_{ei} to σ_e and of electron-ion recombination processes can be neglected for monatomic gases. For this calculation, values of α_r, k_d, and α_{rd} are cited from refs. 48, 43, and 49 respectively.

7.2 Discussion

7.2.1 Comparison of the calculated $I_{net}(t)$ with data on D_{obs}

Data on D_{obs} in monatomic gases[3] are plotted as functions of pressure in **Fig. 7.2**. Since the value of $\int_0^{t_b} I_b(t) I_{net}(t) dt$ may be proportional to D_{obs} from Eq. (2.26), values of the integral calculated from the values of $I_{net}(t)$ in **Figs. 7.1** and **7.7** are also plotted in an arbitrary unit by solid marks (● for He and ▲ for Ar) in **Fig. 7.2**. The value for Ar corresponds well to the value of D_{obs} (△), while that for He is the minimum at 50 Torr despite of the minimum D_{obs} (○) at about 20 Torr. This discrepancy for He may be due to ignorance of ionization by secondary electrons escaping radially as pointed out as the enhancement factor by McArthur and Poukey[16]. This factor might not be ignored for the case that such an escaping occurs up to higher pressure as for He.

As another discrepancy, the minimum value of the integral is large for both the gases in comparison with their minimum D_{obs}. This discrepancy is mainly attributed to variation of ϵ_b which should be larger for a defocused beam than for a self-focused beam. Furthermore, when the envelope of the defocused beam is conic at the observing position (10.4 cm from the cell window), the factor A in Eq. (2.20) should be smaller than that of Eq. (2.20) for the paraxial beam. When the curve of the integral is corrected for A and ϵ_b, the value at the minimum or for the most defocused beam becomes relatively much small against the larger value of the integral. Then, the curve of the integral against p can be fitted with the curve of D_{obs} by using the corrected value of A and ϵ_b. The present computation is fitted in itself for the self-focused beam because of the assumption that $r_0 = 0.6$ cm.

It is concluded from this comparison that the present computational results can be used for the analysis of data on D_{obs}. Decreasing of D_{obs} above 150 Torr of Ar is due to multiple scattering of the primary beam (Chap. 11).

7.2.2 Relationship between D_{obs} and t_i

In the pressure region in which D_{obs} increases gradually with increasing pressure after passing the minimum, the calculated $I_{net}(t)$ increases gradually with the lapse of time even after electron avalanching occurs. This increasing gradient increases with increasing pressure so as to induce the larger E_z with increasing pressure. This means that, at the same pressure, the larger D_{obs} is given by the gas giving the larger E_z/p. On the other hand, the larger I_{net} means the smaller negative I_{back} which is determined by $E_z \sigma_e$. Since it can be assumed that

$\sigma_e \approx \sigma_{en}$, from Eq. (6.10), the value of $E_z \sigma_e$ is proportional to the product of $n_e/Q_m \bar{\varepsilon}^{0.5}$ and E_z/p. Therefore, the value of $n_e/Q_m \bar{\varepsilon}^{0.5}$ must be much smaller for the larger D_{obs} because of the larger E_z/p. Most of secondary electrons are produced by electron avalanching (term 2 in Eq. (6.16)) which is given by $n_e(t)/t_i$. Consequently, when the variation of $Q_m \bar{\varepsilon}^{0.5}$ is neglected among gases, the larger D_{obs} is given by the gas giving the larger t_i or pt_i at the same pressure. This relationship between D_{obs} and t_i is the most important conclusion from the present analysis. Hereafter, data on D_{obs} will be analyzed on the basis of this conclusion.

When $\eta_T = 0$ in Eq. (6.15) as in monatomic gases, t_i is given by

$$1/(pt_i) = w\alpha_T/p . \qquad (7.1)$$

Values of w and α_T/p for various gases are known as functions of E/p[50,51]. Since swarm parameters are measured under steady-state conditions, they may not be applied directly for the abrupt change of E/p as pointed out at the end of **6.**. However, the present computational result shows that these data can be used as the measure of them for the present study as will be shown in the following chapters.

Data on w and α_T/p for monatomic gases[50,51] are shown in **Figs. 7.12** and **7.13**. As comparing these data among gases for E/p below 100 Vcm^{-1}Torr^{-1} which is given in the pressure region in interest in **Figs. 7.4** and **7.9**, the value of $w\alpha_T/p$ is in the order

$$Ne > He > Ar \approx Kr > Xe . \qquad (7.2)$$

Therefore, as compared at the same pressure at which $E/p < 100$ Vcm^{-1}Torr^{-1}, the order of t_i or D_{obs} should be inverse to the order (7.2). This conclusion is consistent with the order of D_{obs} at pressures above 70 Torr in **Fig. 7.2**. Data on D_{obs} for Xe are not sufficient due to multiple scattering of the beam by Xe. Values of $Q_m \bar{\varepsilon}^{0.5}$ for monatomic gases[47,52] are given as functions of ε in **Fig. 7.14**. These curves indicate that the value around 10 eV of ε is smaller for He and Ne than for Ar, Kr, and Xe. Therefore, as considering the variation of $Q_m \bar{\varepsilon}^{0.5}$ among monatomic gases, value of D_{obs} for He and Ne must be more separated from the values for Ar and Kr than as expected from the value of $w\alpha_T/p$. The value of D_{obs} reversed between Ar and He at 50 Torr. This is due to the inversion of α_T/p at 80 Vcm^{-1}Torr^{-1} in **Fig. 7.13**.

On the other hand, Eq. (7.1) is rewritten as
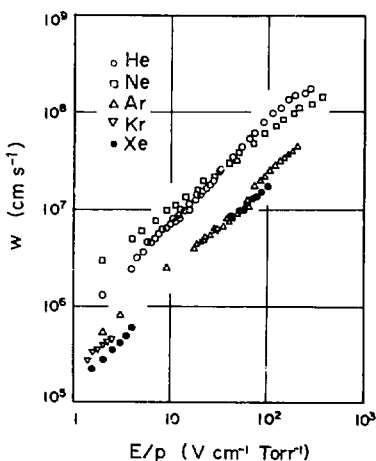
Fig. 7.12   Curves of w as functions of E/p for monatomic gases cited from references in text.
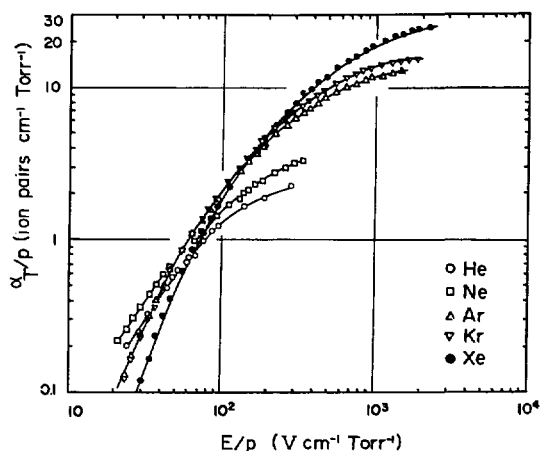
Fig. 7.13   Curves of α_T/p as functions of E/p for monatomic gases.
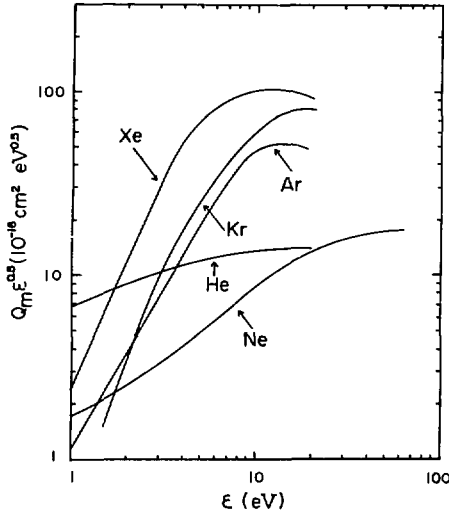
Fig. 7.14 Curves of $Q_m(\varepsilon)\varepsilon^{0.5}$ for monatomic gases cited from references in text.
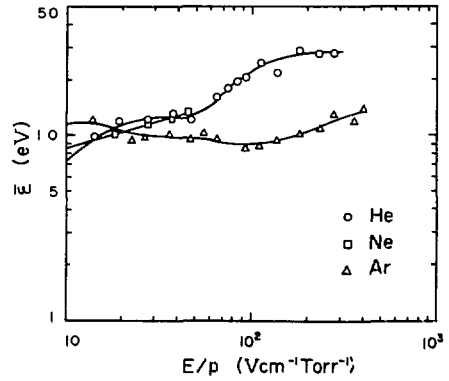
Fig. 7.15 Curves of ε as function of E/p for monatomic gases.

$$\frac{1}{n_0 l_i} = \left(\frac{2}{m_e}\right)^{\frac{1}{2}} \int_{IP}^{\infty} \varepsilon^{\frac{1}{2}} \sigma_i(\varepsilon) F(\varepsilon) d\varepsilon \qquad (7.3)$$

where IP is the ionization potential of a gas and $F(\varepsilon)$ the distribution function of secondary electron energy ε. Data on total ionization cross section σ_i for lower-energy electrons have been determined for some gases by Rapp and Englander-Golden[51,53].

The heavier monatomic gas gives the lower IP and the larger σ_i. Therefore, in order to give the larger t_i for the heavier gas as concluded from the order of D_{obs}, from Eq. (7.3), the larger part of secondary electrons must have ε lower than the IP. Data on $\bar{\varepsilon}$ corresponding to E_t/p in **Figs. 7.4** and **7.9**, estimated by Eq. (6.12), are shown as functions of E/p in **Fig. 7.15** for He[46], Ne[54,55], and Ar[46]. The total collision cross section for monatomic gases increases with increasing the atomic number[56].

7.2.3 Conclusion

It is concluded from the computational results for He and Ar that, when the variation of $Q_m \varepsilon^{0.5}$ is neglected among gases, the larger D_{obs} is given by the larger t_i. As compared the value of D_{obs} at the same pressure, the value of t_i can be estimated by Eqs. 7.1 and 7.3 by which t_i is related to molecular data for gases. This conclusion is demonstrated for all the monatomic gases.

8. Ionization of Inorganic Gases by Pulsed Beam

8.1 Computational Results of I_{net} for H_2 and N_2 [11]

8.1.1 H_2

The computation for H_2 as carried out by using σ_{ion} (480 keV) = 2.13 × 10^{-19} cm² [36], w [50], α_T/p [57], D_L/μ [58], Q_m [47], and $\alpha_r (H_2^+) = 4.7 \times 10^{-8} \varepsilon^{-0.4}$ [59]. Curves on $I_{net}(t)$ are shown in **Fig. 8.1**, in which t_B might be defined somehow or other up to 30 Torr but I_{net} after t_B is not constant even at 20 Torr. The corresponding E_z/p curves are shown in **Fig. 8.2**. The value of E_z/p for H_2 is lower than for Ar and rather higher than for He. Curves of $n_e(t)$ are shown in **Fig. 8.3** in which the curve is almost the same at pressures between 50 and 150 Torr at which D_{obs} is higher than 1 Mrad. The maximum value of $n_e(t)$ at near 3 ns is rather smaller than for He and Ar. Values of $\sigma_e(t)$ in **Fig. 8.4** become the maximum at 30 Torr as for He but about a half as large as for He. Curves of $\bar{\varepsilon}(t)$ estimated from D_L/μ for E_z/p in **Fig. 8.2** are shown in **Fig. 8.5**.

Fig. 8.1 Calculated curves of $I_{net}(t)$ for various pressures of H_2.
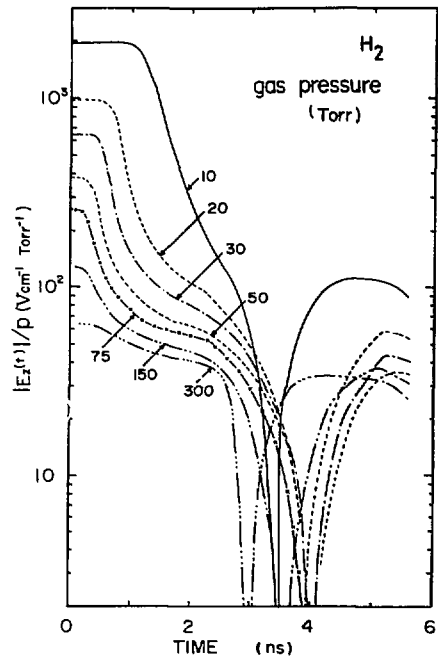
Fig. 8.2 Calculated curves of $E_z(t)/p$ for various pressures of H_2.
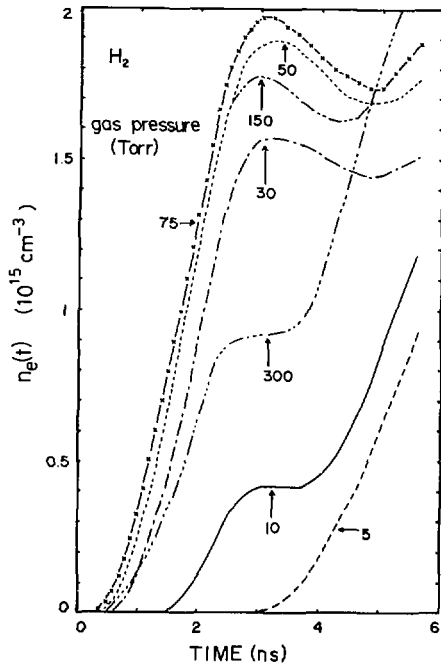
Fig. 8.3   Calculated curves of $n_e(t)$ for various pressures of H_2.
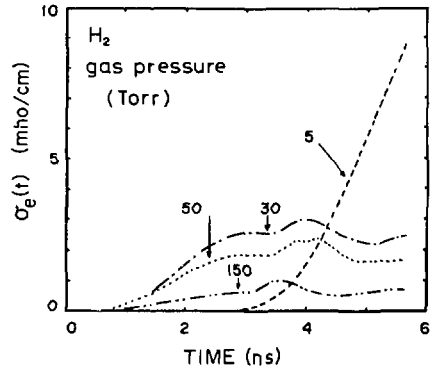
Fig. 8.4   Calculated curves of $\sigma_e(t)$ for various pressures of H_2.
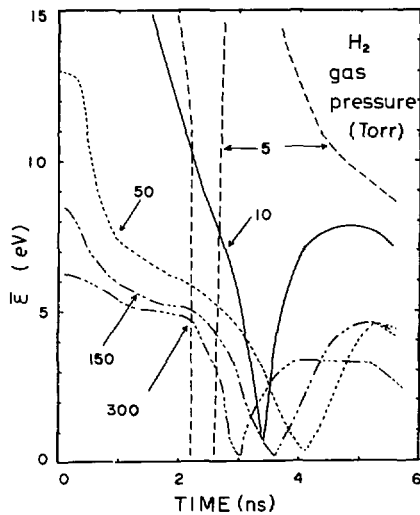
Fig. 8.5   Calculated curves of $\epsilon(t)$ for various pressures of H_2.

8.1.2 N_2

The computation for N_2 as carried out by using σ_{ion} (480 keV) = $9.15 \times 10^{-19}\,cm^2$ [36], w [50], α_T/p [60], D_L/μ [61], Q_m [47], $\alpha_r(N_2^+)$ [62], $k_d = 8 \times 10^{-29}\,molecule^{-2}\,cm^6\,s^{-1}$ [43], and α_{rd} [62]. Curves of $I_{net}(t)$ in **Fig. 8.6** show that, as for He, Ar, and H_2, the t_B model of $I_{net}(t)$ is valid

approximately up to the pressure at which D_{obs} is the minimum. The corresponding E_z/p curves in **Fig. 8.7** show that the value decreases with increasing pressure. Curves of $n_e(t)$ in **Fig. 8.8** show that the curve is almost the same at pressures between 30 and 75 Torr at which D_{obs} is higher than 1 Mrad, as for H_2 and that the maximum value at near 3 ns is smaller than for He, Ar, and H_2. Curves of $\sigma_e(t)$ in **Fig. 8.9** show that σ_e decreases with increasing pressure after passing the minimum D_{obs}. Curves of $\bar{\epsilon}$ estimated from D_L/μ for E_z/p in **Fig. 8.7** are
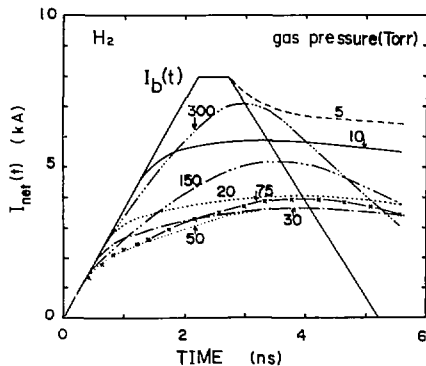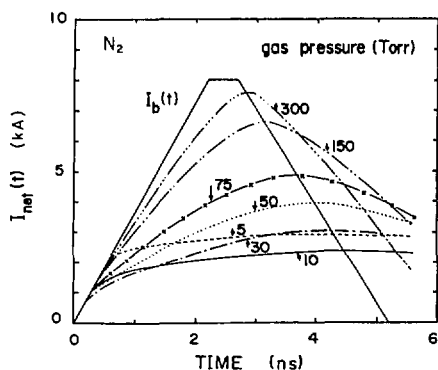

Fig. 8.6   Calculated curves of $I_{net}(t)$ for various pressures of N_2.
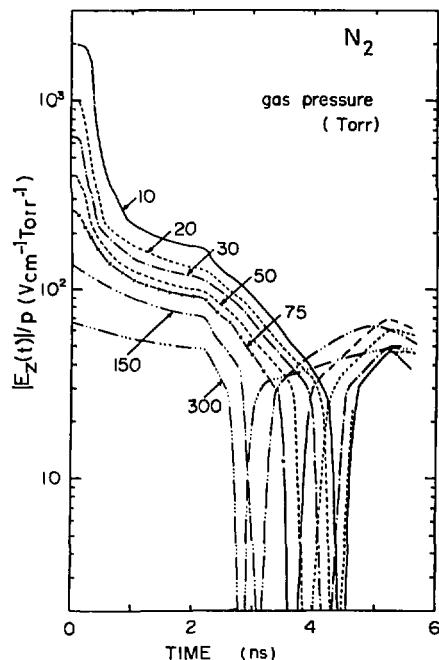
Fig. 8.7   Calculated curves of $E_z(t)/p$ for various pressures of N_2.
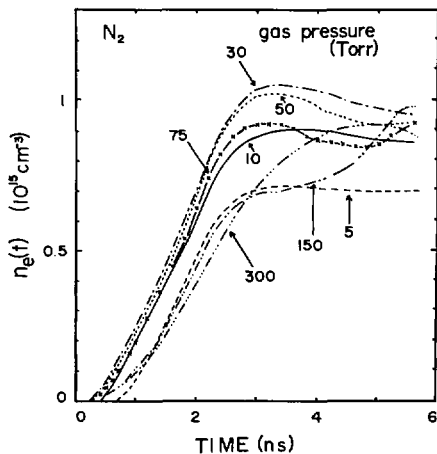
Fig. 8.8   Calculated curves of $n_e(t)$ for various pressures of N_2.
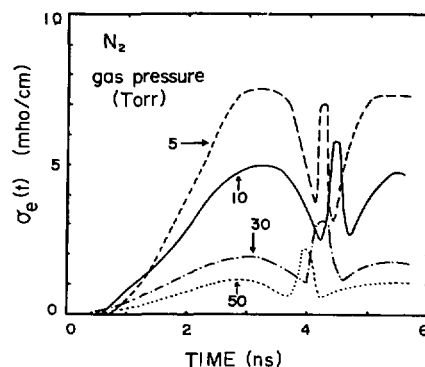
Fig. 8.9   Calculated curves of $\sigma_e(t)$ for various pressures of N_2.
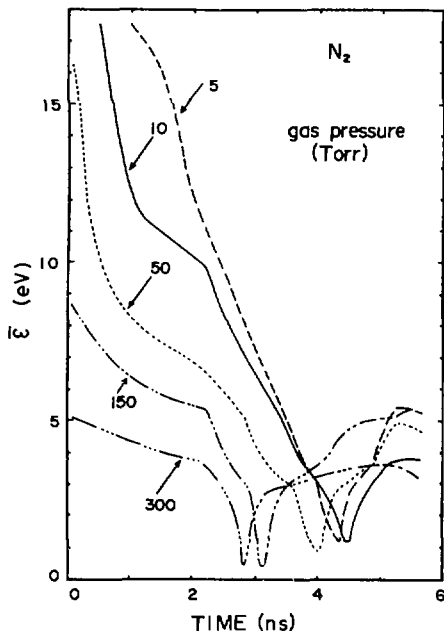
Fig. 8.10   Calculated curves of $\bar{\varepsilon}(t)$ for various   **Fig. 8.11**   Calculated curves of $n_e(t)$, $n_i(N_2^+)(t)$,
pressures of N_2.   and $n_d(N_4^+)(t)$ at 30 and 300 Torr of N_2.
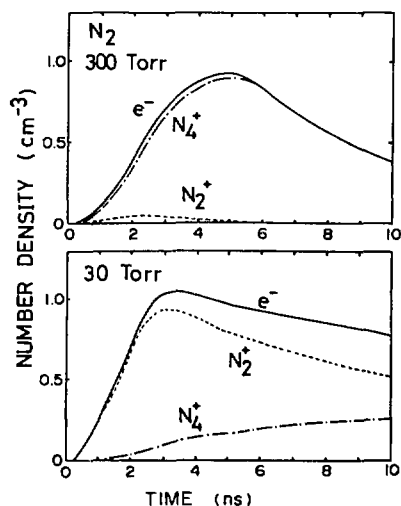
shown in **Fig. 8.10**. Some results for $n_i(N_2^+)$ and $n_d(N_4^+)$ are shown in **Fig. 8.11**. The curve indicates that $n_d(N_4^+)$ produced from $n_i(N_2^+)$ increases with increasing pressure but N_4^* does not recombine appreciably with secondary electrons for the major part of the pulse duration.

8.1.3 Contribution of electron-ion recombination processes

The contribution of each term to the total n_e in Eq. (6.16) can be summarized as follows, as a result of the computation for H_2, N_2, and CH_4 the result for which will be shown in **9.1**, although the computation was carried out for the discrete values of p. The contribution of direct ionization (term 1) is less than 10% of electron avalanching (term 2) at 20 − 150 Torr of H_2, 5 − 50 Torr of N_2, and 5 − 100 Torr of CH_4. Furthermore, the contribution of recombinations (terms 3 and 4) at 2.2 ns is less than 10% of the total n_e at pressures below 300 Torr of three gases. However, at higher pressure, the recombination processes contribute appreciably after 3 ns due to decreasing $\bar{\varepsilon}$ in the low E/p region and to the increasing contribution of term 4.

Generally speaking, since n_e is on the order of 10^{15} cm^{-3} from the present computation, the half life of secondary electrons is less than 1 ns only for α_r larger than 10^{-6} cm^3/s. Such large rate constants are reported only for N_4^{+}[49], O_4^{+}[49], and CH_4^* or CH_3^*[63] for thermal electrons and N_2O[64] for 0.04-eV electrons. Apparent recombination coefficients for N_2, CO_2, CH_4, C_3H_8, and neo-C_5H_{12}[65,66] are also larger than 10^{-6} cm^3/s at 50 Torr. When α_r is reduced according to $\bar{\varepsilon}^{-0.5}$, even for these gases, the value may be reduced down to the order of 10^{-7} cm^3/s; as demonstrated by the present computation, the recombination processes for N_2 and CH_4 are not affected appreciably for the major part of the pulse duration in the pressure region in interest.

8.1.4 Comparison of the calculated I_{net} with data on D_{obs}

As described in **7.2.1**, values of $\int_0^{t_p} I_b(t)I_{net}(t)dt$ are plotted in an arbitrary unit as functions of p by closed marks for H_2 (●), N_2 (▲), and CH_4 (■) in **Fig. 8.12**. The corresponding values of D_{obs} are plotted by open marks also in **Fig. 8.12**. The curves represent fairly well the aspect of the D_{obs}-p curve except the value at the minimum. The discrepency of the minimum can be solved as discussed in **7.2.1**.
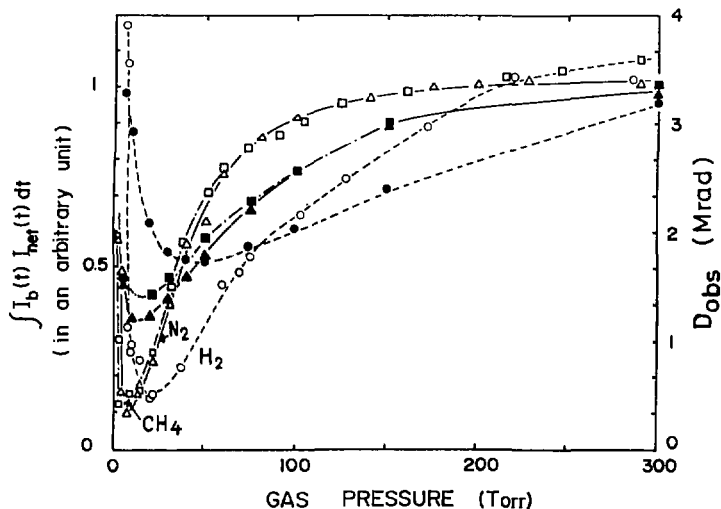
Fig. 8.12   Data on $D_{obs}(p)$ for H_2 (○), N_2 (△), and CH_4 (□) and values of $\int_0 I_b(t)I_{net}$

(*t*)*dt* calculated from $I_{net}(t)$ in Figs. 8.1, 8.6, and 9.1, which are plotted
in an arbitrary unit by the corresponding closed marks.

8.1.5 Conclusions

The same conclusion as described for He and Ar in **7.1.3** can be derived from the computational results for H_2, N_2, and CH_4. As described in **8.1.4**, the aspect of $D_{obs}(p)$ can be expressed fairly well by Eq. (2.26) by using the calculated $I_{net}(t)$. This means that the present computational scheme in 6.2 represents fairly well the phenomena induced by the pulsed beam in a gas chamber. Therefore, the calculated values of parameters such as n_e and E_z/p might represent semi-quantitatively the data for the above phenomena. The computational results show that the great part of secondary electrons are produced by electron avalanching (term 2 in Eq. (6.16)) and that, for most of polyatomic gases, the recombination processes have no substantial effect on $I_{net}(t)$ for the major part of the pulse duration in the pressure region in interest.

8.2 Discussion

8.2.1 Relationship between D_{obs} and t_i

It is concluded in **7.2.2** that, when the variation of $Q_m \bar{\varepsilon}^{0.5}$ is neglected among gases, the larger D_{obs} is given by the gas giving the larger t_i or $p t_i$ at the same pressure. Values of $Q_m \bar{\varepsilon}^{0.5}$ for some polyatomic gases[47,52,67] are shown as functions of ε **in Fig. 8.13**. The value is almost the same for ε around 7 eV. Therefore, data on $D_{obs}(p)$ might be analyzed approximately in terms of $p t_i$ and E_z/p.
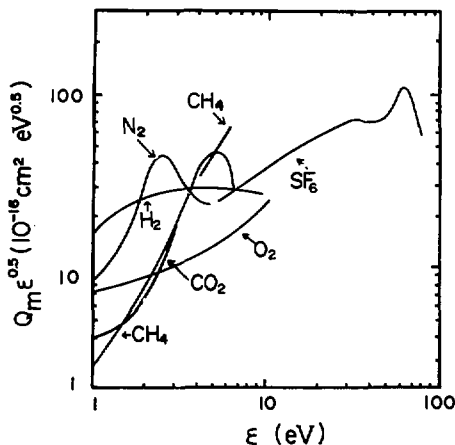
Fig. 8.13   Curves of $Q_m \epsilon^{0.5}$ for some polyatomic gases plotted against ϵ.

The relationship between E/p and pt_i has been reported by Felsenthal and Proud[42] as shown in **Fig. 8.14**; pt_i increases with decreasing E/p. From the above conclusion, the curve for the gas giving the larger D_{obs} at the same pressure must be placed at the upper side in such a figure. In fact, in **Fig. 8.14**, the value of E/p at the same pt_i is in the order.

$$CCl_2F_2 > SF_6 > N_2 > O_2 > Ar > He. \qquad\qquad (8.1)$$

This is the same with the order of D_{obs} at the same pressure as seen in **Figs. 7.2** and **8.15** in which data on D_{obs}[3,4,5,8] are summarized. On the other hand, the value of pt_i can be estimated by either Eq. (7.1) or (7.3) for a gas with no electron-attachment process. Therefore, at first, we examine the contribution of η_T to t_i in Eq. (6.15) in **8.2.2**.
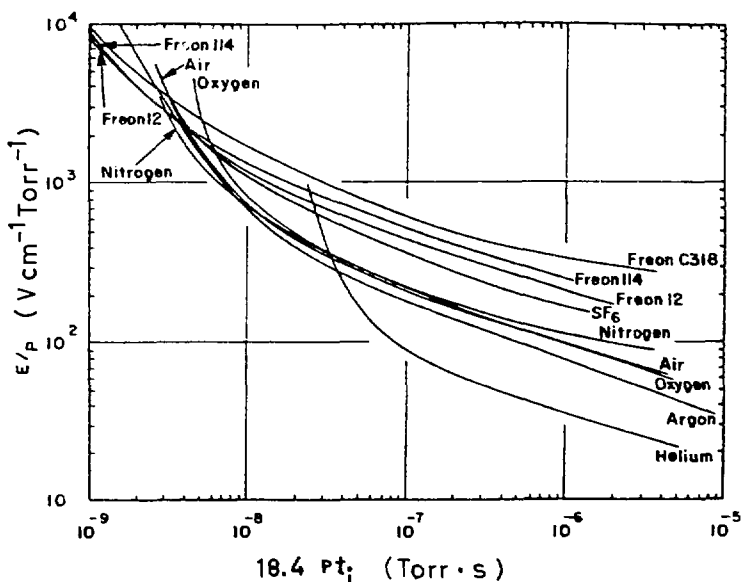
Fig. 8.14   The relationship between pt_i and E/p cited from the paper of Felsenthal and Proud[42].
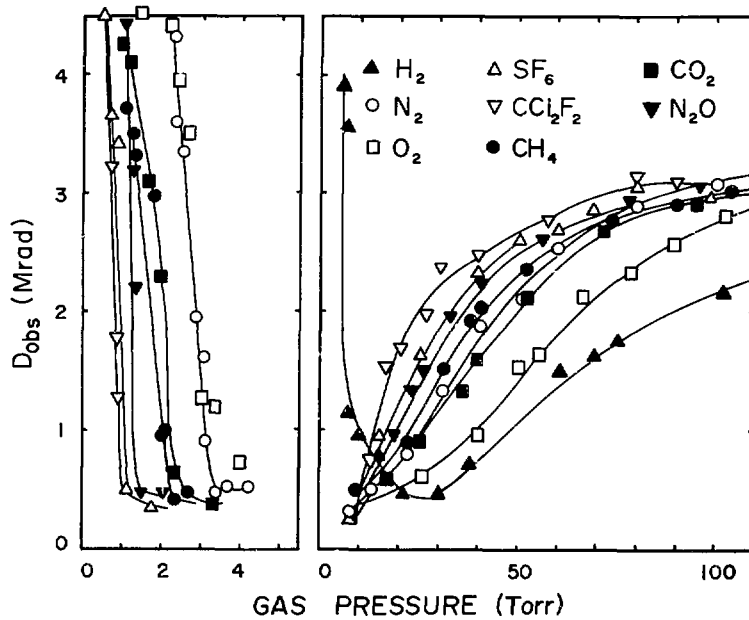
Fig. 8.15   Data on $D_{obs}(p)$ for some polyatomic gases.

8.2.2 Electron-attachment processes

Values of α_T/p and η_T/p have been measured as functions of E/p for SF_6[68], CCl_2F_2[69], N_2O[70], O_2[69], and CO_2[71] as shown in **Figs. 8.16** and **8.17**. The value of α_T/p at 100 Vcm^{-1} $Torr^{-1}$ is 74% for SF_6 against CO_2 and 60% for CCl_2F_2[72] against CO_2 and, furthermore, the
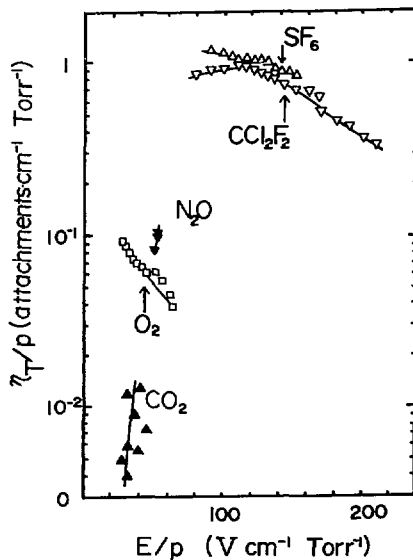
Fig. 8.16   Data on η_T/p as functions of E/p cited from references in text.
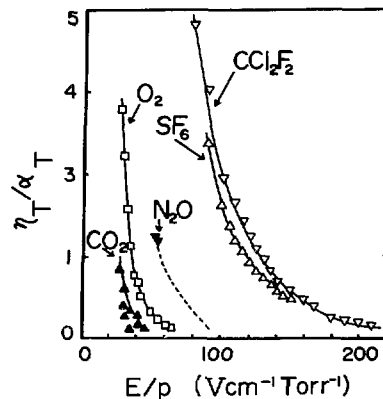
Fig. 8.17   Data on η_T/α_T as functions of E/p cited from references in text.

value at 50 $Vcm^{-1} Torr^{-1}$ is 58% for $N_2 O^{70,73)}$ against CO_2. On the other hand, the value of η_T/p is in the order (Fig. 8.16)

$$SF_6 \approx CCl_2F_2 \gg N_2O > O_2 > CO_2 . \qquad (8.2)$$

Then, the ratio of η_T/α_T is in the order (Fig. 8.17)

$$CCl_2F_2 > SF_6 \gg N_2O > O_2 > CO_2 . \qquad (8.3)$$

These data indicate that this ratio is negligibly small in O_2 and CO_2 for $E/p > 60$ $Vcm^{-1} Torr^{-1}$. Therefore, for CCl_2F_2, SF_6, and N_2O, the value of t_i must be lengthened due to the contribution of η_T to t_i so as to give the larger D_{obs}. In fact, the order of D_{obs} at the same pressure in **Fig. 8.15** is the same with the order (8.3).

Generally speaking, since the number density of gas molecule is $3.3 \times 10^{18} cm^{-3}$ at 20°C and 100 Torr, the half life of secondary electrons must be less than 1 ns for the rate constant of the electron-attachment process k_a larger than $2 \times 10^{-10} cm^3/s$. Such large rate constants have been reported for O_2 (3.4×10^{-10} at 6.7 $eV^{51)}$), $N_2 O$ (9.2×10^{-10} at 2.4 $eV^{51)}$), SF_6 (2×10^{-7} at thermal and 1.1×10^{-7} at 0.37 $eV^{74)}$), and CCl_2F_2 (5.6×10^{-9} at 1.08 $eV^{74)}$ and 7.7×10^{-10} at 3.5 $eV^{75)}$). These molecular data support the above data on swarm parameters.

8.2.3 Energies of secondary electrons

Data on $\bar\varepsilon$ estimated from D_L/μ by Eq. (6.12) are shown as functions of E/p in **Fig. 8.18** for $H_2^{58)}$, $N_2^{61)}$, $O_2^{55,76)}$, $CO_2^{77)}$, $CH_4^{46)}$, $SF_6^{78)}$, and $CCl_2F_2^{79)}$. The value of $\bar\varepsilon$ is about 7 – 8 eV at 100 $Vcm^{-1} Torr^{-1}$ for the gases other than CCl_2F_2 (5.5 eV) and, at 50 Vcm^{-1} $Torr^{-1}$, in the order

$$CH_4 > H_2 \approx O_2 \approx CO_2 \approx (SF_6) > N_2 > CCl_2F_2 . \qquad (8.4)$$

Values for SF_6 and CCl_2F_2 are extrapolated from the data at 100 $Vcm^{-1} Torr^{-1}$.

Secondary electrons with higher energies must be slowed down by collisions with molecules through $Q_t f$ where Q_t is the total collision cross section and f the mean fractional energy loss per collision which is given by[80)]

$$f = 1.74 \times 10^{-14} w^2 / k_T . \qquad (8.5)$$

In Eq. (8.5), the Townsend energy factor k_T equals 39.8 D_L/μ at 20°C for the Maxwellian. On the other hand, once secondary electrons ionize a gas, their energy becomes nearly thermal and their acceleration by E/p is more retarded by the gas with the larger $Q_t f$ for electrons
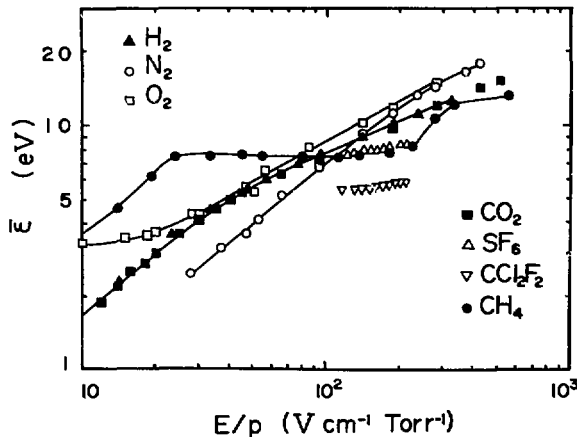
Fig. 8.18 Curves of $\bar\varepsilon$ as functions of E/p estimated from data on D_L/μ in references in text.

with lower energies.

Curves of $Q_t f$ are shown as function of $\bar{\varepsilon}$ in **Fig. 8.19**. These values are estimated from data on D_L/μ cited above and on Q_t for H_2 [81], N_2 [56], O_2 [82,83], CO_2 [56], CH_4 [52], and SF_6 [84]. The curves shown by dotted lines in **Fig. 8.19** are cited from the data of Christophorou and Carter[85] who calculated them on the assumption of the Druyvesteynian. As comparing the curves between **Figs. 8.18** and **8.19**, the high value of $\bar{\varepsilon}$ for CH_4 at lower E/p is attributed to the small value of $Q_t f$ for lower $\bar{\varepsilon}$ because of the special dependence of D_L/μ on E/p [46]; the low value for N_2 at lower E/p is attributed to the large value of $Q_t f$ for lower $\bar{\varepsilon}$; and also the middle values for O_2, CO_2, and SF_6 are understood by their curves of $Q_t f$. This means that $Q_t f$ from Eq. (8.5) is useful to presume qualitatively the form of $F(\varepsilon)$ in Eq. (7.3) by which t_i is determined mainly, although there is some problem for the application of Eq. (8.5) to the higher E/p region.

The peak of $Q_t f$ for lower $\bar{\varepsilon}$ as seen for N_2 and N_2O in **Fig. 8.19** retards the acceleration of nearly thermal electrons after ionization as pointed out already so that such electrons might not ionize molecules again for the ns pulse duration; that is, such a peak lengthens t_i. According to Kennerly, Bonham, and McMillan[84], the value of Q_t for SF_6 is 3.6×10^{-15} cm² for 0.5 eV electrons, becomes the minimum (2.2×10^{-15} cm²) for 4 eV ones, and increases again gradually up to 3.1×10^{-15} cm² for 12 eV ones; that is, the same effect as for N_2 and N_2O might be expected also for SF_6. Consequently, the longer t_i or the larger D_{obs} can be expected
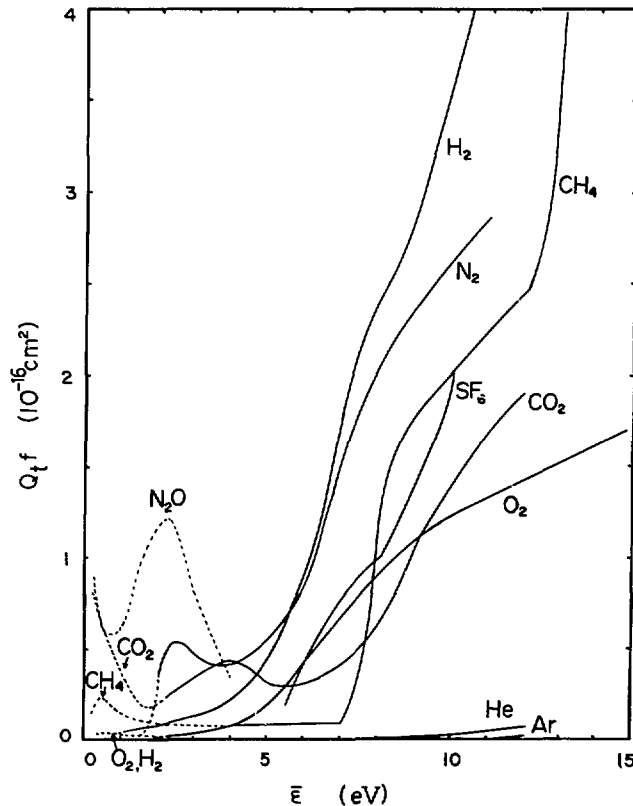
Fig. 8.19   Curves of $Q_t f$ as functions of $\bar{\varepsilon}$ estimated from data in references in text.
Dotted curves are estimated by using f in ref. 85.

for N_2O and SF_6 not only from the electron-attachment process neglected for Eqs. (7.1) and (7.3) but also from the data on $Q_t f$ for lower $\bar{\varepsilon}$.

Electron thermalization in gases has been discussed theoretically for monatomic gases[86,87] and determined experimentally for some polyatomic gases[80,88,89]. According to the data, the thermalization time at 30 Torr ($E/p = 0$) is about or less than 1 ns for CO_2, N_2O, C_2H_2, C_2H_4, and neo-C_5H_{12}.

8.2.4 Interpretation of D_{obs} in terms of swarm parameters

Data on D_{obs} for gases other than N_2O, SF_6, and CCl_2F_2 with large η_T as described in **8.2.2** should be interpreted in terms of w and α_T/p by Eq. (7.1). Data on w[50] are shown as functions of E/p in **Fig. 8.20** for H_2, N_2, O_2, CO_2. and CH_4[90,91] and data on α_T/p are shown in **Fig. 8.21** for H_2, N_2, O_2, CO_2, and CH_4[92]. Although E/p varies over the pulse duration, we attempt to estimate the value of $p/w\alpha_T$ or $p t_i$ from data in **Figs. 8.20** and **8.21** at 100 $Vcm^{-1}Torr^{-1}$ as the representative value of E/p between 20 and 50 Torr. The value of $p/w\alpha_T$ is in the order

$$N_2 > CO_2 > CH_4 > O_2 > H_2. \qquad (8.6)$$

This order is almost the same with the order of D_{obs} at the same pressure in **Fig. 8.15** except CH_4;

$$CH_4 \gtrsim N_2 \gtrsim CO_2 > O_2 > H_2. \qquad (8.7)$$

The value of $\bar{\varepsilon}$ at 100 $Vcm^{-1}Torr^{-1}$ is about 8 eV for these gases as shown in **Fig. 8.18**. In **Fig. 8.14**, the value of $Q_m \varepsilon^{0.5}$ for 8 eV is about $2.5 \times 10^{-15} cm^2 eV^{0.5}$ for the gases other than CH_4 for which the value is $7 \times 10^{-15} cm^2 eV^{0.5}$[93]. The order of D_{obs} for CH_4 can be interpreted in terms of this large value of $Q_m \bar{\varepsilon}^{0.5}$ in Eq. (6.10) as well as $p t_i$ or $w\alpha_T/p$.
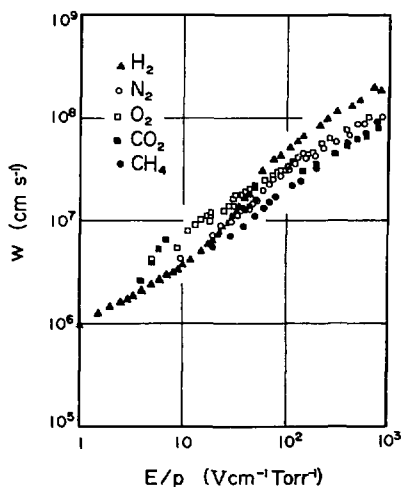
Fig. 8.20   Curves of w as functions of E/p cited from references in text.
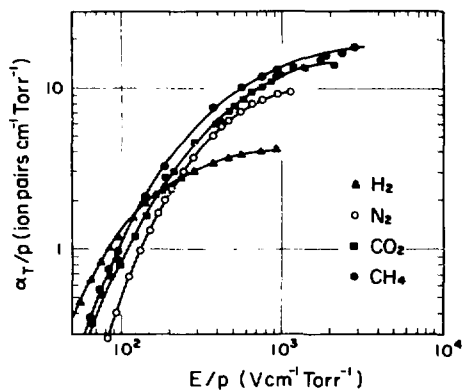
Fig. 8.21   Curves of α_T/p as functions of E/p cited from references in text.

8.2.5 Interpretation of D_{obs} in terms of molecular data

Equation (7.1) is rewritten in the form of Eq. (7.3). According to the Eq. (7.3), the larger t_i or D_{obs} is given by the gas with the higher IP, the slower initial slope of σ_i against ε, and the larger distribution of $F(\varepsilon)$ at the lower-ε side. Data on σ_i and IP for lower-energy
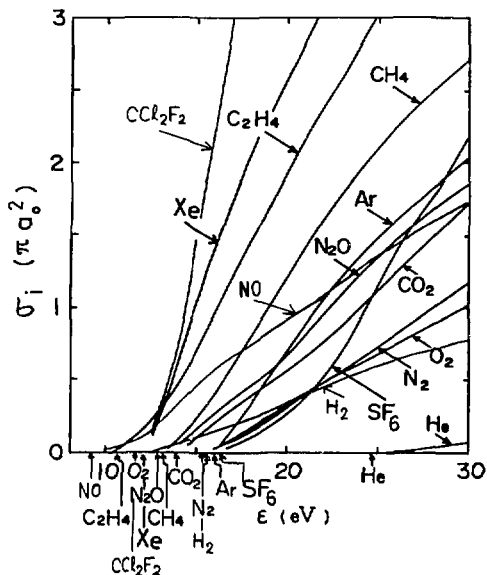
Fig. 8.22   Curves of σ_i as functions of ϵ cited from the data of Rapp and Englander-Golden[53]. The curve of CCl_2F_2 is cited from ref. 75. a_0 = the frist Bohr radius. The arrows under the abscissa indicate the ionization potentials of the respective gases.

electrons are given by Rapp and Englander-Golden[51,53] as shown in **Fig. 8.22**. The curve for CCl_2F_2 is cited from ref. 75. Data on $F(\epsilon)$ are already discussed in **8.2.3**.

In **Figs. 8.19** and **8.22**, N_2 has the highest IP, the smallest σ_i, and the largest $Q_i f$ roughly among the gases shown in **Fig. 8.15**. Therefore, the value of pt_i for N_2 becomes the largest among the gases so that, at the same pressure, D_{obs} for N_2 should be the largest among these gases. In fact, D_{obs} at the same pressure in **Fig. 8.15** increases roughly with reducing IP, decreasing σ_i, and also decreasing $Q_i f$ among N_2, CO_2, and O_2 as shown by the order (8.7), although these three factors are rather complicated. The large value of $Q_m \bar{\epsilon}^{0.5}$ must be noticed for CH_4 as described in **8.2.4**. Since SF_6 as the IP higher than N_2, almost the same σ_i with N_2 between 15 and 22 eV, and furthermore the large k_a at thermal and around 0.4 eV, the value of D_{obs} for SF_6 becomes larger than for N_2 as seen in **Fig. 8.15**. That for N_2O is rahter smaller than for SF_6 and much larger than for N_2 despite of almost the same σ_i curve between both the gases in **Fig. 8.22**. This fact for N_2O must be attributed to the peak of $Q_i f$ and the larger k_a around 2.4 eV. The largest value of D_{obs} for CCl_2F_2, despite of the low IP and the large σ_i, will be discussed in **9.2**. Swarm data as shown in **Figs. 8.16** and **8.17** are determined by various parameters such as IP, σ_i, $F(\epsilon)$, and k_a. As pointed out in **8.2.2** and **8.2.3**, for N_2O, SF_6, and CCl_2F_2, the value of t_i is strongly affected not only by k_a but also $Q_i f$

The value of D_{obs} for H_2 is the lowest as seen in **Fig. 8.15** despite of the highest IP and the smallest σ_i among polyatomic gases. This small value may be due to the small $Q_i f$ for secondary electrons lower than 5 eV as shown in **Fig. 8.19**.

8.2.6 Conclusion

As the analytical result of the computed I_{net} in **8.2.1**, at the same pressure, the larger D_{obs} is concluded to be given by the longer t_i if the variation of $Q_m \bar{\epsilon}^{0.5}$ is neglected among

gases. This conclusion is supported by the experimental data on t_f by Felsenthal and Proud[42]. For gases other than studied by them, the value of t_i is given by Eq. (6.15). As described in **8.2.4**, the swarm parameters for Eq. (6.15) support the above conclusion for the relationship between D_{obs} and t_i except CH_4 which has the large value of $Q_m \bar{\varepsilon}^{0.5}$. Generally speaking, since Eq. (6.15) or (7.1) is rewritten as Eq. (7.3), data on D_{obs} can be analyzed in terms of IP, σ_i, and $F(\varepsilon)$ in Eq. (7.3). The interpretation of data on D_{obs} for gases as shown in **Fig. 8.15** in terms of these molecular data is given in **8.2.5**. The form of $F(\varepsilon)$ can be presumed by the curve of $Q_i f$ as shown in **Fig. 8.19**. It is concluded from the discussion in this chapter that data on D_{obs} can give information on t_i for the pulse duration which is not easy to be measured directly.

9. Ionization of Organic Gases by Pulsed Beam

9.1 Hydrocarbons

9.1.1 CH$_4$ [11)]

The computation of I_{net} was carried out by using $\sigma_{ion}(CH_4) = 1.10 \times 10^{-18}\,cm^2$ [36)], w [90,91,94)], α_T/p [92)], D_L/μ [46)], and Q_m [52,56)]. It was assumed as secondary reactions that

$$CH_4 \overset{\text{\textasciitilde}}{\longrightarrow} CH_3^+ + H + e$$

$$CH_3^+ + CH_4 \overset{k}{\longrightarrow} C_2H_5^+ + H_2$$
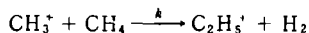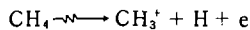
$$(k = 1 \times 10^{-9}\,cm^3/s\,)^{95)}$$

and also

$$\alpha_r = 5.5 \times 10^{-8}\,\bar{\varepsilon}^{-0.93}\quad \text{for } \bar{\varepsilon}\;0.8\;\text{eV}^{63)}$$

$$\alpha_{rd} = 9.5 \times 10^{-5}\,\bar{\varepsilon}^{-0.75}\quad \text{for } \bar{\varepsilon}\;1\quad \text{eV}^{63)}$$

The results are shown in **Fig. 9.1** for $I_{net}(t)$, in **Fig. 9.2** for E_z/p, in **Fig. 9.3** for $n_e(t)$, and in **Fig. 9.4** for $\sigma_e(t)$. Curves of $\bar{\varepsilon}$ estimated from D_L/μ for E_z/p in **Fig. 9.2** are shown as functions of t in **Fig. 9.5**. Although $\bar{\varepsilon}$ might not reduce immediately as shown in **Fig. 9.5** against the abrupt reduction of E_z/p in **Fig. 9.2**, the present computation was carried out according to the curve in **Fig. 9.5**. The constancy of 7.4 eV for the long period is due to the specific dependence of D_L/μ on E/p [46)]. Curves of $n_e, n_i(CH_3^+)$, and $n_d(C_2H_5^+)$ at 30 and 300 Torr are shown as examples in **Fig. 9.6**. At higher pressure, the greater part of CH_3^+ is converted
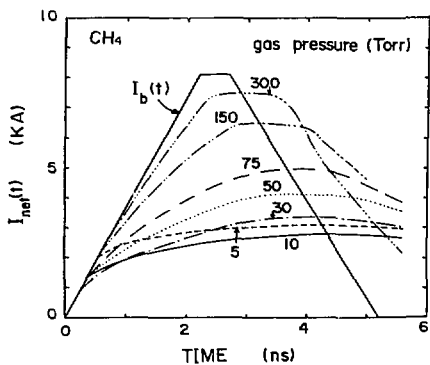
Fig. 9.1   Calculated curves of $I_{net}(t)$ for various pressures of CH$_4$.
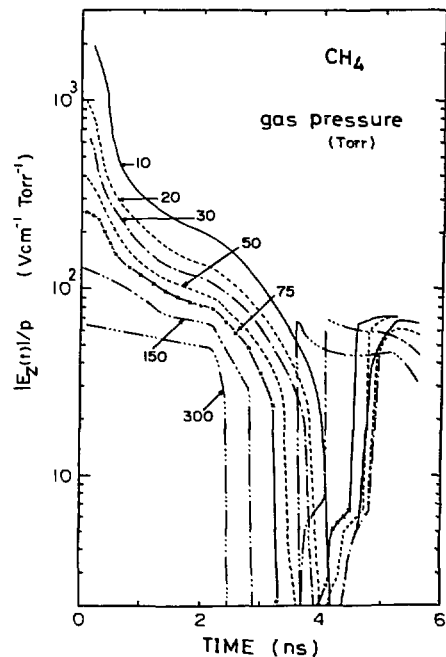
Fig. 9.2   Calculated curves of $E_z(t)/p$ for various pressures of CH$_4$.
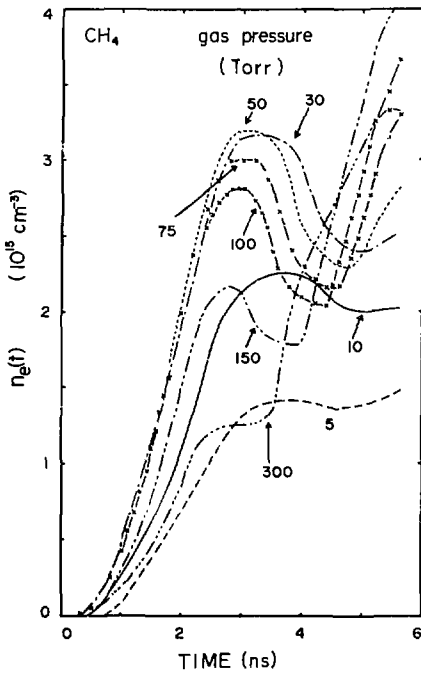
Fig. 9.3 Calculated curves of $n_e(t)$ for various pressures of CH_4.
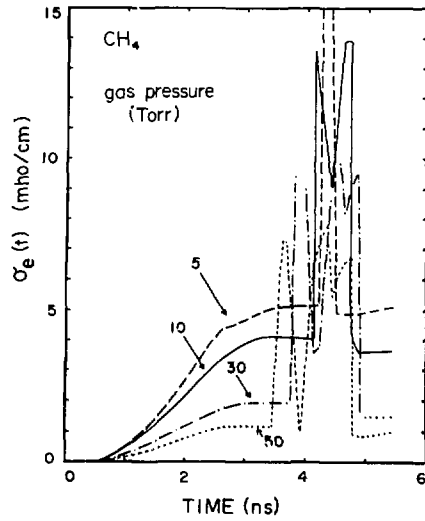
Fig. 9.4 Calculated curves of $\sigma_e(t)$ for various pressures of CH_4.
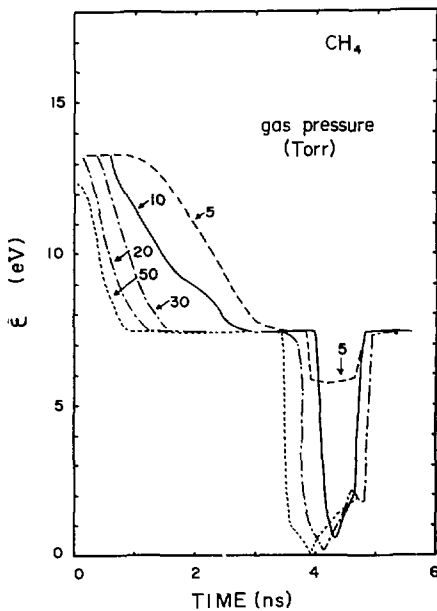
Fig. 9.5 Calculated curves of $\bar{\varepsilon}(t)$ for various pressures of CH_4.
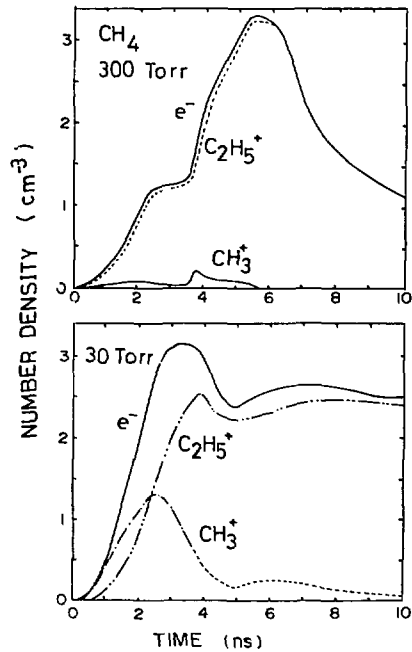
Fig. 9.6 Calculated curves of $n_e(t)$, $n_i(CH_3^+)$ (t), and $n_d(C_2H_5^+)(t)$ at 30 and 300 Torr of CH_4.

immediately to $C_2H_5^+$ which survives without recombination with secondary electrons for the ns pulse duration.

The curve of $\int_0^{t_p} I_b(t)I_{net}(t)dt$ for CH_4 in **Fig. 8.12** indicates the good reliability of the present computation as discussed already in **8.1.4**. The interpretation of D_{obs} (CH_4) by Eq. (7.1) is already described in **8.2.4**.

9.1.2 Other alkanes

Data on D_{obs} are shown in **Fig. 3.11**. The value at pressure lower than 50 Torr is almost the same between CH_4 and C_2H_6 and, larger for C_3H_8 than for C_2H_6. Data for other alkanes are shown in ref. 5.

The value of w at E/p lower than 15 $Vcm^{-1}Torr^{-1}$ decreases with increasing carbon number[94,96,97]. The data for CH_4 are shown in **Fig. 8.20**. On the other hand, as shown in **Fig. 9.7**, the value of α_T/p at E/p lower than 300 $Vcm^{-1}Torr^{-1}$ is almost the same between CH_4[92] and C_2H_6[98] and less for C_3H_8[98] than for CH_4. According to these data, D_{obs} in **Fig. 3.11** can be interpreted by Eq. (7.1).

Data on D_L/μ at E/p lower than 5 $Vcm^{-1}Torr^{-1}$ are known for CH_4[99], C_2H_6[100], and C_3H_8[100]. The value of $\bar{\varepsilon}$ at 5 $Vcm^{-1}Torr^{-1}$ estimated from Eq. (6.12) is about 2.5, 0.9, and 0.3 eV for CH_4, C_2H_6, and C_3H_8 respectively. As considering these data with E_s/p computed for CH_4 and thermalization time[88,89], $\bar{\varepsilon}$ is supposed to be lowered with increasing carbon number appreciably down to lower than IP. Therefore, data on D_{obs} can be also interpreted by Eq. (7.3) approximately. The value of α_r for 0.04-eV electrons is fairly large as described in **8.1.3**.
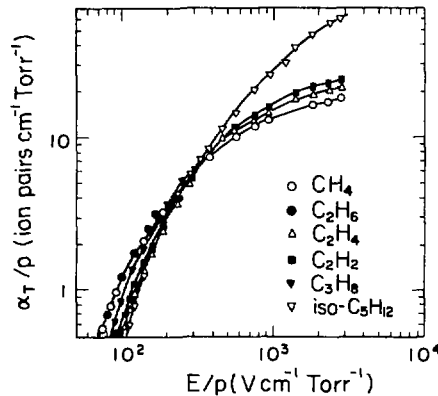
Fig. 9.7   Curves of α_T/p as functions of E/p for hydrocarbons.

9.1.3 C_2H_2, C_2H_4, and C_2H_6

As shown in **Fig. 9.8**, the value of D_{obs} is almost the same between C_2H_4 and C_2H_6 and rather larger for C_2H_2. Data on w are known at E/p up to 40 $Vcm^{-1}Torr^{-1}$ for C_2H_4[101] and up to 15 $Vcm^{-1}Torr^{-1}$ for C_2H_2 and C_2H_6[97]. These data at E/p higher than 10 $Vcm^{-1}Torr^{-1}$ is in the order

$$C_2H_2 > C_2H_4 > C_2H_6 . \tag{9.1}$$

On the other hand, data on α_T/p[92] show that the value is almost the same between C_2H_2 and C_2H_4 over the whole range and that for C_2H_6 is almost the same with them at 100 Vcm^{-1} $Torr^{-1}$ and larger at the lower E/p than for C_2H_2 and C_2H_4. The value of D_L/μ or $\bar{\varepsilon}$ at E/p
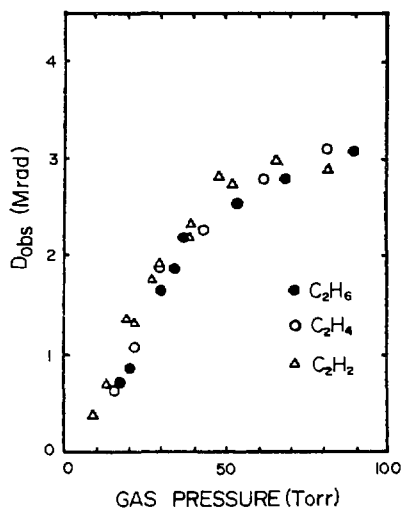
Fig. 9.8   Data on D_{obs} as functions of pressure for C_2H_6, C_2H_4, and C_2H_2.
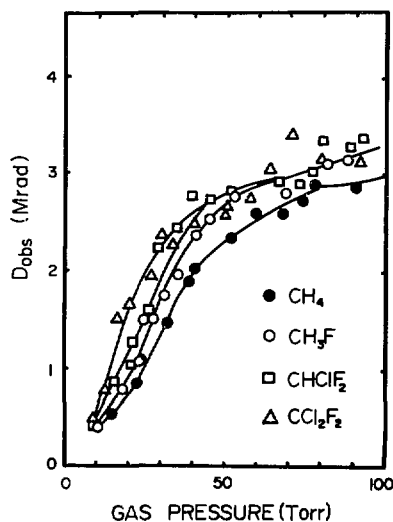
Fig. 9.9   Data on D_{obs} as functions of pressure for halogenomethanes.

lower than 5 $Vcm^{-1}Torr^{-1}$ for C_2H_4 is nearly equal to that for C_3H_8 and lower than for C_2H_6[99]. These data are consistent with t, estimated from Eqs. (7.1) and (7.3).

9.2 Halogenomethanes

Data on $D_{obs}(p)$ for CH_4, CH_3F, $CHClF_2$, and CCl_2F_2 are shown in **Fig. 9.9**. Although the data are rather scattered, the slope of the rising D_{obs} around 10 Torr becomes steeper with increasing the number of halogen atoms, especially, Cl atom. The value of Q_t increases considerably with increasing Cl atom and has the peak for low ε but almost the same between CH_4 and CH_3F[56]. The strong reduction of $\bar{\varepsilon}$ is expected for the large Q_t. The electron-ion recombination coefficient should increase with increasing the complexity or size of a molecule and with reducing $\bar{\varepsilon}$. Moreover, the electron-attachment rate constant increases with increasing halogen atom, especially, Cl atom because of the large electronegativity[102,103]. Data on w are known for CCl_2F_2 at $115 - 210\ Vcm^{-1}Torr^{-1}$[79] and for $CHClF_2$ at low E/p[104]. These data for these halogenomethanes are reflected to data on D_{obs} for them by Eqs. (6.15), (7.1), and (7.3). In **Fig. 8.15**, D_{obs} for CCl_2F_2 is larger than for SF_6 despite of the large σ_i and low IP (**Fig. 8.22**) and also the value of k_a smaller than for SF_6. This larger D_{obs} is due to the Q_t for Cl at low ε larger than for F[56] and the resonance energy of the electron attachment for CCl_2F_2 (1.08 eV[74] and 3.5 eV[75]) higher than for SF_6 (0.37 eV). Such peaks at higher ε must reduce n_e more efficiently than the peak at lower ε.

10.   Effect of Additives to He, Ar, and O_2

10.1   Introduction[12]

As described already in detail, D_{obs} on the beam axis increases gradually with increasing pressure after passing the minimum; usually D_{obs} becomes the minimum at $5-10$ Torr of polyatomic gases. The value of D_{obs} at $10-100$ Torr is relatively small in He, Ar, and O_2 as compared with other gases. When polyatomic gases were added to these gases, the increase of D_{obs} with pressure was enhanced so that the beam was self-focused more strongly. At first[6], the effect of additives has been discussed on the basis of the promotion of electron-ion recombination processes due to slowing-down of secondary electrons by additives and of the occurence of charge-transfer processes to additive molecules. However, such an interpretation is rather inconsistent with the conclusion in the foregoing chapters that these slow processes can be neglected for the beam with the ns pulse duration because the value of n_e is on the order of $10^{15}cm^{-3}$ at the largest as the computational result. Penning ionization processes can also be neglected in this case because of their slow rate. Consequently, in this chapter, the previous data for the mixtures[6] are re-examined on the basis of t_i lengthened by additives. In this chapter, E/p represents E_z/p. Gaseous mixtures used for the present study were prepared in advance in a large reservoir for each run.

10.2   Estimation of t_i in a Binary Mixture

When there are no effective electron-attachment and Penning-ionization processes, we can assume the equation of t_i in a binary mixture as

$$\frac{1}{n_0 t_i} = \left(\frac{2}{m_e}\right)^{\frac{1}{2}} \left[\int_{IP_1}^{\infty} x \varepsilon^{\frac{1}{2}} \sigma_{i1}(\varepsilon) F(\varepsilon) d\varepsilon + \int_{IP_2}^{\infty} (1-x) \varepsilon^{\frac{1}{2}} \sigma_{i2}(\varepsilon) F(\varepsilon) d\varepsilon \right]$$

(10.1)

analogously with Eq. (7.3) where x is the mole fraction of a host gas 1 and the index 2 is referred to an additive gas. This equation indicates that the effect of additives on t_i in the mixture can be estimated in terms of the IP_2 of the additive relative to IP_1 of the host gas, the initial slope of σ_i against ε, and the shift of $F(\varepsilon)$ in the presence of the additive. Yamane[105] has interpreted his experimental data of α_T/p in Ar mixtures in terms of the similar parameters; the initial slope of energy dependence of σ_i, IP of additives relative to that of a host gas, the average fractional energy loss per collision, and the mean energy of secondary electrons $(\bar{\varepsilon})$.

Data on σ_i and IP for lower-energy electrons obtained by Rapp and Englander-Golden[53] are shown in **Fig. 8.22**. As described in **8.2.3**, the $Q_t f - \varepsilon$ curve as shown in **Fig. 8.19** is useful to presume the form of $F(\varepsilon)$. Then, data on D_{obs} in the present mixtures might be interpreted qualitatively in terms of the lengthened t_i estimated by Eq. (10.1) in referring to data on these parameters.

In Eq. (10.1), the first integral represents the contribution of a host gas to t_i. When this integral is very small compared to the second integral for an additive, t_i in the mixture is mainly determined by the properties of the additives; in other words, for such a case, D_{obs} in the mixture can be presumed from D_{obs} in the pure additive. Since He has the highest IP and the small σ_i, the contribution of He to t_i for He mixtures becomes easily negligibly small

by addition of polyatomic gases which make $F(\varepsilon)$ shift to the lower-ε side. Since He has the small σ_i, secondary electrons generated from He contribute hardly to the second integral. Therefore, D_{obs} in He mixtures should be generally estimated by D_{obs} in He mixtures should be generally estimated by D_{obs} in pure additive. This is approximately realized for the present data for the mixtures other than with N_2 as described in **10.3**.

The situation of Ar in Ar mixtures is not so simple as in He mixtures because Ar has the large σ_i and the intermediate IP. Furthermore, according to data on D_L/μ[46], $\bar{\varepsilon}$ in Ar is supposed not to be reduced from 9 eV down to E/p of a few Vcm^{-1} Torr^{-1}. Then, secondary electrons in the pulsed-beam channel are not retarded in Ar so that they have plenty of chances for ionization which are lost only by the retardation by additive molecules. In fact, the effect of the enhancement is weak for Ar mixtures with a weakly retarding gas such as CH_4 as described in **10.4**.

The discussion on the basis of Eq. (10.1) should be realized macroscopically in swarm parameters. The equation t_i can be also expressed as

$$1/(pt_i) = w_m \alpha_m/p \quad \text{for} \quad \eta_m = 0 \tag{10.2}$$

where the index m is referred to mixture. Data on w_m and α_m/p for some mixtures have been determined either experimentally or by the Boltzmann equation analysis. On the other hand, as a first approximation, the average electron method[106] has been proposed to estimate w_m. When values of w and ε_k are known as function of E/p for two gases 1 and 2 respectively, the value of w_m at $E/p = z_m$ is given by

$$w_m z_m = x w_1 z_1 + (1-x) w_2 z_2 \tag{10.3}$$

and

$$z_m = x z_1 + (1+x) z_2 \tag{10.4}$$

where z_1 and z_2 are the value of E/p giving the same ε_k for respective gases and w_1 and w_2 are the values at these z's for both the gases. The value of α_m/p at z_m is similarly estimated by

$$\frac{\alpha_m}{p} = x \frac{\alpha_1}{p} + (1-x) \frac{\alpha_2}{p} \tag{10.5}$$

where α_1 and α_2 are the value at z_1 and z_2 for respective gases for Eq. (10.3). It is assumed for the average electron method that $F(\varepsilon)$ is the same among gases 1 and 2 and the mixture.

Values of pt_i given by $p/(w_m \alpha_m)$ from these mthods are in a function of not p but E/p. The value increases with decreasing E/p which decreases with increasing p and also with the lapse of time even at the same pressure as shown in **7.1**. Therefore, since D_{obs} is integrated over the whole pulse duration, D_{obs} increases more effectively with increasing pressure than pt_i with decreasing E/p. As compared at the same pressure, the increment of D_{obs} for a mixture from for a pure host gas becomes larger than pt_i shown as a function of E/p. Furthermore, the $D_{obs}(p)$ curve becomes steeper than the curve expected from the $pt_i - E/p$ curve due to the variation of ε_b with the self-focusing in Eq. (2.26) as discussed in **7.2.1**.

In conclusion, it should be noticed that the parameters for t_i are in functions of E/p for which p is not the partial pressure of an additive but the total pressure even if some correction is needed for it. As will be described in **10.4**, the effect of SF_6 on D_{obs} for SF_6/Ar appears from the pressure lower than the pressure expected from its partial pressure. Such an effect is due to such a E/p related to total pressure.

The rate constants of Penning and associative ionizations are on the order of 10^{-11} — 10^{-9} cm³/s[107]. Even if the rate constant is overestimated to be 10^{-9} cm³/s and the excited rare gas atoms are produced in the same yield as the ions, for the case of $(1-x) = 0.1$, the quantity of the secondary electrons produced by such ionizations is estimated to be at largest one-tenth of that produced by the direct and secondary ionizations for the ns pulse duration. This estimation is based on the computational result on CH_4 ionization (**Fig. 9.6**), where the dimer

ions are presumed to be formed with the rate constant of 10^{-9} cm^3/s and $x = 1.0$ (pure methane). In addition, and additives may make the yield of the excited rare-gas atoms reduce substantially because of the retardation of secondary electrons. Thus, Penning or associative ionizations are concluded hardly to affect the ionization in the present study of the ns pulse duration.

10.3 He Mixtures

10.3.1 Experimental results

Values of D_{obs} for He mixtures containing N_2, O_2, N_2O, CH_4, C_2H_4, and SF_6 ($x = 0.9$) respectively are shown as functions of total pressure in **Fig. 10.1**. The D_{obs} increases in the order

$$N_2 > N_2O, C_2H_4, SF_6 > O_2, CH_4.\qquad\qquad(10.6)$$

When this order is compared with the curve in pure gases in **Fig. 8.15**, the self-focusing is remarkably enhanced by addition of N_2. The relationship of D_{obs} among gases except N_2 is almost the same between the pure gases and the mixtures, though data in the mixtures are rather scattered. Decreasing of D_{obs} above 250 Torr is mainly attributed to multiple scattering of the primary beam by a background gas.

10.3.2 Discussion

Data on σ_i and IP for lower-energy electrons are shown in **Fig. 8.22**. The profile of $F(\epsilon)$ can be presumed qualitatively from the $Q_t f - \bar{\epsilon}$ curve in **Fig. 8.19** as described already. Since He has the much higher IP and the much smaller σ_i and $Q_t f$ relatively to polyatomic gases, as described for Eq. (10.1) in **10.2**, the contribution of He to t_i is generally much smaller than
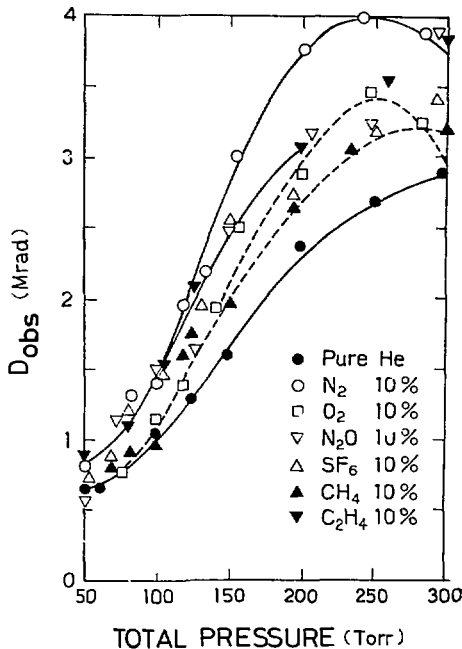
Fig. 10.1   Data on D_{obs} plotted against total pressure for He mixtures containing additives by 10%.
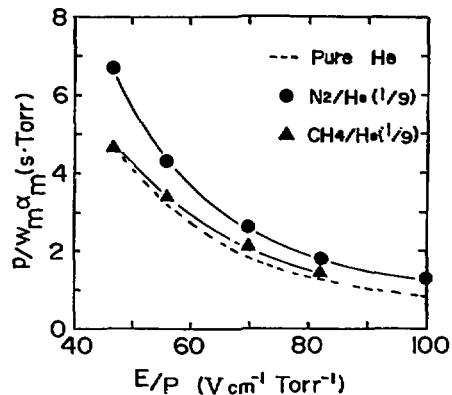
Fig. 10.2   Values of p $(w_m \alpha_m)$ estimated by the average electron method for N_2/He (1/9) and CH_4/He (1/9).

that of the additive. Then, the effect of these additives except N$_2$ can be interpreted in terms of the properties of the additives as described in **8.2.4** and **8.2.5**. The curve of D_{obs} for pure C$_2$H$_4$ is almost the same with that for CH$_4$ as seen in **Figs. 3.11** and **3.12**, while the curve for C$_2$H$_4$/He is rather higher than for CH$_4$/He. This may be due to the reduction of ϵ by C$_2$H$_4$ more effectively than by CH$_4$ because of the special dependence of $\bar{\epsilon}$ on E/p for CH$_4$ as described in **9.1.1**.

In **Fig. 10.1**, the increasing D_{obs} is strongly enhanced by addition of N$_2$. In **Fig. 8.22**, N$_2$ has the high IP and the small σ_i as compared with other additives. Furthermore, N$_2$ makes $\bar{\epsilon}$ reduce effectively as seen as the $Q_i f$ curve in **Fig. 8.19**. Then, in Eq. (10.1), the value of the second integral for N$_2$ is also small as well as of the first integral for He so that the value of t_i is much lengthened by addition of N$_2$. This fact indicates that the self-focusing in He is strongly enhanced by addition of a gas having high IP, small σ_i, and the strong effect on $F(\epsilon)$. Haydon and McIntosh[108] have reported that α_m/p for N$_2$/He increases by about 10% at E/p between 17 and 400 Vcm^{-1}Torr^{-1}. Although their data seems to be inconsistent with the above discussion, their data contain the contribution of the Penning ionization which can be neglected for the present study.

We attempted to estimate values of w_m and α_m/p by using Eqs. (10.3), (10.4), and (10.5) from data for pure gases cited already. As compared with pure He, the values of w_m descrease considerably for N$_2$/He (1/9) and CH$_4$/He (1/9), while the value of α_m/p for CH$_4$/He increases appreciably and that for N$_2$/He decreases only a little. Then, the values of $p/(w_m\alpha_m)$ vary with E/p as shown in **Fig. 10.2**. The curves indicate that, from Eq. (10.2), the value of pt_i increases by addition of N$_2$ while the value is hardly affected by CH$_4$. Then, as considering the relationship between the pt_i–E/p and D_{obs}–p curves as pointed out in **10.2**, the D_{obs}–p curve for the mixtures should be more separated from the curve for pure He. Consequently, the curve of pt_i for He mixtures estimated by means of the average electron method represents fairly well the aspect of the $D_{obs}(p)$ curve.

According to the Boltzmann equation analysis with the assumption of no Penning ionization for SF$_6$/He (1/9)[109], the value of w_m at E/p of 100 Vcm^{-1}Torr^{-1} is by 25% smaller than for pure He and the value of α_m/p at the same E/p is by 35% larger than for pure He. Morruzi and Craggs[110] have reported that the value of α_m/p for SF$_6$/He (13/87) decreases by about 20% at E/p between 14 and 32 Vcm^{-1}Torr^{-1}. These data suggest that the value of pt_i, given by $p/(w_m\alpha_m)$, in SF$_6$/He is almost the same with that in pure He at E/p of 100 Vcm^{-1}Torr^{-1}, while this value becomes much larger at lower E/p than that in pure He. On the other hand, in **Fig. 7.4**, E/p in pure He is less than 100 Vcm^{-1}Torr^{-1} for the major part of the pulse duration at pressures high than 50 Torr. Then, the effect of SF$_6$ in **Fig. 10.1** is attributed to such a lengthened t_i by addition of SF$_6$. The value of $\bar{\epsilon}$ in the mixture at E/p of 100 Vcm^{-1}Torr^{-1} is estimated to be around 15 eV by means of the Boltzmann equation analysis[109]. Therefore, the large value of α_m/p at this E/p is attributed to the σ_i for SF$_6$ which is large for higher ϵ and decreases considerably for ϵ lower than 23 eV, so that the value of α_m/p decreases with decreasing E/p.

10.3.3 Conclusion

It is concluded from the above discussion that D_{obs} in He mixtures can be interpreted by Eq. (10.1) and that the discussion on the basis of Eq. (10.1) is also supported by data on swarm parameters in the mixtures obtained experimentally and theoretically. The self-focusing of the beam is strongly enhanced by addition of a gas having high IP, small σ_i, and large $Q_i f$ such as N$_2$. Since O$_2$ has small σ_i but low IP and small $Q_i f$, the effect of O$_2$ is weak as seen in **Fig. 10.1**.

10.4   Ar Mixtures

10.4.1   Experimental results

The effect of various additives in Ar on D_{obs} was studied as a function of total pressure of a constant-composition mixture for some compositions (1, 5, and 10%). Values of D_{obs} for Ar mixtures containing Xe, N_2, O_2, N_2O, CH_4, C_2H_4, and SF_6 by 10% respectively are shown in **Fig. 10.3**. It is noticed that D_{obs} increases steeply with increasing pressure from a certain pressure (the onset pressure) by addition of polyatomic gases in contrast with the case of He mixtures in which the effect of additives appears gradually from 50 Torr and that D_{obs} is decreased by addition of Xe. The onset pressures of the effect are listed in **Table 10.1** with data for the other compositions. Decreasing of D_{obs} with increasing pressure above 150 Torr is due to multiple scattering of the primary beam by a background gas.
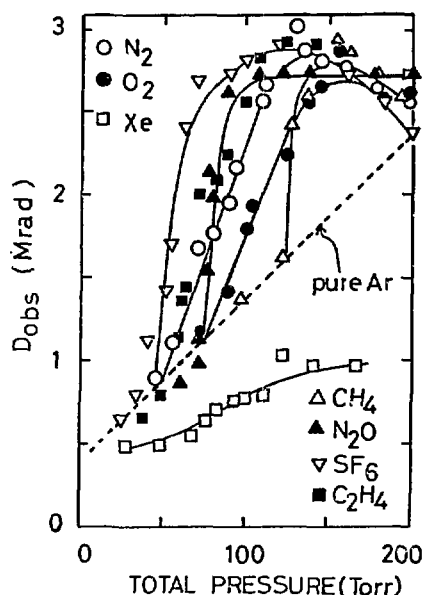
Fig. 10.3   Data on D_{obs} plotted against total pressure for Ar mixtures containing additives by 10%.

Table 10.1   Onset pressures (Torr)

Additives	Percentage in Ar mixture		
	1	5	10
CH_4	–	165	125
CH_3F	–	–	125
CCl_2F_2	130	70	55
CCl_3F	–	–	30
C_2H_6	–	140	95
C_2H_4	–	105	58
C_2H_2	–	120	60
N_2	–	–	50
NO	–	–	70
O_2	–	–	80
N_2O	110	95	75
SF_6	150	110	45

10.4.2   Discussion

As pointed out in **10.2**, $\bar{\varepsilon}$ in Ar is presumed not to be reduced from 9 eV down to E/p of a few $Vcm^{-1} Torr^{-1}$. Furthermore, as seen in **Fig. 8.22**, Ar has its IP and σ_i which are not so much different as He from most of the additives. Therefore, in Eq. (10.1), the relationship between the first and second terms is not so simple as for He mixtures. Therefore, the effect of additives must be mainly due to the shift of $F(\varepsilon)$ to the lower-ε side and or the electron-attachment process which is neglected for Eq. (10.1). In the following discussion, the additives are classified to (a) Xe by which D_{obs} is decreases, (b) CH_4 and CH_3F for which the onset pressure of the effect is the highest, (c) C_2H_6, C_2H_4, and C_2H_2 for which D_{obs} increases gradually with increasing pressure from the lower onset pressure, (d) N_2, NO, and O_2 for which D_{obs} increases gradually like (c), (e) N_2O and SF_6 for which D_{obs} increases steeply with increasing pressure and the effect of the electron attachment process is expected, and (f)

CCl_2F_2 and CCl_3F for which the situation is the same with (e).

a.   Xe

The decrease of D_{obs} by addition of Xe should be explained by the shortened t_i by means of Eq. (10.1). In **Fig. 8.22**, Xe has the lower IP and the larger σ_i than Ar so as for n_e to be increased. Furthermore, electron energies are not so reduced by Xe as by polyatomic gases for the ns pulse duration so that $F(\varepsilon)$ might not appreciably shift to the lower-ε side. Then, t_i is shortened as explained by Eq. (10.1).

b. CH_4 and CH_3F

As seen in **Fig. 10.4**, D_{obs} increases steeply with increasing pressure from 125 Torr in the presence of 10% CH_4 or CH_3F. This onset pressure is the highest in **Table 10.1**. In **Fig. 8.22**, CH_4 has the lower IP and the larger σ_i rather than Ar but not so much as Xe. Furthermore, according to data on $D_L/\mu^{46)}$, ε in CH_4 is presumed as Ar not to be reduced from 7.4 eV for E/p higher than 20 $Vcm^{-1}Torr^{-1}$. Most of E/p at pressures higher than 50 Torr of Ar lie in this E/p range higher than 20 $Vcm^{-1}Torr^{-1}$ in **Fig. 7.9**. Consequently, $\bar{\varepsilon}$ in the mixture is not reduced in the presence of the small amount of CH_4 for the major part of the pulse duration so that t_i may be shortened rather than lengthened due to the above IP and σ_i for CH_4. In fact, in **Fig. 10.4**, D_{obs} is rather smaller than for pure Ar at pressure lower than the onset pressure. Such a lower D_{obs} was found for most of Ar mixtures with additives having the lower IP and larger σ_i.

As increasing of the partial pressure of CH_4, some secondary electrons are retarded to an extent larger than in pure Ar due to the larger $Q_t f$ of CH_4 for $\bar{\varepsilon}$ above 7.4 eV as seen in **Fig. 9.19**. Once $F(\varepsilon)$ shifts appreciably to the lower-ε side so as to affect t_i, this retarding effect is proportional to the total pressure p or n_0 in Eq. (10.1) or (10.2). Therefore, the curve of D_{obs} rises steeply as seen in **Fig. 10.4** because of the high onset pressure. The value of
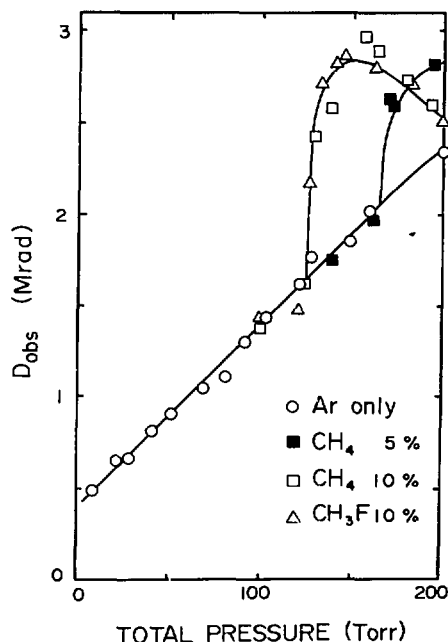
Fig. 10.4   Data on D_{obs} plotted against total pressure for CH_4/Ar (1/9) and (5/95) and CH_3F (1/9).

$p/(w_m \alpha_m)$ estimated by the average electron method is almost the same with that for pure Ar at E/p between 80 and 100 $Vcm^{-1} Torr^{-1}$.

As described in **9.2**, the behavior of CH_3F is almost the same with CH_4. In fact, in **Fig. 10.4**. The curve of D_{obs} for CH_3F is quite the same with for CH_4.

c. C_2H_6, C_2H_4, and C_2H_2

Data on D_{obs} for Ar mixtures with C_2H_6, C_2H_4, and C_2H_2 containing 5 and 10% respectively are shown in **Fig. 10.5**. The order of the onset pressure among CH_4, C_2H_6, C_2H_4, and C_2H_2 can be explained in terms of their properties as described in **9.1**, especially, by the shift of $F(\epsilon)$ to the lower-ϵ side. According to Yamane[105], the value of α_m/p for hydrocarbons/Ar at E/p between 5 and 35 $Vcm^{-1} Torr^{-1}$ increases by addition of the small amount of hydrocarbons while decreases with increasing the amount of hydrocarbons owing to decreasing $\bar{\epsilon}$. Although Heylen[111-114] had reported the data on α_m/p for hydrocarbons/Ar, their data contain the Penning-ionization processes which should be neglected for the present study.

The slope of the D_{obs} curve is slower for the lower onset pressure. Since the effect on $F(\epsilon)$ is in a function of E/p for which p is related to the total pressure as pointed out in **10.2**, the effect of additives on $D_{obs}(p)$ appears more abruptly for the mixture giving the higher onset pressure as described for CH_4/Ar.
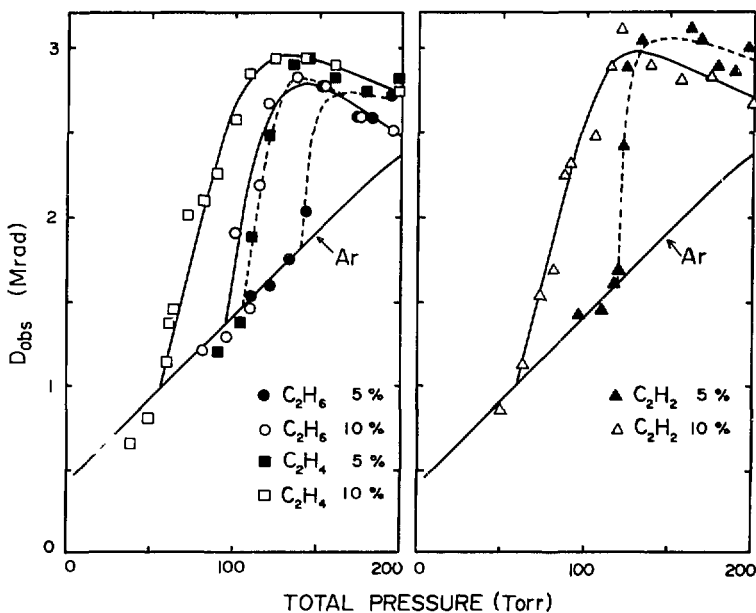
Fig. 10.5   Data on D_{obs} plotted against total pressure for Ar mixtures containing C_2H_6, C_2H_4, C_2H_2 by 5 and 10% respectively.

d. O_2, NO, and N_2

The onset pressure for O_2/Ar (1/9) is fairly high in **Table 10.1** and the slope of the D_{obs} curve in **Fig. 10.3** relatively slow. These facts are attributed to the lower IP, the smaller σ_i, and the smaller $Q_t f$ for O_2; the effect of the smaller σ_i is cancelled by the lower IP and the smaller $Q_t f$. The value of t_i lengthened by addition of O_2 is supported by the Boltzmann equation analysis on O_2/Ar (1/9)[55]. According to this analysis, the value of $p/(w_m \alpha_m)$ increases gradually more than for pure Ar with decreasing E/p from 100 $Vcm^{-1} Torr^{-1}$ and the incre-

ment for the mixture becomes about 10% at E/p around 60 Vcm^{-1} Torr^{-1} and, furthermore, 50% at E/p around 30 Vcm^{-1} Torr^{-1}.

In **Fig. 8.22**, N$_2$ has the same *IP* with Ar and the σ_i smaller than Ar and furthermore, in **Fig. 8.19**, N$_2$ has the large $Q_t f$. The onset pressure for N$_2$/Ar lower than for O$_2$/Ar can be explained in terms of these properties of N$_2$. However, the value of $p/(w_m \alpha_m)$ estimated by the average electron method does not show such a difference between pure Ar and N$_2$/Ar (1/9).

The curve of D_{obs} for NO/Ar (1/9) lies between the curves for N$_2$/Ar (1/9) and O$_2$/Ar (1/9) in **Fig. 10.3**: In **Fig. 8.22**, NO has the lower *IP* and the larger σ_t than N$_2$ and O$_2$. The electron-attachment cross section for NO is almost the same with for O$_2$[51]. On the other hand, NO has the high peak of Q_t around 1 eV[56].

e.   N$_2$O and SF$_6$

Data on D_{obs} for N$_2$O/Ar and SF$_6$/Ar are shown in **Figs. 10.6** and **10.7** respectively. As seen in **Fig. 10.3**, the slope of the curve is much steeper than for N$_2$/Ar and O$_2$/Ar. It must be remembered that, as described in **8.2.3**, N$_2$O and SF$_6$ have the large possibility of the effects of $Q_t f$ and the electron-attachment process.

In **Fig. 8.22**, *IP* for N$_2$O is almost the same with O$_2$ and CH$_4$ but σ_t for N$_2$O is twice as large as for O$_2$ at ϵ lower than *IP* for Ar. On the other hand, the value of Q_t[56] is larger than N$_2$ for ϵ around 20 eV and has the high peak around 3 eV like N$_2$ as shown in **Fig. 8.19**. The onset pressure for N$_2$O/Ar higher than for N$_2$/Ar despite of such a Q_t for N$_2$O may be due to the larger σ_i of N$_2$O. However, once the effect of the shift of $F(\epsilon)$ on t_t appears appreciably, this effect is superposed on the effect of the electron attachment process around 2.3 eV so that D_{obs} increases steeply with increasing pressure. The onset pressure for N$_2$O/Ar (1/9) is about ten times as large as the pressure at which D_{obs} begins to increase with increasing pressure in pure N$_2$O. However, the onset pressure for the 1 and 5% mixtures are not so different
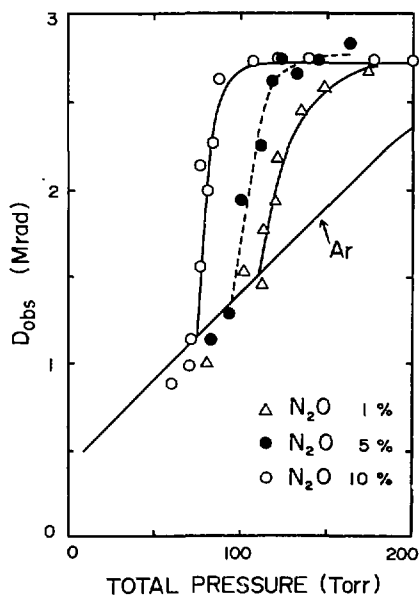
Fig. 10.6   Data on D_{obs} plotted against total pressure for N$_2$O/Ar (1/9), (5/95), and (1/99).

Fig. 10.7   Data on D_{obs} plotted against total pressure for SF$_6$/Ar (1/9), (5/95), and (1/99).

as the difference of the N_2O mole fraction. This may be due to the effect on $F(\epsilon)$ closely connected with the total pressure.

In **Fig. 8.22**, IP for SF_6 is higher than for N_2O and almost the same with N_2 and Ar and also σ_i for SF_6 at ϵ below 23 eV is smaller than for Ar and N_2O. These data for SF_6 suggest that t_i may be lengthened by additi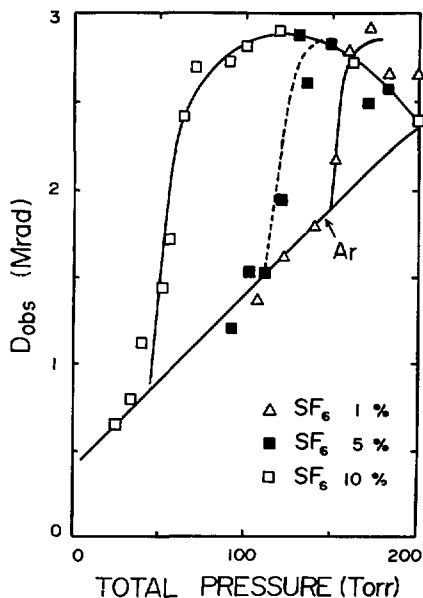on of SF_6 as shown by Eq. (10.1) when $F(\epsilon)$ is affected and some of secondary electrons are lost by the electron-attachment process in the presence of the small amount of SF_6 as described in **8.2.3**. The electron-attachment process to SF_6 is known for electrons around 0.4 eV to give efficiently SF_5^-, as well as for thermal electrons. The amount of SF_6 at the onset pressures for the 1, 5, and 10% mixtures seems to be too small relatively to the pressure at which D_{obs} begins to increase with increasing pressure in pure SF_6. This discrepancy can be understood by the effect of E/p on $F(\epsilon)$ for which p is not simply the partial pressure but related to the total pressure. The onset pressure for SF_6/Ar is much dependent on the mole fraction of SF_6 in contrast with N_2O/Ar. The onset pressure for SF_6/Ar lower than for N_2O/Ar, despite of the lower resonance energy of the electron-attachment process (0.4 eV), may be due to the small σ_i for SF_6. The effect of the electron-attachment process is proportional to the total density of secondary electrons so that the effect might appear even in the presence of the small amount of SF_6 at higher total pressure. The difference of the mole-fraction dependence on the onset pressure may suggest that the shift of $F(\epsilon)$ is mainly affected for N_2O/Ar and the electron-attachment process does so for $S \cdot_{\epsilon}/Ar$.

f. CCl_2F_2 and CCl_3F

Data on D_{obs} for CCl_2F_2/Ar and CCl_3F/Ar are shown as functions of total pressure in **Fig. 10.8**. As described in **9.3**, the value of Q_i increases considerably with increasing Cl atom and the electron-attachment process for both the gases has the large cross section at the resonance energy higher than for SF_6. The curves in **Fig. 10.8** can be explained in terms of these properties.

10.4.3 Conclusion

The increase of D_{obs} by addition of polyatomic gases can be explained by the lengthened t_i which can be estimated qualitatively by using Eq. (10.1). This effect is enhanced by a gas having the higher IP and the smaller σ_i. However, this effect is mainly determined by $F(\epsilon)$ The value of D_{obs} is increased from lower pressure by addition of a gas which retards secondary electrons more strongly. Furthermore, when the electron-attachment process neglected in Eq. (10.1) occurs for secondary electrons with higher energy, D_{obs} is steeply increased with increasing pressure. The discussion on the basis of Eq. (10.1) is demonstrated for some cases by swarm parameters obtained experimentally or theoretically but the average electron method was useful only for He mixtures.

10.5 O_2 Mixtures

In **Fig. 10.9**, values of D_{obs} for N_2/O_2 (1/9) and SF_6/O_2 (1/9) are plotted by closed marks as functions of total pressure with those for pure O_2, N_2, and SF_6 by open marks. The curve for the mixtures shifts from the curve for pure O_2 to that for pure N_2 or SF_6; suddenly at 50 Torr for N_2/O_2 and rather mildy from 20 Torr for SF_6/O_2.

As pointed out already, D_{obs} is affected strongly by addition of N_2 to He and Ar. The effect of N_2 for O_2 can be explained similarly with that for He and Ar mixtures. This effect appears only from 50 Torr which is the same with the onset pressure for N_2/Ar (1/9). The difference of the effect between N_2 and SF_6 can be explained similarly with their effects on

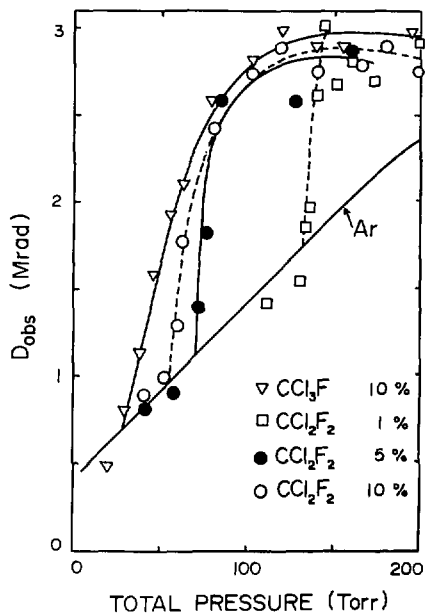the Ar mixtures.

Fig. 10.8   Data on D_{obs} plotted against total pressure for CCl_3F (1/9) and CCl_2F_2 (1/9), (5/95), and (1/99).
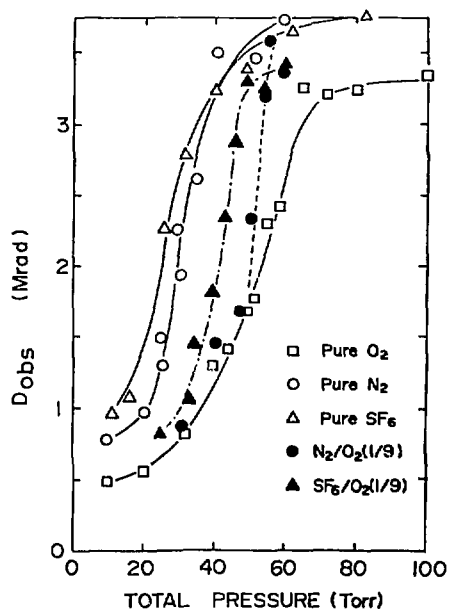
Fig. 10.9   Data on D_{obs} plotted against total pressure for N_2/O_2(1/9) and SF_6/O_2 (1/9).

11. Multiple Scattering of Beam

11.1 Multiple Scattering

Electrons passing through matter lose energy by inelastic collisions and deflect from their original course by scattering. The deflection is due to elastic collisions with atomic nuclei. Inelastic collisions result mainly in the energy loss but hardly in the deflection. Spencer had discussed the influence of inelastic collisions as a correction factor for elastic collisions[115].

When the scattering layer is very thin, that is, $d < 1/\sigma_s N$ (σ_s = the scattering cross section and N = the number density of scattering atoms), all the electrons are scattered by a single nucleus. The theory of this single scattering has been developed by some investigators[116-118].

When electrons are scattered by times more than about 20 in the layer, this is termed by multiple scattering. The angular distribution of the scattered electrons is approximately Gaussian when the mean scattering angle $\bar{\theta}$ is smaller than about 20°. The simple theory of multiple scattering has been given by Williams[119], assuming that energy losses in a scattering medium can be neglected. From the theory of errors, the statistical angular distribution of the deflection is approximately given by

$$P(\theta)\,d\theta \cdot \frac{2\theta}{\bar{\theta}^2}\exp\left(\frac{\theta^2}{\bar{\theta}^2}\right)d\theta \qquad (11.1)$$

where $\bar{\theta}^2$ (rad^2) is the mean squared scattering angle. According to Williams, $\bar{\theta}^2$ is given by

$$\theta^2 = 0.601 \cdot \frac{z(z+1)d}{A}\left\{\frac{\tau+1}{\tau(\tau+2)}\right\}^2 \cdot \ln\left[1.13 \times 10^4 \frac{z^{\frac{1}{3}}(z+1)(\tau+1)^2}{A\tau(\tau+2)}\,d\right] \qquad (11.2)$$

where Z is the atomic number of the scattering medium, A the atomic weight, d the total thickness (g/cm^2), and τ the electron kinetic energy in unit of rest mass; therefore, roughly

$$\bar{\theta}^2 \propto \frac{Z(Z+1)d}{A\tau^2} \qquad (11.3)$$

Consider a parallel and infinitely narrow beam incident upon a gaseous medium, assuming that the thickness of the medium is sufficiently thin so that the energy loss of incident electrons can be neglected. The distribution of electrons in radial distance r from the axis after traverse of a thickness d of the scattering medium is Gaussian. The mean squared value of r is given by [120]

$$\bar{r}^2 = \frac{\bar{\theta}^2 d^2}{3} \qquad (11.4)$$

The flux density ϕ on the beam axis is inversely proportional to $\bar{r}^2$. Therefore, we can obtain the relation for polyatomic gases like

$$\frac{1}{\phi} \propto \frac{\bar{Z}(\bar{Z}+1)Mp}{\bar{A}} \qquad (11.5)$$

with $\bar{Z} = \sum w_i Z_i$ and $\bar{A} = \sum w_i A_i$, where M is the molecular weight of the gas, p the gas pressure, and for the ith element in the gas, Z_i is its atomic number, A_i its atomic weight, and w_i its weight fraction. More strict theoretical treatment of multiple scattering has been developed by Goudsmit and Saunderson[121] and Molierè[122].

11.2 Comparison with Data on D_{obs}

Although the primary beam used in the present study did not always satisfy the assumptions leading to equation (11.5), data on the maximum value of the depth-dose curve (D_{obs}) at various pressures shown in **2.4** are plotted as functions of $\bar{Z}(\bar{Z}+1)M/\bar{A}$ in **Fig. 11.1**. The isobar curves in **Fig. 11.1** are drawn to fit with the observed points as many as possible in the low-$\bar{Z}$ region and to fall in inverse proportion at high-$\bar{Z}$. Generally speaking, the slope of the isobar curve is more gentle for low-$\bar{Z}$ and steeper for high-$\bar{Z}$ than inversely proportional. The value of D_{obs} decreases inversely proportionally with increasing $\bar{Z}(\bar{Z}+1)M/\bar{A}$ from the lower-$\bar{Z}$ region at higher pressure as suggesting that D_{obs} is roughly proportional to ϕ.

The beam is defocused at higher pressure as a result of competition between the self-focusing force and the diffusion by multiple scattering. Since f_e becomes unity at the very early stage of the pulse duration at higher pressure, D_{obs} is related by Eq. (2.26) to I_{net} which is proportional to the self-focusing force by Eq. (2.27). The value of I_{net} is computed as a function of time for the various pressure of some gases in **6. — 9.**. This analysis shows that I_{net} increases with increasing pressure in the pressure range as shown in **Fig. 11.1**. Then, the inversely proportional decrease of D_{obs} at higher pressure is mainly due to multiple scattering of the primary beam by the background gas.
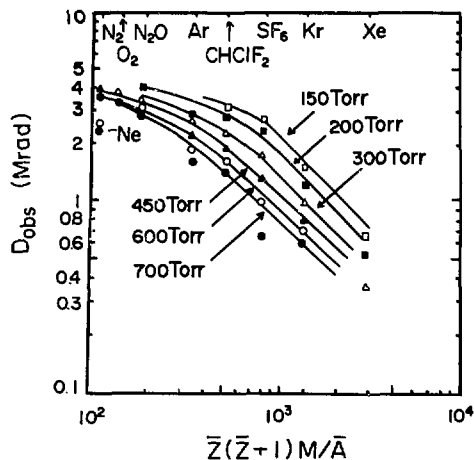

Fig. 11.1   Data on D_{obs} plotted against $Z(Z+1)M/A$ for various pressures; 150 Torr (□), 200 Torr (■), 300 Torr (△), 450 Torr (▲), 600 Torr (○), and 700 Torr (●).

12. Summary

12.1 General Conclusions

An aluminum-blue-cellophane stack was used as a dosimeter to measure the degree of the self-focusing. The depth-dose distributions in this dosimeter were measured at first in helium as a function of pressure p at various positions to see the variation of electron energy spectrum with the position as well as with p (Chap. 4). Afterwards, the maximum dose of the depth-dose curve, D_{obs}, in the dosimeter on the beam axis at 10.4 cm from the irradiation cell window was measured as a function of p for various gases. In low-pressure gases, D_{obs} increases abruptly and almost linearly with increasing p due to the space-charge neutralization by direct ionization. Therefore, the relative total ionization cross section of gases for the primary beam could be obtained from the data in this region (Chap. 5). As seen in **Fig. 3.5 – 3.13**, after passing the maximum (usually 1 – 3 Torr), D_{obs} decreases abruptly with slightly increasing p due to electron avalanching by an electric field E_z induced by the pulsed beam. After passing the minimum, D_{obs} increases again gradually with further increasing p due to the suppression of electron avalanching as a result of decreasing E_z/p. At higher pressure, (above 100 Torr), the beam is diverged due to multiple scattering by a background gas (Chap. 11).

The value of D_{obs} is related to the net current I_{net} at higher pressure like

Eq. (2.26): $$D_{obs} \propto \int \frac{I_b(t) I_{net}(t) \beta^2}{\varepsilon_b^2} \, dt$$

where $\pi \varepsilon_b$ is the beam emittance. The net current is the sum of the beam current I_b and the backward plasma current I_{back} induced by E_z;

Eq. (2.19): $$I_{net} = I_b + I_{back}$$

The self-focusing force is proportional to I_{net} (Eq. (2.27)).

When the value of $I_{net}(t)$ is estimated from molecular data for gases, our data on D_{obs} can be analyzed physicochemically. For this purpose, we assumed that

Eq. (6.2): $$I_{back} = \pi r_0^2 E_z(t) \sigma_e(t)$$

Eq. (6.4): $$E_z = 0.93 \, c_1 \frac{dI_{net}(t)}{dt}$$

Eq. (6.10): $$\sigma_e = 1.43 \times 10^{-28} \frac{n_e(t)}{p(\text{Torr}) Q_m \bar{\varepsilon}(\text{eV})^{0.5}}$$

Eq. (6.12): $$\bar{\varepsilon} = \frac{3e D_L}{2\mu}$$

Eq. (6.16): $$\frac{dn_e}{dt} = \frac{n_0 \sigma_{ion}(E_b) I_b(t)}{\pi r_0^2 e} + \frac{n_e(t)}{t_i(t)} - \alpha_r n_e n_i - \alpha_{re} n_e n_d$$

Eq. (6.15): $$p t_i = \frac{1}{w(\alpha_T/p - \eta_T/p)}$$

where c_1 is a constant defined in Eq. (6.1), σ_e the plasma conductivity, Q_m the momentum transfer cross section, $\bar{\varepsilon}$ the mean energy of secondary electrons estimated from D_L/μ by Eq. (6.12), n_e the number density of secondary electrons calculated by Eq. (6.16), and t_i the mean ionization time estimated by Eq. (6.15) in which w is the electron drift velocity, α_T the first Townsend ionization coefficient, and η_T the electron attachment coefficient. The explanation of symbols of Eq. (6.16) is given in text.

The value of $I_{net}(t)$ for He, Ar, H_2, N_2, and CH_4 was calculated self-consistently for various pressures on the basis of the above scheme. The calculated values of I_{net} could express fairly well the aspect of D_{obs} for these gases according to Eq. (2.26) (**Figs. 7.2** and **8.12**). Therefore, we can say that values of parameters obtained by the present computation can be used fairly quantitatively as data for the phenomena occuring in the drift channel of the pulsed beam, which are not easy to be measured directly. The present numerical analysis gives the following conclusions. The value of $I_{net}(t)$ is nearly constant after a certain time (t_B) up to pressure at which $D_{obs}(p)$ is the minimum, as assumed for the t_B model (**2.2.1**), but increases gradually with the lapse of time at higher pressure. The larger D_{obs} is given by the smaller I_{back} which is proportional to the product of $n_e/Q_m \bar{\varepsilon}^{0.5}$ and E_z/p. When the variation of $Q_m \bar{\varepsilon}^{0.5}$ is neglected among gases, the larger D_{obs} is given by the larger t_i which is related to molecular data by Eq. (6.15). The value of E_z/p decreases with the lapse of time and also with decreasing p. Most of E_z/p are lower than 100 $Vcm^{-1} Torr^{-1}$ for the major part of the pulse duration in the pressure region at which D_{obs} increases gradually with increasing pressure.

The major part of secondary electrons are produced by direct ionization due to the beam at low pressure but, after passing the maximum D_{obs} at low pressure, by secondary ionization due to secondary electrons accelerated by E_z. The value of n_e increases with the lapse of time and becomes the plateau value at about 3 ns. This plateau value is almost the same for all the gases at pressures at which D_{obs} is higher than 1 Mrad. Since this plateau value is on the order of $10^{15} cm^{-3}$, the electron-ion recombination, Penning ionization, and charge transfer processes can be neglected for the ns pulse duration because of the slow rate of these processes.

12.2 Effect of Respective Gases on Ionization

The larger D_{obs} is given by the longer t_i, which is estimated by Eq. (6.15), in the beam-drift channel. For a gas with no appreciable electron-attachment process, Eq. (6.15) is re-written as

Eq. (7.3): $$\frac{1}{n_0 t_i} = \left(\frac{2}{m_e}\right)^{\frac{1}{2}} \int_{IP}^{\infty} \varepsilon^{\frac{1}{2}} \sigma_i(\varepsilon) F(\varepsilon) d\varepsilon$$

where n_0 is the number density of gas molecules, m_e the electronic rest mass, IP the ionization potential of a gas, $\sigma_i(\varepsilon)$ the total ionization cross section for secondary electrons with energy ε, and $F(\varepsilon)$ the distribution function of ε. The aspect of our data on D_{obs} for various gases could be interpreted in terms of swarm parameters by Eq. (6.15) and also in terms of molecular data by Eq. (7.3) except for CH_4 which has the large $Q_m \bar{\varepsilon}^{0.5}$ in Eq. (6.10) relatively to other gases. In Eq. (6.15), the term of η_T can be neglected except for SF_6 and $CCl_2 F_2$.

Generally speaking, when the form of $F(\varepsilon)$ is presumed qualitatively by $Q_t f$ (Q_t: the total collision cross section and f: the mean fractional energy loss per collision to be proportional to w^2/k_T (the Townsend energy factor)), in Eq. (7.3), $F(\varepsilon)$ plays an important role to determine t_i, rather than IP and σ_i. Therefore, the gas with the larger $Q_t f$ gives the larger D_{obs} in the intermediate pressure region (10 − 100 Torr). Especially, N_2 has the large $Q_t f$ in addition to the higher IP and the smaller σ_i, while O_2 has the small $Q_t f$, the lower IP and the smaller σ_i so that D_{obs} for N_2 is much larger than for O_2 (**Fig. 8.15**). Since $N_2 O$ has the high peak of $Q_t f$ for ε around 3 eV and some effect of the electron attachment, D_{obs} for $N_2 O$ is larger in spite of the lower IP and the larger σ_i than for N_2. The large D_{obs} for SF_6 at lower pressure around 20 Torr is attributed to the higher IP, the smaller σ_i and the large cross section of the electron attachment process. The value of D_{obs} for $CCl_2 F_2$ at this lower pressure is larger than for SF_6. This is due to the large cross section of the electron attachment process around 1 eV for $CCl_2 F_2$ and the large Q_t for Cl because this resonance energy is higher than

for SF_6 (0.4 eV) and Q_t is larger for Cl than for F.

The value of D_{obs} at $10 - 100$ Torr was relatively small in He, Ar, and O_2 as compared with other gases. When polyatomic gases were added to these gases, the increase of D_{obs} with pressure was enhanced so that the beam was self-focused more strongly by the addition. For a binary mixture with no appreciable electron-attachment and Penning-ionization processes, Eq. (7.3) is rewritten approximately as

Eq. (10.1): $$\frac{1}{n_0 t_i} = \left(\frac{2}{m_e}\right)^{\frac{1}{2}} \left[\int_{IP_1}^{\infty} x \, \varepsilon^{\frac{1}{2}} \sigma_{i1}(\varepsilon) F(\varepsilon) d\varepsilon \right.$$
$$\left. + \int_{IP_2}^{\infty} (1 - x) \varepsilon^{\frac{1}{2}} \sigma_{i2}(\varepsilon) F(\varepsilon) d\varepsilon \right]$$

where x is the mole fraction of a host gas 1 and the index 2 is referred to an additive gas. Although the related data are sparse for these mixtures, our data on D_{obs} for them can be interpreted on the basis of Eq. (10.1). Data on related swarm parameters for some of them are also consistent with Eq. (10.1).

For He mixtures ($x = 0.9$ for He), the effect appeared gradually with increasing total pressure between 100 and 200 Torr. The self-focusing is remarkably enhanced by addition of N_2. For other gases, the order of the effect is the same with that of D_{obs} for pure additive gases. Since He has the highest IP and the smallest σ_i, in Eq. (10.1), the contribution of the first term for He to t_i can be neglected against that of the second term for additives which have low IP, large σ_i, and also large $Q_i f$ because of the large shift of $F(\varepsilon)$ to the lower-ε side. Therefore, the effect of such additives can be interpreted in light of the data of D_{obs} in pure gases. When the additive has higher IP, smaller σ_i, and larger $Q_i f$ like N_2, the effect on D_{obs} appears very strongly.

For Ar mixtures ($x = 0.90 - 0.99$ for Ar), D_{obs} increased steeply with increasing pressure from a certain pressure by addition of polyatomic gases; this onset pressure for $(1-x) = 0.1$ was the highest for CH_4 (125 Torr) and the lowest for $CCl_3 F$ (30 Torr). Since Ar has IP and σ_i not so different from most of polyatomic gases as He, the relationship between the first and second terms in Eq. (10.1) is not so simple for He mixtures. It is presumed from data on D_L/μ that ε is hardly reduced during the pulse in Ar and, furthermore, Ar has the fairly large σ_i. Therefore, the effect can appear only in the mixture containing additives more than the critical amount. Since CH_4 has the similar dependence of ε on D_L/μ with Ar, the effect does not appear up to the highest pressure.

The present study gives many useful informations for ionization of gases under electric field induced by the pulsed electron beam. The informations are related to the behavior of gases in a ionization chamber, the discharge inhibition, and the precursor of laser produced by the pulsed beam.

References

1) Hotta H., Tanaka R., Sunaga H., Washino M., Sugiura T. and Suzuki N.: JAERI-M5775, "Characteristics of the Pulsed Electron Beam from Febetron 706" (1974) [in Japanese].
2) Tanaka R., Sunaga H. and Hotta H.: Radiat. Res., **63**, 14, (1975).
3) Hotta H., Tanaka R., Sunaga H. and Arai H.: ibid., **63**, 24, (1975).
4) Hotta H., Tanaka R. and Arai H.: ibid., **63**, 32 (1975).
5) Arai H. and Hotta H.: ibid., **64**, 407 (1975).
6) Arai H. and Hotta H.: Radiat. Phys. Chem., **10**, 7 (1977).
7) Link W.T.: IEEE Trans. Nucl. Sci., **NS-14**, 777 (1967).
8) Hotta H. and Arai H.: J. Chem. Phys., **67**, 3608 (1977).
9) Arai H. and Hotta H.: Radiat. Res., **77**, 405 (1979).
10) Arai H. and Hotta H.: J. Chem. Phys., **75**, 2252 (1981).
11) Arai H. and Hotta H.: ibid., **75**, 2723 (1981).
12) Arai H. and Hotta H.: ibid., **75**, 3876 (1981).
13) Yonas G. and Toepfer A.J.: "Gaseous Electronics", ed. Hirsh M.N. and Oskam H.J., Acad. Press, New York, Vol. 1, Chap. 6 (1978).
14) Swain D.W.: J. Appl. Phys., **43**, 396 (1972).
15) McArthur D.A. and Poukey J.W.: Phys. Rev. Lett., **27**, 1765 (1971).
16) McArthur D.A. and Poukey J.W.: Phys. Fluids, **16**, 1996 (1973).
17) Miller P.A., Gerardo J.B. and Poukey J.W.: J. Appl. Phys., **43**, 3001 (1972).
18) Miller P.A. and Geraido J.B.: ibid., **43**, 3008 (1972).
19) Wallace S.C. and Kenney-Wallace G.A.: Int. J. Radiat. Phys. Chem., **7**, 345 (1975).
20) Sauer M.C., Jr.: Adv. Radiat. Chem., **5**, 98 (1976).
21) Rhodes Ch. K.: "Topics in Applied Physics vol. 30, Excimer Lasers", Springer-Verlag, Berlin (1979).
22) Ono K.: Jpn J. Appl. Phys., **19**, 1515 (1980).
23) Willis C., Boyd A.W. and Miller O.A.: Radiat. Res., **46**, 428 (1971).
24) Bennett W.H.: Phys. Rev., **45**, 890 (1934).
25) Lawson J.D.: J. Electron. Contr., **5**, 146 (1958).
26) Putnam S.: Phys. Intern. Comp. Report PIFR-72-105, "Theoretical Studies of Intense Relativistic Electron Beam-Plasma Interactions", California (1971).
27) Yonas G., Spence P., Ecker B. and Rander J.: DASA 2426, "Dynamic Effect of High ν/τ Beam Plasma Interactions" (1969).
28) Alfvén H.: Phys. Rev., **55**, 425 (1939).
29) Yonas G. and Spence P.: "Record of 10th Symposium on Electron, Ion, r .. Laser Beam Technology", ed. Martin L., San Francisco Press, 143 (1969).
30) Kapchinskij I.M. and Vladimirskij V.V.: "Proc. Int. Conf. on High-Energy Accelerators and Instrumentation", ed. Kowarski L., CERN, Scientific Inform. Service, Geneva, 274 (1959).
31) Garren A.A.: UCRL-19313, "Thin Lens Optics with Space Charge", Lawrence Berkeley Lavoratory, California (1969).
32) Graybill S.E. and Uglum J.R.: J. Appl. Phys., **41**, 236 (1970).
33) Olson C.L.: Phys. Fluids, **18**, 585 (1975).
34) Olson C L.: ibid., **18**, 598 (1975).
35) Ling C.C., Weiss H. and Epp E.R.: Radiat. Res., **56**, 307 (1973).
36) Rieke F.F. and Prepejchal W.: Phys. Rev. A **6**, 1507 (1972).
37) Olson C.L.: ibid., A **11**, 288 (1975).
38) Mitchner M. and Kruger C.H., Jr.: "Partially Ionized Gases", Wiley, New York (1973).
39) Spitzer L., Jr.: "Physics of Fully Ionized Gases", Interscience Tracts on Physics and Astronomy, John Wiley ans Sons, New York, 138 (1962).
40) Bell A.T.: "Techniques and Applications of Plasma Chemistry", John Wiley and Sons, New York, Chap. 1 (1974).
41) Dote T. and Shimada M.: J. Phys. Soc. Jpn, **49**, 1434 (1980).
42) Felsenthal P. and Proud J.M.: Phys. Rev., **139** A, 1976 (1965).
43) Good A.: Chem. Rev., **75**, 561 (1975).
44) Arai H.: JAERI-M9320, "Analysis of Gas Ionization by an Intense Pulsed Electron Beam" (1981) [in Japanese].
45) Kuo S.S.: "Computer Application of Numerical Methods", Addition-Wesley, U.S.A. (1972).
46) Lakshiminarashimha C.S. and Lucas J.: J. Phys. D **10**, 313 (1977).

47) Gilardini A.L.: "Low Energy Electron Collisions in Gases", Wiley, New York (1972).
48) Bates D.R., Kingston A.E. and McWhirter R.W.P.: Proc. Roy. Soc., A **267**, 297 (1962).
49) Bardsley J.N. and Biondi M.A.: Adv. Atomic and Molecular Physics, **6**, 1 (1970).
50) Dutton J.: J. Phys. Chem. Ref. Data, **4**, 577 (1975).
51) Christophorou L.G.: "Atomic and Molecular Radiation Physics", Wiley-Intersci., New York (1971).
52) Itikawa Y.: Atomic Data and Nucl. Data Tables, **14**, 1 (1974).
53) Rapp D. and Englander-Golden P.: J. Chem. Phys., **43**, 1464 (1965).
54) Garamoon A.A. and Ismail I.A.: J. Phys. D **10**, 991 (1977).
55) Matsushima H., Taniguchi T., Tagashira H. and Sakai Y.: Papers of Technical Group of Electric Discharges (IEE, Japan), ED-78-71 (1978) [in Japanese].
56) Landolt H.H., and Börnstein R.: "Zahlenwerte und Funktionen", Springer, Berlin, Vol. **1**, Part 1 (1956).
57) Rose D.J.: Phys. Rev., **104**, 273 (1956).
58) Kontoleon N., Lucas J. and Virr L.E.: J. Phys. D **5**, 956 (1972).
59) Auerbach D., Cacak R., Caudano R., Gaily T.D., Keyser C.J., McGowan J. Wm., Mitchell J.B.A. and Wilk S.F.J.: ibid., B **10**, 3797 (1977).
60) Haydon S.C. and Williams O.: ibid., D **9**, 523 (1976).
61) Kontoleon N., Lucas J. and Virr L.E.: ibid., D **6**, 1237 (1973).
62) Mul P. and McGowan J. Wm.: ibid., B **12**, 1591 (1979).
63) Mul P. and McGowan J. Wm.: Technical Report H-78-1 "Compilation of Data Relevant to Rare Gas-Rare Gas and Rare Gas-Monohalide Excimer Lasers", ed. McDaniel E.W., Flannery M.R., Ellis H.W. and Robert T.G., U.S. Army Missile Research and Development Command, Alabama 35809, Chap. 2 (1979).
64) Wilson D.E. and Armstrong D.A.: Can. J. Chem., **48**, 598 (1970).
65) Maier H.N. and Fessenden R.W.: J. Chem. Phys., **62**, 4790 (1975).
66) Warman J.M., Sennhauser E.S. and Armstrong D.A.: ibid., **70**, 995 (1979).
67) Srivastava S.K., Trajmar S., Chutjan A. and Williams W.: ibid., **64**, 2767 (1967).
68) Bhalla M.S. and Craggs J.D.: Proc. Phys. Soc., **80**, 151 (1962).
69) Harrison M.F.A. and Geballe R.: Phys. Rev., **91**, 1 (1953).
70) Dutton J., Harris F.M. and Hughes D.B.: J. Phys., B **8**, 313 (1975).
71) Conti V.J. and Williams W.: ibid., D **8**, 2198 (1975).
72) Asundi R.K. and Craggs J.D.: Proc. Phys. Soc., **83**, 611 (1964).
73) Dutton J., Harris F.M. and Hughes D.B.: Proc. IEE, **120**, 941 (1973).
74) Christophorou L.G.: Chem. Rev., **76**, 409 (1976).
75) Pejčev V.M., Kurepa M.V. and Čadež I.M.: Chem. Phys. Lett., **63**, 301 (1979).
76) Lucas J., Price D.A. and Moruzzi J.M.: J. Phys., D **6**, 1503 (1972).
77) Lakshiminarsasimha C.S., Lucas J. and Kontoleon N.: ibid., D **7**, 2545 (1974).
78) Naidu M.S. and Prasad A.N.: ibid., D **5**, 1090 (1972).
79) Naidu M.S. and Prasad A.N.: ibid., D **2**, 1431 (1969).
80) Christophorou L.G., Gant K.S. and Baird J.K.: Chem. Phys. Lett., **30**, 104 (1975).
81) Golden D.E., Bandel H.W. and Salerno J.A.: Phys. Rev., **146**, 40 (1966).
82) Salop A. and Nakano H.H.: ibid., A **2**, 127 (1970).
83) Trajmar S., Cartwright D.C. and Williams W.: ibid., A **4**, 1482 (1971).
84) Kennerly R.E., Bonham R.A. and McMillan M.: J. Chem. Phys., **70**, 2039 (1979).
85) Christophorou L.G. and Carter J.G.: Chem. Phys. Lett., **2**, 607 (1968).
86) Braglia G.L., de'Munari G.M. and Mambriani G.M.: Nuovo Cimento **41B**, 96 (1966).
87) Mozumder A.: J. Chem. Phys., **72**, 1657 & 6289 (1980).
88) Warman J.M. and Sauer M.C., Jr.: ibid., **62**, 1971 (1975).
89) Warman J.M. and de Haas M.P.: ibid., **63**, 2094 (1975).
90) Frommhold L.: Z. Phys., **156**, 144 (1958).
91) Schlumbohm H.: ibid., **182**, 317 (1965).
92) Heylen A.E.D.: J. Chem. Phys., **38**, 765 (1963).
93) Pollak W.J.: Trans. Faraday Soc., **64**, 2919 (1968).
94) Fink X. and Huber P.: Helv. Phys. Acta, **38**, 717 (1965).
95) Clow R.P. and Futrell J.H.: Int. J. Mass Spectrom. Ion Phys., **4**, 165 (1970).
96) Cottrel T.L. and Walker I.C.: Trans. Faraday Soc., **61**, 1585 (1965).
97) Cottrel T.L., Pollock W.J. and Walker I.C.: ibid., **64**, 2260 (1968).
98) LeBlanc O.H., Jun. and Devins J.C.: Nature, **188**, 219 (1960).
99) Cochran L.W. and Forester R.W.: Phys. Rev., **126**, 1785 (1962).
100) Cottrel T.L. and Walker I.C.: Trans. Faraday Soc., **63**, 549 (1967).
101) McGee J.D. and Jaeger J.C.: Phil. Mag., **6**, 1107 (1928).

102) Bansal K.M. and Fessenden R.W.: J. Chem. Phys., **53**, 3468 (1970).

103) Schumacher R., Sprunken H.R., Christodoulides A.A. and Schindler R.N.: J. Phys. Chem., **82**, 2248 (1978).

104) Christophorou L.G. and Christodoulides A.A.: J. Phys., B **2**, 71 (1969).

105) Yamane M.: J. Phys. Soc. Jpn, **15**, 1076 (1960).

106) Townsend J.S.: J. Franklin Inst., **200**, 563 (1925).

107) Lampe F.W.: "Ion-Molecule Reactions", ed. Franklin J.L., Plenum Press, New York, Vol. 2, Chap. 13 (1972).

108) Haydon S.C. and McIntosh A.I.: J. Phys., D **11**, 1859 (1978).

109) Matsushima H., Kitamori K., Tagashira H. and Sakai Y.: Papers of Technical Group of Electrical Discharges (IEE, Japan), ED-79-56 (1979) [in Japanese].

110) Moruzzi J.L. and Craggs J.D.: "Proc. 12th Intern. Conf. on Phenomina in Ionized Gases", ed. Hoelscher J.G. and Schram D.C., North Holland, Amsterdam, Neth., 1, 225 (1975).

111) Heylen A.E.D.: J. Phys. D **2**, 179 (1968).

112) Heylen A.E.D.: Int. J. Electr., **24**, 165 (1968).

113) Heylen A.E.D.: J. Phys., D **3**, 789 (1970).

114) Heylen A.E.D.: Int. J. Electr., **30**, 121 (1971).

115) Spencer L.V.: Phys. Rev., **98**, 1507 (1955).

116) Mott N.F.: Proc. Roy. Soc., A **124**, 425 (1929).

117) Roy R.R. and Reed R.D.: "Interactions of Photons and Leptons with Matter", Acad. Press, New York (1968).

118) Berger Ch., Knop G., Kofink H., Menze D. and Schulz W.: Z. Phys., **235**, 191 (1970).

119) Williams E.J.: Proc. Roy. Soc., London, A **169**, 531 (1939).

120) Rossi B.B.: "High Energy Particles", Prentice Hall, New York, 63 (1956).

121) Goudsmith G.A. and Saunderson J.L.: Phys. Rev., **57**, 24 (1940) & **58**, 36 (1940).

122) Molierè G.: Z. Naturforsch., **3a**, 78 (1948).

List of Symbols

Symbol	Definition	Unit
A	Defined by Eq. (2.21)	
B_θ	Magnetic flux induced by a pulsed beam	Gauss
c	Light velocity	cm/s
D_L	Lateral diffusion coefficient of electron against electric field	cm^2/s
D_{obs}	Observed maximum dose of a depth-dose curve in a dosi-meter placed on the beam axis	Mrad
E	Electric field	V/cm
E_b	Energy of beam electrons	eV
E_z	Electric field induced by a pulsed beam	V/cm
e	Electronic charge	CGS unit
$F(\varepsilon)$	Distribution function of secondary electron energies	
F_e	Electric force against electron	dyne
F_m	Magnetic force against electron	dyne
F_r	Total radial force against electron	dyne
f	Mean fractional energy loss per collision defined by Eq. (8.5)	
f_e	Space-charge neutralization factor defined by n_i/n_b	
f_m	Current or magnetic neutralization factor defined by I_{back}/I_b	
H_θ	Magnetic field induced by a pulsed beam	Gauss
I_b	Beam current	A
I_{back}	Backward plasma current induced by a pulsed beam	A
I_{net}	Net current defined by $I_b + I_{back}$ like Eq. (2.19)	A
I^p	Peak current of a pulsed beam	A
IP	Ionization potential	eV
k	Boltzmann's constant	erg/K
k_a	Electron-attachment rate constant	cm^3/s
k_d	Rate constant of dimer-ion formation like Eq. (6.18)	$molec.^{-2}\,cm^3\,s^{-1}$
k_T	Townsend energy factor	
m_e	Electronic rest mass	g
N_e	Number of beam electron per cm	cm^{-1}
n_b	Number density of beam electrons	cm^{-3}
n_d	Number density of dimer-ions	cm^{-3}
n_e	Number density of secondary electrons	cm^{-3}
n_i	Number density of ions	cm^{-3}
n_0	Number density of neutral molecules	cm^{-3}
p	Gas pressure at 20°C	Torr
$Q_m(\varepsilon)$	Momentum transfer cross section to a particle to an electron with energy ε	cm^2
Q_t	Total collision cross section of an electron to a particle	cm^2
R	Radius of an irradiation cell	cm
r	Radial distance from the beam axis	cm
r_0	Beam radius	cm
t	Time measured at the position of a dosimeter after the front of the beam passes this position	s

Symbol	Definition	Unit
t_B	Gas-breakdown time defined in 2.2.1	s
t_d	Defined in Fig. 2.1	s
t_f	Breakdown formative time defined by Felsenthal and Proud (Ref. 42) (cf. Eq. (6.14))	s
t_{flat}	Defined in Fig. 2.1	s
t_i	Mean ionization time	s
t_N	Space-charge neutralization time	s
t_r	Pulse rising time defined in Fig. 2.1	s
v	Electron randum velocity	cm/s
v_b	Beam-electron velocity	cm/s
w	Electron drift velocity	cm/s
w_m	Electron drift velocity in a binary mixture	cm/s
x	Mole fraction	
Z	Atomic number	
z	Co-ordinate direction along the beam axis	cm
z	$= E/p$ in Eq. (10.3)	$Vcm^{-1} Torr^{-1}$
α_m	α_T in a binary mixture	ion pair/cm
α_r	Electron-ion recombination coefficient	cm^3/s
α_{rd}	Electron-dimer ion recombination coefficient	cm^3/s
α_T	Townsend first ionization coefficient	ion pair/cm
β	Defined by v_b/c	
γ	Defined by $(1-\beta^2)^{-\frac{1}{2}}$	
ε	Secondary eiectron energy	eV
ε_b	Beam emittance in Eq. (2.20)	cm radian
ε_k	Characteristic energy	eV
η_T	Electron attachment coefficient	cm^{-1}
μ	Electron mobility	$cm^2 V/s$
ν	Defined by Eq. (2.8)	
ν_{en}	Momentum transfer collision frequency between an electron and a particle	s^{-1}
σ_e	Plasma conductivity	mho/cm
σ_{ei}	Plasma conductivity determined by electron-ion collisions	mho/cm
σ_{en}	Plasma conductivity determined by electron-neutral particle collisions	mho/cm
$\sigma_{ion}(E_b)$	Total ionization cross section by beam electron with energy E_b	cm^2
$\sigma_i(\varepsilon)$	Total ionization cross section by secondary electron with energy ε	cm^2

Note: Symbols used only in a single section are omitted.